Neural network dynamics in Parkinson's disease

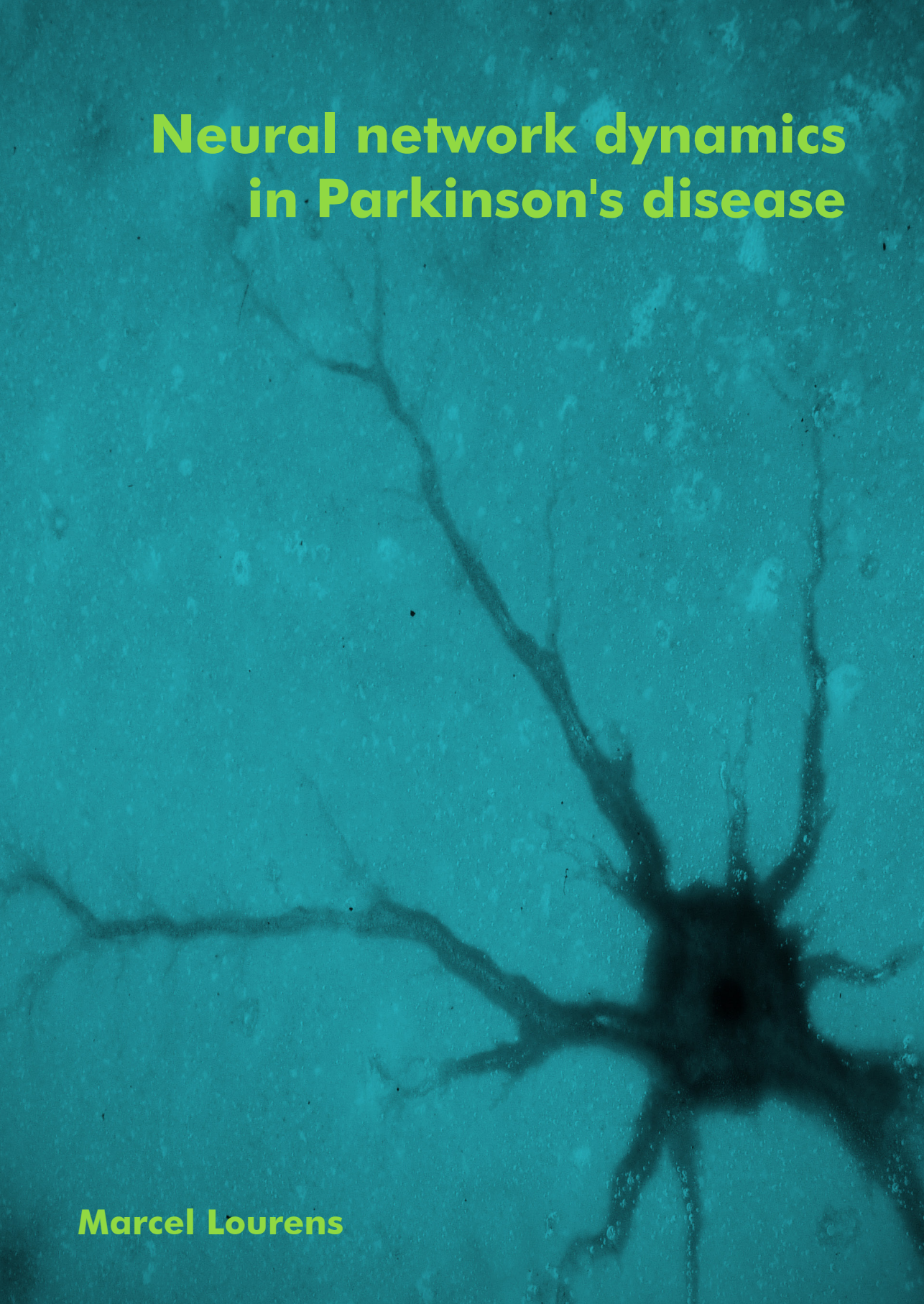

Marcel Lourens

Neural network dynamics in Parkinson's disease

Marcel Lourens

The research presented in this thesis was carried out at the group of Applied Analysis and Mathematical Physics (AAMP), the faculty of Electrical Engineering, Mathematics and Computer Science, and MIRA Institute for Biomedical Technology and Technical Medicine, University of Twente, PO Box 217, 7500 AE Enschede,The Netherlands.

UNIVERSITY OF TWENTE.

This work was supported by BrainGain Smart Mix Programme of the Netherlands Ministry of Economic Affairs and the Netherlands Ministry of Education, Culture and Science.

Lourens, Marcel A.J.

Neural network dynamics in Parkinson's disease.

Ph.D. Thesis, University of Twente, 2013.

This thesis is prepared with LaTeX 2_ε.

Printed by Gildeprint Drukkerijen, Enschede, The Netherlands.

ISBN : 978-90-365-3507-6 DOI : 10.3990/1.9789036535076

Neural network dynamics in Parkinson's disease

PROEFSCHRIFT

ter verkrijging van
de graad van doctor aan de Universiteit Twente,
op gezag van de rector magnificus,
prof. dr. H. Brinksma,
volgens besluit van het College voor Promoties
in het openbaar te verdedigen
op woensdag 3 april 2013 om 14:45 uur

door

Marcel Antonius Johannes Lourens
geboren op 30 november 1980
te Deventer

Dit proefschrift is goedgekeurd door promotor,
prof. dr. S.A. van Gils

en de assistent-promotor,
dr. ir. L.J. Bour

Samenstelling van de promotiecommissie:

Voorzitter en secretaris:	
prof. dr. ir. A.J. Mouthaan	Universiteit Twente
Promotor:	
prof. dr. S.A. van Gils	Universiteit Twente
Assistent-promotor:	
dr. ir. L.J. Bour	Academisch Medisch Centrum Amsterdam
Leden:	
prof. dr. C.F. Beckmann	Universiteit Twente
dr. H.C.F. Martens	Sapiens Steering Brain Stimulation
prof. dr. C.C. McIntyre	Case Western Reserve University School of Medicine
prof. dr. ir. M.J.A.M. van Putten	Universiteit Twente
prof. dr. Y. Temel	Universiteit Maastricht
prof. dr. ir. P.H. Veltink	Universiteit Twente

To all laboratory animals

Contents

CHAPTER 1

Introduction

"build it, and you understand it." John Hopfield

1.1 Parkinson's disease

In 1817 a British surgeon named James Parkinson described in 'An Essay on the Shaking Palsy' a disease called 'paralysis agitans' in which a patient experiences muscle weakness and involuntary movements (tremor). He was the first to formally describe this disease that would later be renamed as Parkinson's disease (PD). However, the description of 'paralysis agitans' by Parkinson did not bring forward the recognition of its pathological origin. This became clear in the 1950's. PD results from degeneration of neurons in a region of the brain known as the basal ganglia. This part of the brain is involved in movement control. In particular, neurons in the substantia nigra pars compacta (SN_c) are degenerated. These neurons project to the striatum and hence their degeneration leads to a shortage of the signaling molecule (neurotransmitter) dopamine in the main input structure of the basal ganglia, causing movement impairments that are characteristic for the disease.

The number of people living with PD worldwide in 2005 is estimated to lie between 4.1 and 4.6 millon and it is estimated that this number will reach 8.7 to 9.3 million by 2030 due to the increasing number of elderly people [52]. Although the risk to get PD is much higher for older individuals (average age at onset is 68 years), patients with young onset are also reported [216, 225]. PD is nowadays subdivided in idiopathic Parkinson's disease (having unknown cause) and Parkinson plus syndromes [215]. Parkinson plus syndromes counts for 15% of all parkinsonism, although in large autopsy series the percentage was estimated as 20–25% [87], thus leaving idiopathic Parkinson's disease as the most frequently occurring form [95]. In this thesis we concentrate on idiopathic PD and PD will refer to this form of the disease only.

Although the specific causes of PD remain unknown, it seems that it involves a combination of genetic and environmental factors. The pathology of the disease is characterized by progressive loss of neuromelanin-containing cells and by the presence of intra-cytoplasmic inclusions, called Lewy bodies, in surviving neurons in the SN_c and other areas. For an overview see Usunoff et al. [215]. The Lewy bodies consist primarily of an accumulation of a neuronal protein called α-synuclein. "Lewy bodies in the substantia nigra (SN) are considered the pathological hallmark of Parkinson's disease, which means that if they cannot be found, the diagnosis is not Parkinson's disease" [215]. There are no Lewy bodies involved in Parkinson-plus syndromes. However, within the human SN_c not all subareas degenerate. In particular, most severe neuronal loss is in the ventrolateral SN_c [215]. The affected area of the SN_c gives rise to most of the dopaminergic innervation of the sensorimotor region of the putamen, which is part of the striatum. Thus, dopamine loss mainly affects the nigrostriatal pathway. The conclusion that PD involves degeneration of pigmented neurons of the brain stem is inevitable [68]. This conclusion is also based on the distribution of Lewy bodies in other brainstem areas.

As a consequence of dopamine depletion, neurons in the basal ganglia have altered firing rates and have disturbed activity patterns with increased synchronization, see reviews by Hammond et al. [80] and Galvan and Wichmann [61]. Such changes lead to different symptoms whose manifestation and severity are highly variable from patient to patient. Due to several compensatory mechanisms, such as super-sensitivity of dopamine receptors and neuronal plasticity of the brain, the first clinical signs of PD manifest only when approximately 70–80% of striatal dopamine levels are depleted or 50–60% of the dopaminergic neurons are lost in the SN_c [23, 26]. The four cardinal motor symptoms of PD include muscle rigidity, tremor of the limbs at rest, slowness and impaired scaling of voluntary movement (bradykinesia)/loss of voluntary movements (akinesia) and postural instability [93]. Other motor symptoms include gait and posture disturbances as well as speech and swallowing disturbances. In addition to these motor symptoms many patients also suffer from non-motor symptoms, including personal and behavioral, cognitive, sensory, and autonomic disturbances. It should be mentioned that the early symptoms (tremor, rigidity and bradykinesia) are related to progressive loss of dopamine, while the later symptoms are not always related to the dopamine depletion.

Currently, there is no treatment available to prevent the onset or to stop/slow down the progression of PD. However, there exist excellent drugs and surgical treatments to effectively control the symptoms of the disease. When the cardinal symptoms start to show up and are severe enough to interfere with daily life, patients get different types of medication in order to increase their dopamine level in the basal ganglia, thereby suppressing the motor symptoms. Nowadays, the most com-

mon and effective therapeutic treatment for PD is a dopamine replacement therapy, which consists in adminstration of the dopamine precursor levodopa (L-Dopa). In particular, replacement of dopamine with L-Dopa improves bradykinesia, rigidity and, to a lesser extent, tremor. However, long-term (5–10 years) L-Dopa usage is commonly associated with motor fluctuations ('on–off' effect) and abnormal involuntary movements (dyskinesia) [156, 157]. Dopamine deficiency can also be treated with medications that prevent the breakdown (Monoamine oxidase (MAO) B inhibitors or Catechol-O-methyl transferase (COMT) inhibitors) or mimick the effects (dopamine agonists) of dopamine. Those therapies are less effective than treatment with L-Dopa and they are not without their own adverse effects. Moreover, some of them work only in combination with L-Dopa. As the disease progresses, the efficacy of all drug therapies decreases, and higher doses have to be administered.

Surgical techniques such as lesioning or deep brain stimulation (DBS) of specific brain regions are other therapies to reduce PD motor symptoms, when medication does no longer produces satisfying results or in case side-effects of medication become significant. Due to the operation risks of ablation of functional targets, such as hemorrhages and loss of brain function, lesioning surgery has gradually been replaced by DBS surgery. DBS is able to mimic the effects of ablation in a reversible manner and is now an established treatment of advanced PD [16, 76]. The procedure for DBS involves the implantation of an electrode called the lead into a region of the brain that controls movement. The lead is then connected via an insulated wire (extension) to a programmable, battery-operated pulse generator ('brain pacemaker') that is implanted below the clavicle, see Figure 1.1A. The DBS lead can be implanted in one of several nuclei including the subthalamic nucleus (STN) [15, 122], globus pallidus pars interna (GPi) [190] and the ventral intermediate thalamic (VIM) nucleus [12, 13]. Thalamic DBS is mainly effective in reducing tremor. However, when DBS is predominantly applied within the STN or GPi, it relieves other PD motor symptoms, including rigidity and bradykinesia [76]. Remarkably, DBS is only effective for the different target nuclei within very specific parameter ranges, most notably at high frequencies ($>$100 Hz) and with lower amplitudes at higher frequencies [146, 177]. These parameter settings for DBS are based on several studies [14, 122, 219, 220]. Despite the high clinical success rate, the mechanism by which DBS prevents pathophysiological responses of the motor network remains to a large extend unknown. It is suggested that high frequency stimulation leads to somatic inhibition of neurons that are close to the electrical field, while simultaneously afferent and efferent axons may be excited. Both cellular and network effects may contribute to the overall clinical effects of DBS. Moreover, stimulation does not necessarily have to restore the network to a pre-pathological, i.e. normal state, but should allow improvement in Parkinson's symptoms. McIntyre and Hahn [136] hypothesize

that high frequency stimulation disrupts or desynchronizes the pathological activity by changing the underlying dynamics of the stimulated brain networks, which can be achieved via activation, inhibition, or lesion.

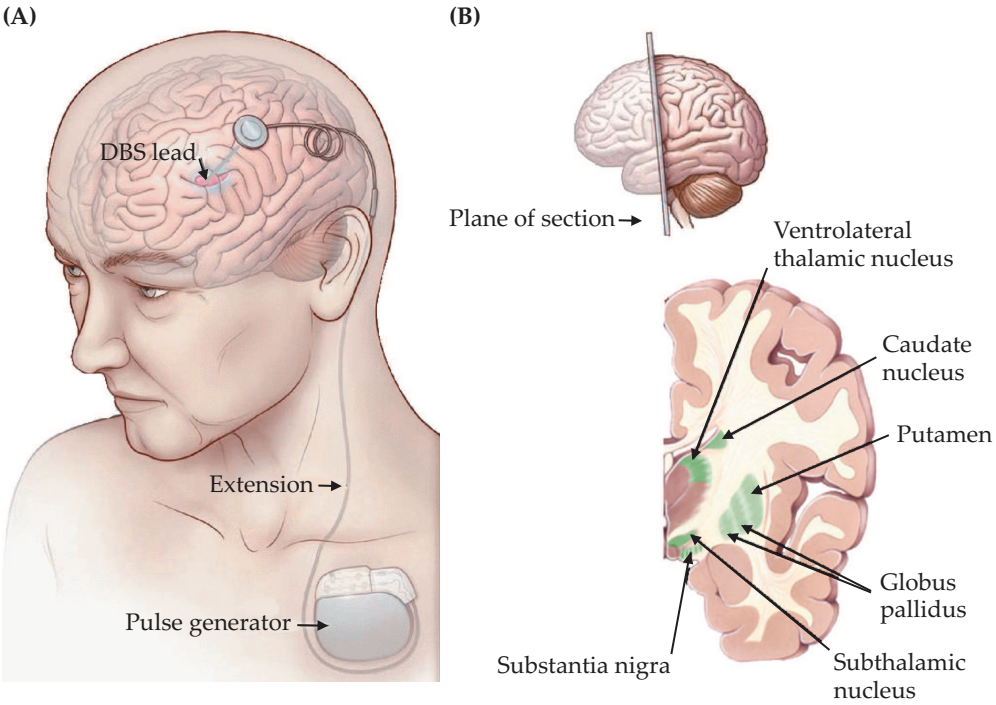

Figure 1.1 (**A**) Schematic representation of the implantation of a deep brain stimulation system. (**B**) The basal ganglia area. The four principal nuclei are the striatum (putamen and caudate nucleus), the substantia nigra, the subthalamic nucleus and the globus pallidus. Reproduced with permission from Okun [159], Copyright Massachusetts Medical Society.

1.2 Basal ganglia

One of the main brain regions that is involved and affected in PD is the basal ganglia. It is the collective name given to a group of interconnected forebrain nuclei located at the base of both cerebral hemispheres, lateral to and surrounding the thalamus. It includes the neostriatum, the globus pallidus pars externa (GPe) and pars interna, the substantia nigra pars compacta and pars reticulata (SN_r), and the subthalamic nucleus. The neostriatum is further subdivided in the caudate nucleus and the putamen. Except for their most anterior part, the caudate nucleus and putamen

are completely separated by the internal capsula, a large collection of fibers run between the neocortex and the thalamus in both direction [103]. Figure 1.1B shows the relative locations of these nuclei.

Although the basal ganglia nuclei do not have a direct input or output to the spinal cord, they play a major role in normal voluntary movement. It is now widely acknowledged that the basal ganglia are not only involved in motor function but also in cognition and emotion. This is reflected in the fact that the basal ganglia receive input from almost the whole cortex. Moreover, dysfunctioning of the basal ganglia is not only associated with movement disorder, but also with psychiatric disorders such as obsessive-compulsive disorder [9].

The striatum acts as the major receiver of inputs to the basal ganglia mainly from the cortex as well as from the thalamus and to a lesser extent from the brainstem. The corticostriatal connections have an excitatory effect on the GABAergic striatal neurons and come almost from all parts of the cerebral cortex. The GABAergic striatal neurons project directly or indirectly, via the GPe and the STN, to the output nuclei, which in turn project to the thalamus and the brain stem. Thus, basal ganglia nuclei process the cortical information and send their output to the brainstem, and via the thalamus, back to the cortex. These information processing occur in anatomically and functionally segregated parallel circuits. Depending on the cortical region involved, these circuits are divided in motor, oculo-motor, associative (dorsolateral prefrontal and orbitofrontal) and limbic loops [3, 4, 139, 194]. Each circuit uses different parts of the basal ganglia and the thalamus. As PD is mainly a movement disorder, we will focuss on the motor circuit. The major pathways within the basal ganglia-thalamocortical loop, which are known to be involved in the execution of voluntary movement, are illustrated in Figure 1.2 [61, 64, 103].

Much of the insights into the motor function of the basal ganglia have been obtained by studying the deficits that occur following disorders of the basal ganglia, such as Parkinson's disease and Huntington's disease. This research was facilitated by the discovery that neurotoxin 1-methyl-4-phenyl-1,2,3,6-tetrahydropyridine (MPTP) can selectively destroy nerve cells in the substantia nigra of primates after systemic administration, thereby inducing parkinsonian symptoms.

1.2.1 The classical model of the basal ganglia

In the late 1980's, a model for basal ganglia motor circuit functioning was proposed by Albin et al. [2] and DeLong [47]. Derived from studying human movement disorders, the model consists of two major connections, the so called direct and indirect pathways, linking the basal ganglia input nucleus (striatum) to the output nu-

clei (GPi/SN_r). The critical balance between these two pathways determines normal motor behavior. The basal ganglia output nuclei have a high rate of spontaneous discharge, and thus exert a tonic, GABA-mediated, inhibitory effect on their target nuclei in the thalamus. The inhibitory outflow is differentially modulated by the direct and indirect pathways, which have opposing effects on the basal ganglia output nuclei, and thus on the thalamic targets of these nuclei.

The direct pathway arises from inhibitory striatal efferents that contain both GABA and substance P and it projects directly to the output nuclei. It is transiently activated by increased phasic excitatory input from the SN_c to the striatum. Activation of the direct pathway briefly suppresses the tonically active inhibitory neurons of the output nuclei, disinhibiting the thalamus, and thus increasing thalamocortical activity. The indirect pathway starts with inhibitory striatal efferents that contain both GABA and enkephalin. These striatal neurons project to the GPe, which in turn, projects to the STN, via a purely GABAergic pathway, which finally projects to the output nuclei via an excitatory, glutamatergic projection. There is also a direct projection from the GPe to the output nuclei. The indirect pathway is phasically activated by decreased inhibitory input from the SN_c to the striatum, causing an increase in striatal output along its pathway. Normally the high spontaneous discharge rate of GPe neurons exerts a tonic inhibitory influence on the STN. Activation of the indirect pathway tends to suppress the activity of GPe neurons, disinhibiting the STN, and increasing the excitatory drive on the output nuclei. The decreased GPe activity also directly disinhibits the output nuclei. The resulting increase in activity of the output nuclei inhibits the thalamus further, decreasing thalamocortical activity. Activation of the direct pathway thus *facilitates* movement, whereas activation of the indirect pathway *inhibits* movement. See McIntyre and Hahn [136], for an extended overview.

Nigrostriatal dopamine projections exert contrasting effects on the direct and indirect pathways (Figure 1.2). Dopamine is released from the SN_c into the synaptic cleft, where it binds to the receptors of the striatum. The effect of dopamine is determined by the type of receptor to which it binds. Striatal neurons projecting in the direct pathway have D1 dopamine type receptors, which cause excitatory post synaptic potentials, thereby producing a net excitatory effect on striatal neurons of the direct pathway. Those projecting in the indirect pathway have D2 type receptors, which cause inhibitory post synaptic potentials, thereby producing a net inhibitory effect on striatal neurons of the indirect pathway. The facilitation of transmission along the direct pathway and suppression of transmission along the indirect pathway, both have the same effect of reducing inhibition of the thalamocortical neurons and thus facilitating movements initiated in the cortex. Thus, the overall influence of dopamine

within the striatum may be to reinforce the activation of the particular basal ganglia-thalamocortical circuit which has been initiated by the cortex [63, 64, 90].

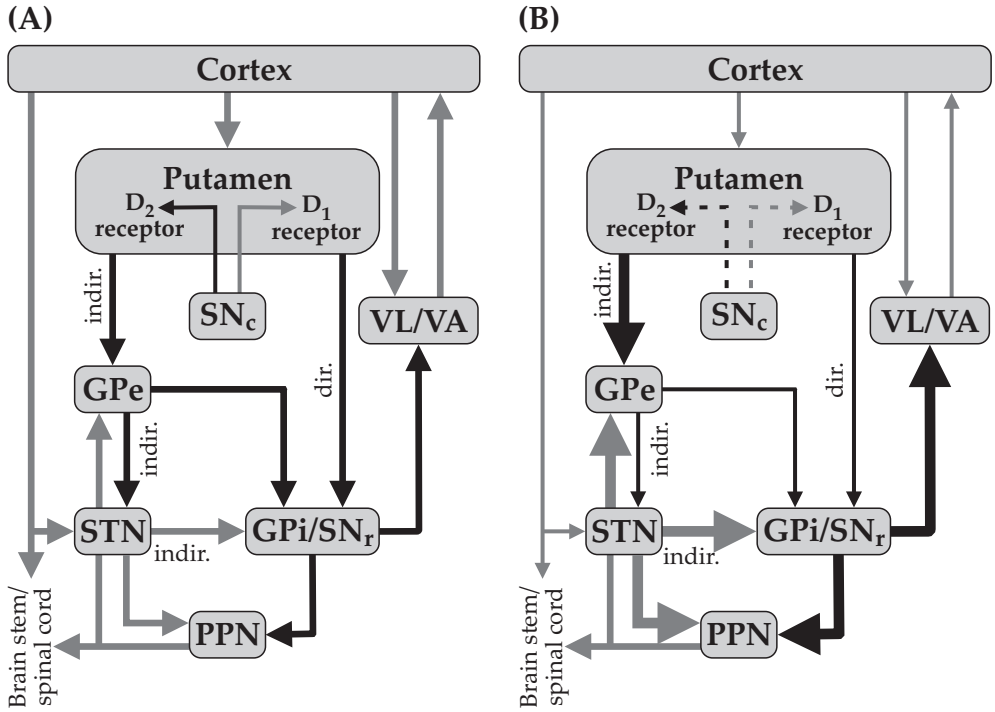

Figure 1.2 Connection diagram of the basal ganglia-thalamocortical motor circuit. Black lines indicate inhibitory pathways; grey lines indicate excitatory pathways. Thickness of the lines corresponds to the presumed connection strength between different regions during healthy (**A**) and parkinsonian (**B**) brain states. *Abbreviations*: Dir., direct pathway; GPe, globus pallidus pars externa; GPi, globus pallidus pars interna; Indir., indirect pathway; PPN, pedunculopontine nucleus; SN_c, substantia nigra pars compacta; SN_r, substantia nigra pars reticulata; STN, subthalamic nucleus; VA, ventroanterior thalamic nucleus ; VL, ventrolateral thalamic nucleus.

1.2.2 The classical model in PD

Using the above model of basal ganglia function with its direct and indirect pathway, PD is explained as an imbalance between the two pathways. Due to the differential effects of dopamine on the D1 and D2 dopamine receptors of the striatum, a loss of striatal dopamine results in a reduction in transmission through the direct pathway and an increase in transmission through the indirect pathway. In the direct pathway, a reduction in inhibitory influence on the output nuclei occurs. Within the indirect

pathway, an excessive inhibition of the GPe leads to disinhibition of the STN, which in turn provides excessive excitatory drive to the output nuclei. The resulting increase in activity of GPi and SN_r neurons leads to excessive inhibition of thalamocortical and brain stem neurons, which in turn supports the hypokinetic symptoms of bradykinesia and akinesia as seen in PD. Increased firing rates are found in the striatum, GPi and STN and a minimally decreased discharge in the GPe. A summary of tonic firing rates of basal ganglia nuclei in the normal and parkinsonian situation can be found in Heida et al. [83].

1.2.3 Limitations of the classical model

There are several clinical and experimental findings that cannot be explained by the classical model of the basal ganglia, see Obeso et al. [157]. The assumption of the classical model is the existence of two parallel cortico-basal ganglia-thalamocortical loops that diverge within the striatum and are differentially modulated by dopamine. However, anatomical and chemical separation of striatal neurons giving rise to the two pathways is unlikely to be absolute, considering the fact that striatal neurons can co-express D1 and D2 receptors [1, 201] and striatal neurons have been found projecting to GPe, GPi and SN_r [119]. In the classical model, the effect of dopamine is restricted to the striatum while there is evidence that dopamine can have effect in other regions of the basal ganglia-thalamocortical loop [99, 193].

The classical model leaves out a number of connections that maybe important for motor function. For example, the cortico-STN hyperdirect pathway [11, 32, 149, 151, 152] conveys powerful excitatory effects from the motor-related cortical areas to the globus pallidus, bypassing the striatum. The hyperdirect pathway is therefore an alternative direct cortical link to the basal ganglia, possibly as important to motor control as the direct pathway, which is typically considered to be the main cortical relay in the basal ganglia. But also connections from the basal ganglia to brain stem structures, such as the pedunculopontine nucleus (PPN), are not involved. PPN plays a role in the control of muscle tone by means of its excitatory projections to the muscle tone inhibitory system in the brainstem and to inhibitory interneurons in the spinal cord. The PPN is also thought to produce the main influence on the parafascicular thalamic nucleus in case of SN degeneration [229]. The parafascicular nucleus is involved in motor control. In PD the increased inhibitory basal ganglia output, together with a decrease in cortical excitation of the PPN, may increase the level of muscle tone causing rigidity [205].

The classical model is based on the idea that the average firing rate in the output of the basal ganglia controls and predicts motor behavior. However, the pattern

of discharge of basal ganglia neurons is thought to be equally as important as the rate of discharge in the execution of smooth movements [19, 21, 28, 80]. Several alterations in the discharge pattern have been observed in neurons of the basal ganglia in PD subjects. These alterations include a tendency of neurons to discharge in bursts, increased correlation and synchronization of discharge between neighboring neurons, rhythmic and oscillatory behavior, see reviews by Hammond et al. [80], and Galvan and Wichmann [61]. Coherence between STN and GPi activity has been confirmed at tremor frequencies (3–10 Hz) [34]. These oscillatory patterns are projected to GPi's thalamic projection site, the ventroanterior thalamic nucleus, and the cortex. In addition, STN and GPi demonstrate a tendency to synchronization at beta-frequencies (11–30 Hz), which is likely to be driven from the motor areas of the cortex [32]. Several studies have demonstrated both in local field potentials and neuronal spike activity, that beta-frequency oscillations and synchronization are prominent features of the STN activity in PD patients and inversely correlate with the motor improvement produced by either dopaminergic treatment or DBS of the STN [32, 111, 113, 121, 173, 175]. In this circuit, the thalamus is in a key position as it receives the convergent afferent input from the GPi, the cortex, and the peripheral system, which it then projects back to the cortex, including motor areas [194].

1.3 Computational models of the basal ganglia

Computational studies are useful in investigating how pathological conditions and DBS induced activity may find their way through the basal ganglia-thalamocortical circuit and the basal ganglia-brain stem circuit. In addition, computational models can be used in order to test new DBS targets and DBS protocols and to confirm or reject hypotheses concerning the mechanisms underlying the pathological activity in the basal ganglia.

In 1952, Alan Lloyd Hodgkin en Andrew Huxley wrote a series of papers, describing the electrophysiological experiments they conducted on a giant squid axon to reveal the mechanisms which govern the generation of action potential in neurons. They discovered that the changes in membrane potential during an action potential result from the regulated opening and closing of sodium and potassium channels in the cell membrane. From their experiments they derived a mathematical model consisting of a set of nonlinear partial differential equations to describe the genesis of the action potential [85]. One can say that the field of computational neuroscience started with Hodgkin's and Huxley's mathematical description of their experimental results. Their equations describing the flow of ions across the cell membrane based

on voltage and on concentration are still used in computational models of neurons today.

Thus, neurons can be modeled using the properties of ion channels in the cell membrane. To build a good biophysical model of a certain neuron involves at least the following steps. Firstly, the ionic currents, which are responsible for the characteristic spiking behavior of that neuron type, have to be identified. For this purpose, pharmacological channel blockers can be used. Secondly, to measure the kinetic parameters of the currents, various stimulation protocols need to be performed, such as voltage-, space- and patch-clamp. Finally, a mathematical model of the Hodgkin–Huxley type equations is used to describe the dynamics of the membrane potential and the ion channels.

The majority of realistic single cell models used today are based on the Hodgkin–Huxley formalism and they are referred to as conductance-based models. A neuron can be represented as a point, meaning that there is no cellular morphology dependency. Cellular morphology can be incorporated by dividing the neuron into compartments where each compartment is simulated by a conductance-based model, and the compartments are coupled via conductances. Having now a mathematical description of a single neuron at our disposal, we can connect the individual neuron models together via synapses or gap-junctions to form neuronal circuits.

Terman et al. [211] were one of the first to develop a biophysically plausible model of a subset of the basal ganglia. In particular, their model includes a population STN cells and GPe cells, in which each STN and GPe cell is represented as a single compartment conductance-based model. They use voltage-clamp and current-clamp data from rat neurons to estimate the kinetic parameters of both cell models. Their subthalamopallidal network model has well defined physiological and pathological states, that rely on the strength of the synaptic connections between the cells and the inputs to them. They demonstrate that under parkinsonian condition, i.e. increased inhibitory input to the GPe, the STN–GPe network can show a pacemaker rhythm at tremor frequency. Their results support the hypothesis that the pathological activity in the basal ganglia as seen in PD is caused by the interaction between the STN and GPe rather than being driven by an external source [170].

The output of the basal ganglia network is directed towards the thalamic nuclei (Figure 1.2), which influences the motor cortex. Rubin and Terman [181] extend their STN–GPe network model with a population of GPi and thalamic relay cells to investigate how DBS can affect the functioning of the thalamus as a relay station. Although this is a simplification, it is presumed that this relay should retransmit incoming information from cortex and sensory systems back to cortex. They show how DBS may be regularizing the output of thalamus. The pathological oscillations from the basal ganglia may impair the transmission of thalamocortical information. When replac-

ing these basal ganglia oscillations by regular DBS input, thalamocortical relay may be restored [70, 181]. A lot of computational studies of the basal ganglia in relation to PD and DBS are based on these two network models, including the studies described in Chapters 2 and 3.

1.3.1 Tuning and fitting of the parameters

We started the Introduction with the quote "Build it, and you understand it". Thanks to, among other things, the work of Hodgkin and Huxley we are able to model a neuron from which we can go to neuronal circuits, brain structures and even the whole brain. But what do we learn from it? Conclusions drawn from models are only valuable when the network model is able to describe and to predict experimental studies correctly. A crucial step in constructing a realistic neuron model is the tuning of model parameters to replicate well described properties of the neuron in question. Experimental studies on the properties and localization of current channels are therefore a prerequisite for adequate modeling of a neuron. However, information regarding the presence, types and properties of ion channels in human neurons is scarce. Although these gaps in knowledge can be filled in by using the parameters obtained from experimental animal studies, difficulties in fitting and tuning remain because of different experimental conditions, which makes it difficult to compare results. Moreover, different parameters and different current can lead to the same firing behavior. As put forward by Izhikevich [91], the behavior of a neuron model should be equivalent to the neuron under consideration. He proposes that the behavior of the model is equivalent to the neuron if it undergoes the same dynamical bifurcation as the neuron, even if some of the currents are omitted or some of the kinetic parameters are guessed incorrectly [91]. For single neuron model bifurcation analysis is possible, but for large network models it is almost, if not, impossible.

In the network model of Terman et al. [211] the architecture and the coupling strength between STN and GPe cells as well as the applied current to them are essential for the obtained physiological and pathological states. In contrast, the network model of Hahn and McIntyre [72] is able to switch from parkinsonian to healthy activity by reducing the influence of the cortical beta input, thereby supporting the hypothesis that parkinsonian activity within the STN–GPe network has a cortical origin. Interesting in the work of Hahn and McIntyre [72] is the way they deal with the gaps in knowledge of the topography and the strength of the synaptic connections within and between the cellular populations (STN, GPe and GPi), and the input to these populations. They use a relatively simplistic and stereotyped functional channel architecture, in which the action-selection function of the basal ganglia is

preserved. To define the coupling and input parameters such that the model activity resembles experimental observed activity, they develop an optimization algorithm, whereas Terman et al. [211] use a parameter sensitivity analysis to identify unique parameter sets. The algorithm tries to match the firing and burst rate characteristics of the STN, GPe, and GPi obtained from micro-electrode recordings of MPTP treated monkeys by adjusting a set of coupling and input parameters.

In general there is a wide gap between experimental animal results, especially with respect to neuroanatomical data, and computational modeling. In order to be able to investigate the anatomical and functional properties of afferent and efferent connections between the different nuclei of the basal ganglia, neuroanatomical tracing and degeneration studies need to be performed. These studies, though very time-consuming, are essential to decide which pathways play important roles in normal functioning and therefore need to be included in modeling studies. In addition, it should be known what neuroanatomical changes take place resulting from the neurodegeneration associated with Parkinson's disease and how they affect network behavior. For instance, the direct effects of DBS on motor control are of interest, but since DBS has a low threshold to side effects, additional non-motor pathways are expected to be involved. Including these pathways in network models may shed light on the extent and effect of stimulation. Similarly, as PPN stimulation may have a beneficial influence on gait and balance, different pathways are important regarding the different motor symptoms of PD.

Population level recordings such as local field potential (LFP) are commonly used in animal research in Parkinson's disease, see Chapter 5. It is not trivial how such recordings can be used in network models of spiking neurons. Generally speaking, it is assumed that LFP reflects the incoming synaptic activity (excitatory and inhibitory postsynaptic potentials) [102, 141], while spikes reflect the output of the local network [59, 117]. However, other slow processes may contribute to the generation of LFPs, see Moran and Bar-Gad [143] and references therein. To use the observations of population level recordings to tune the spiking models, for example in the fitting algorithm of Hahn and McIntyre [72], the spiking activity has to be averaged in one way or another.

It is also possible to represent the neural populations within the basal ganglia-thalamocortical loop with neural mass models, which describe the collective dynamics of an ensemble of neurons and the interaction with other ensembles. Dynamic Causal Modeling is a theoretical framework which can be used to reveal the synaptic strength within the basal ganglia-thalamocortical loop from the population level recordings through optimization of neural mass model parameters given a set of recordings and a network topology [108, 145, 198, 199]. However, the results are not straightforward to relate to spiking models.

Dissociated neural cultures as well as brain slices positioned on multi electrode arrays open the possibility to study basal ganglia nuclear functional action and interaction, i.e. the overall result of all cell membrane activities of a neuron or group of neurons. By the addition of neurotransmitters, their agonists or antagonists, PD basal ganglia activity can be mimicked *in vitro*. It is expected that this alternative route of studying PD will bring up the badly needed extra information to support fine-tuning of neuron and neuronal network models and will as a consequence incorporate the more subtle connections nowadays described in neuroanatomical studies.

Essential in modeling is to formulate reduced models that still capture essential properties of the dynamics but are able to include even these subtle connections. Models need verification by experiments to demonstrate that the model has reality value. With the increasing amount of *in vitro* and *in vivo* experimental data computational models may become applicable in human research and health care problems. The therapeutic stimulation parameters for DBS (polarity, pulse amplitude, pulse width, frequency) will in the near future rely more on the predictions made by model simulations [46]. Below we give an example how micro-electrode recordings can be used as input for a thalamic relay cell model to validate the existence of a clinically effective stimulation window that combines low stimulation amplitudes and high frequencies [137].

1.3.2 Example of using micro-electrode recordings within computational models

We used a thalamic relay cell model to investigate the effect of DBS parameters on thalamocortical relay of excitatory cortical inputs and pathological basal ganglia oscillations. In particular, we focused on the effectiveness of the stimulation with respect to PD tremor reduction. A GPi spike train obtained from a human PD patient during DBS surgery with characteristic patterns of rest tremor was used to generate GPi input to the thalamus. See Chapter 4 for the details how such a spike train can be extracted from micro-electrode recordings. Without relay of cortical input (rest situation), the thalamic model response consisted of rebounds at the same tremor frequency (Figure 1.3).

By including excitatory input the combined effects of relay, PD and DBS could be examined (Figure 1.4). The pathological input was partially replaced by DBS pulses reflecting a limited volume of tissue being activated by the stimulation. For DBS there are two common targets: STN and GPi. Stimulation of the STN may recruit efferent fibers that excite GPi. In both cases it is therefore plausible that DBS leads to additional downstream GPi output. At the thalamus, the input from the basal

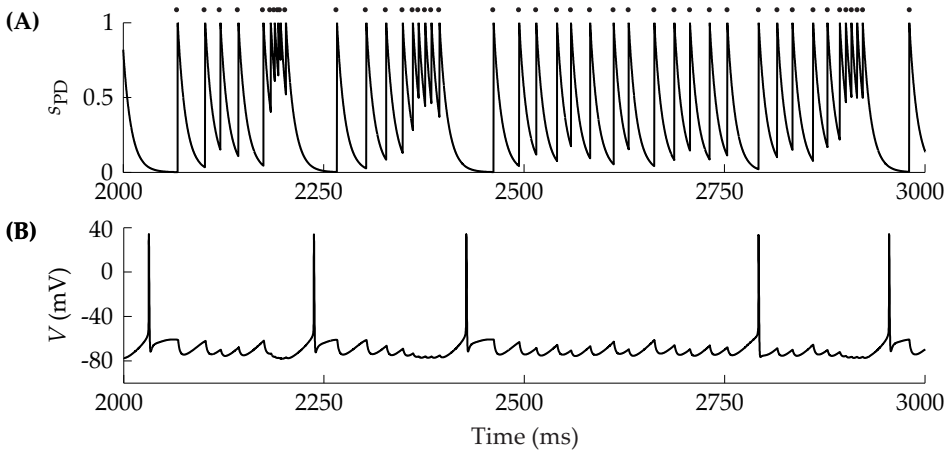

Figure 1.3 (**A**) The model synaptic input (s_{PD}) reflects the burstiness of the activity of the measured GPi neuron. The presynaptic GPi spike times are indicated by the dots. (**B**) The thalamic relay cell exhibits post-inhibitory rebound action potentials, i.e. during the pause after the GPi burst an action potential is generated.

ganglia comes from the GPi and is therefore inhibitory. A key property of thalamic relay cells is their low-threshold T-type calcium current. When the thalamic relay cell is inhibited long enough, it fires rebound action potentials when it is relieved from inhibition [92] (Figure 1.3B). The effect of such phasic pathological inhibition is that the thalamic output activity does not reflect the original excitatory input. This stems from two sources of errors. Long periods of inhibition diminish the responsiveness of the thalamic relay cell and rebound spikes are mixed with successful relays.

In the model we found that additional high frequency stimulation induced inhibition can stop the transmission of pathological oscillations around the loop. The relay of excitatory cortical input is, however, not affected for mid-range to moderately high DBS amplitudes (Figure 1.4B). Failure of the relay function is only observed at very high DBS amplitudes (Figure 1.4C). Taken together, this approach yields a parameter window that corresponds to therapeutic stimulation, i.e where relay of sensorimotor information is maintained and pathological input is suppressed.

1.4 Outline of the thesis

In the following two chapters, we employ computational models in order to get insight in a new proposed stimulation protocol as well as a new proposed target for deep brain stimulation. It has been suggested that short-duration stimulation protocols instead of the standard continuous high frequency stimulation may also disrupt

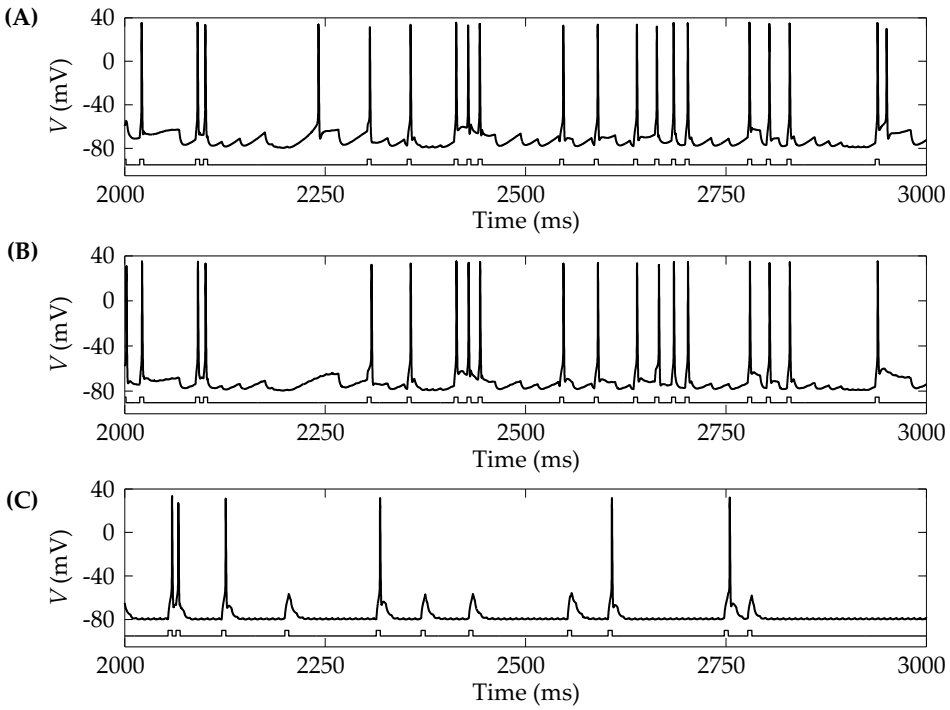

Figure 1.4 The effect of overwriting the pathological GPi input by increasing DBS amplitude. The upper traces represent the membrane voltage (V) of the thalamic relay cell. The precise timing of the excitatory input (mean rate 16.5 Hz) is displayed beneath each voltage trace. (**A**) If the stimulation amplitude is too weak, rebounds and an incorrect signal relay occur. (**B**) With moderate DBS amplitude, rebounds are quenched and relay is correct. (**C**) With high DBS amplitude, relay of sensory information is impaired.

the pathological activity [208]. The mechanism underlying these protocols is supposedly synaptic plasticity. We extend the STN–GPe network model of Rubin and Terman [181] with spike-timing-dependent plasticity (STDP) to explore its role in stabilizing firing patterns in the basal ganglia. Moreover, we investigate how stimulation should be applied, such that it exploits STDP most effectively to teach the network to fire in a less pathological manner.

Due to its location in the brainstem and its function in locomotion and postural control, the pedunculopontine nucleus (PPN) has been suggested as a target for DBS to improve gait and postural instability. It is remarkable that DBS in PPN should be applied with low frequency (20–25 Hz) to improve gait disturbances and postural instability. Based on experimental data, we have developed a computational conductance-based model for the glutamatergic PPN type I cell. The network model of Rubin and Terman [181] produces basal ganglia output that is used as input for the PPN cell. The conductances for projections from the STN and the GPi to the PPN

are determined from experimental data. The resulting behavior of the PPN cell is studied under normal and parkinsonian conditions of the basal ganglia network. The effect of high frequency stimulation of the STN is considered as well as the effect of combined high frequency stimulation of the STN and stimulation of the PPN at various frequencies.

In Chapter 4 we optimize spike-sorting algorithms which are able to automatically extract individual unit-activity from multi-unit micro-electrode recordings obtained during deep brain stimulation surgery. We use the spike-sorting algorithms to investigate the functional connectivity between STN neurons in PD patients. Furthermore, we investigate the spatial distribution of the functional connectivity within the STN. To do so, we map the multichannel STN micro-electrode recordings, that are classified in the STN, to a generic atlas representation of the STN with a sensorimotor part and a remaining part.

Finally, in Chapter 5, we develop a measurement set-up to record local field potentials in different brain structures relevant for Parkinson's disease in freely moving rats. We were able to record in the same animal, under healthy and parkinsonian conditions, at rest or during forced exercise. The obtained data may be used to tune the computational models in the first two chapters or other computational models of the basal ganglia, see Section 1.3.1.

CHAPTER 2

The effect of spike-timing-dependent plasticity on activity patterns in the basal ganglia

Abstract In advanced Parkinson's disease (PD), deep brain stimulation (DBS) can be used to disrupt the pathological activity in the basal ganglia, thereby reducing the PD motor symptoms. The standard protocol for DBS, continuous high frequency stimulation of target cells, is applied notably in subthalamic nucleus (STN) or globus pallidus pars interna. It is proposed that short-duration desynchronizing stimulation protocols may also disrupt pathological activity: synaptic plasticity is supposed to be the underlying mechanism. Here, we use an existing biophysically plausible STN–GPe network model which we have augmented with a rule for spike-timing-dependent plasticity (STDP) for the inhibitory connections within globus pallidus pars externa (GPe). We explore the role of plasticity in stabilizing firing patterns. Moreover, we investigate how STN stimulation should be applied, such that it exploits STDP most effectively to bring the network in a less synchronous state. An STDP rule that down-/up-regulates the synaptic weights between GPe cells when they fire in synchronized/uncorrelated manner, stabilizes network states. Both a healthy state with desynchronized dynamics and a PD state with synchronized dynamics stably coexist. Our results suggest that when a traveling wave short-duration desynchronizing stimulation is applied sufficiently long and with sufficiently high amplitude, it may profit from STDP to train the network to fire in a less pathological manner. In contrast, STDP has a negative effect when continuous stimulation is employed, in the sense that the network becomes more synchronized when stimulation is switched off. Since with this kind of stimulation most of the time DBS is turned off, it saves battery power and it leads to fewer negative side effects of DBS in comparison to the traditional continuous high frequency stimulation[1].

[1] The material presented in this Chapter is in preparation for submission to *Journal of Computational Neuroscience*.

2.1 Introduction

As a consequence of the dopamine depletion in Parkinson's disease (PD), neurons in the basal ganglia (BG) tend to discharge in bursts, have altered firing rates and exhibit abnormally synchronized oscillatory activity at multiple levels of the BG-cortical loop, see reviews by Hammond et al. [80], and Galvan and Wichmann [61]. In particular, single-unit and/or local field potential (LFP) recordings have demonstrated that the external part of the globus pallidus (GPe) and the subthalamic nucleus (STN) exhibit a tendency to oscillate and synchronize at low frequencies (3–30 Hz) in the parkinsonian state [20, 34, 130, 155, 176]. The pathophysiological beta-frequency oscillations (13–30 Hz) are thought to be responsible for bradykinesia and rigidity in PD patients [111, 113, 175, 223], whereas the 3–10 Hz oscillations have been associated with tremor [44, 120, 197, 207].

High frequency (> 100 Hz) deep brain stimulation (DBS), especially of the STN, is an established therapy to reduce PD motor symptoms, when medication does no longer produce satisfying results or induces dyskinesia [16, 76]. With optimized stimulation parameters, established empirically [146, 177, 219, 220] and confirmed theoretically [38, 53, 137], STN–DBS is able to reduce dyskinesia and to improve motor symptoms including tremor, bradykinesia and rigidity [109, 179]. However, STN–DBS is less effective for gait disturbance and postural instability, and its therapeutic benefit may decline over time [109, 179]. Furthermore, STN–DBS may cause adverse effects including cognitive decline, speech difficulty, instability, gait disorders and depression [179]. To overcome these limitations of high frequency DBS and to design improved stimulation protocols, it is important to understand how high frequency DBS works. Unfortunately, the fundamental physiological mechanism by which DBS prevents pathophysiological responses of the motor network are still not understood. It is suggested that high frequency stimulation leads to somatic inhibition of neurons that are close to the electrical field, while simultaneously afferent and efferent axons may be excited. Both cellular and network effects may contribute to the overall clinical effect of DBS. Moreover, stimulation does not necessarily have to restore the network to a pre-pathological/healthy state, but should allow improvement in Parkinson's symptoms. McIntyre and Hahn [136] hypothesize that high frequency stimulation disrupts or desynchronizes the pathological activity by changing the underlying dynamics of the stimulated brain networks, which can be achieved via activation, inhibition, or lesion.

A clinical observation is that when stimulation is turned off the symptoms do not return instantaneously, but revert back gradually: tremor within minutes, bradykinesia and rigidity within half an hour to an hour, and axial signs within 3 to 4 hours [210]. When the stimulator is turned on again, the symptoms improve in the same

order, but faster than their rate of deterioration. This observation implies that the DBS-induced dynamical changes have a long-lasting effect, and it suggests that different pathophysiological mechanisms underlie the major PD-symptoms. A neural mechanism that can achieve such long-lasting effects is synaptic plasticity. Thus, DBS may start a cascade of long term changes, up-regulating some synapses and down-regulating others, that eventually disrupt the pathophysiological mechanism and slowly reverse when the stimulator is switched off. To exploit this synaptic plasticity effect of DBS, Tass and colleagues have proposed a coordinated reset (CR) stimulation, which is a short-duration desynchronizing stimulation protocol that leads to a therapeutic synaptic reshaping of neuronal networks [208]. In epileptic hippocampal slices of a rat it was shown that the CR-stimulation has long-lasting desynchronizing effects [209].

To steer novel stimulation protocols that are based on reshaping synaptic connections, it is important to know in which circuitry and how the pathological activity is generated. However, the mechanisms underlying the pathological activity in PD are still debated. Using organotypic culture preparation with GPe and STN with frontomedial cortex and dorsolateral striatum, Plenz and Kital [170] conclude that the observed correlated activity in STN and GPe is caused by their interaction between, rather than being driven by an external source. It is hypothesized that autonomous pacemaking in GPe neurons counterbalances the natural tendency of the reciprocally connected STN–GPe network to switch into a pathological synchronous, rhythmic bursting as seen in PD. Computational models show that increasing the inhibitory input to the GPe, due to dopamine depletion in the striatum, leads to a suppression of the autonomous GPe activity, thereby creating PD activity [114, 211]. In contrast, *in vivo* experiments give evidence that synchronized beta oscillations associated with the parkinsonian state are driven from motor areas of the cortex via the hyperdirect cortico-subthalamic pathway [128, 131, 189]. Recently, Ammari et al. [5] have shown in dopamine-depleted BG slices of mice that STN neurons, without synaptic inhibition from GPe, generate bursts of excitatory postsynaptic currents (EPSCs) in response to a single electrical stimulus. Such a burst of EPSCs leads to bursts of spikes in the STN. They hypothesize that the glutamatergic network within the STN, that is under negative control of dopamine, amplifies the STN responses to incoming excitation in the dopamine-depleted BG by generating bursts of spikes that will in turn generate bursts of spikes in GPe neurons. However, such a glutamatergic network within STN has not been shown to exist in humans.

There exist many different computational BG-models in the literature, each with one of the above mechanisms to regulate its state. Rubin and Terman [181] have been the first to analyze the DBS induced network effects with a biophysically plausible BG-model. Their model has well defined physiological and pathological states, that

rely on the strength of synaptic connections within the GPe and the striatal input to the STN–GPe network, supporting the STN–GPe pacemaker hypothesis. They predicted that STN–DBS induced high frequency tonic firing of STN would regularize BG input to thalamus, thereby restoring the thalamic relay function. A recent computational study by Hahn and McIntyre [72] hypothesizes that parkinsonian beta activity within the STN–GPe network has a cortical origin. Their network model was able to switch from parkinsonian to healthy activity by reducing the influence of the cortical beta input. They hypothesize that STN–DBS should reduce the GPi bursting to a certain level in order to be therapeutic and that the reduction is dependent upon both stimulation frequency and the volume of STN activation. Since the models do not contain an appropriate slow timescale, these computational studies cannot explain the long-lasting effects of DBS. When the stimulation was turned off, their models return immediately back to the parkinsonian state.

The goal of this study is to investigate, with a biophysically plausible model that can display both healthy and parkinsonian activity, the role of synaptic plasticity in stabilizing firing patterns in the BG. In particular, we will show how DBS can be used to steer the network through a landscape of plasticity-induced multistability, i.e. healthy and parkinsonian states. To our best knowledge, the only available spike generated BG-model with synaptic plasticity is the model of Hauptmann and Tass [82]. The authors model a population of bursting STN neurons interacting with a population of GPe neurons. Specifically, the dynamics of each STN neuron are described by a Morris–Lecar model, while the GPe population is modeled as a slow feedback current to the STN. In this setup, the STN cells fire bursts regulated by the GPe current. Furthermore, each STN neuron projects to all other STN cells. These are excitatory connections subject to synaptic plasticity, which is controlled by the timing of the bursts. The model exhibits a stable healthy state characterized by desynchronized STN bursts and weak connectivity within the STN, and a stable pathological state characterized by synchronized STN bursts and strong connectivity within the STN. They show that stimulation of the STN neurons according to their proposed short-duration desynchronizing stimulation protocol reduces the mean synaptic weight and shifts the network to a healthy state. Their model relies crucially on the presence of all-to-all connections within the STN that become weakened by desynchronizing stimuli. However, there is hardly evidence for the existence of such connections within the STN [226], but see Hammond and Yelnik [79], who observed an intranuclear axonal collateral in only one out of a total of ten STN neurons.

In this Chapter, we extend this approach by explicitly modeling the GPe neurons, introducing spike-timing-dependent plasticity (STDP) for the experimentally established inhibitory connections between GPe cells and leaving out the intra-STN

connections. The dynamics of STN and GPe is governed by the biophysically plausible single compartment models as proposed by Rubin and Terman [181]. Finally, we connect these cell models together via a sparse structured architecture as proposed by Rubin and Terman [181]. In this study, we investigate whether and how STN stimulation can control the synaptic plasticity such that either a stable healthy state is reached or a metastable state with irregular dynamics that slowly returns to the parkinsonian state when stimulation is turned off. We hypothesize that STN stimulation can disrupt the pathological activity if it decreases the rate of coincidence of GPe spikes, thereby up-regulating the synaptic coupling between the GPe cells.

2.2 Methods

2.2.1 Neuron models for STN and GPe

The dynamics of each STN cell and each GPe cell are represented by a single compartment conductance-based model as proposed by Rubin and Terman [181, 211]. To produce an action potential each cell model includes a sodium current (I_{Na}), a potassium current (I_{K}) and a leak current (I_{L}). Each cell model contains also the following types of ionic currents (I_{ion}): a calcium activated, voltage independent afterhyperpolarization potassium current (I_{AHP}), a high threshold calcium current (I_{Ca}) and a low threshold T-type calcium current (I_{T}). In addition to these ionic currents and leak current each STN and GPe cell receives synaptic current (I_{syn}) and applied current (I_{app}). The rate of change of the membrane potential (V_{m}) for each cell is given by:

$$C_{\mathrm{m}} \frac{\mathrm{d}V_{\mathrm{m}}}{\mathrm{d}t} = -I_{\mathrm{L}} - I_{\mathrm{ion}} - I_{\mathrm{syn}} + I_{\mathrm{app}}, \tag{2.1}$$

where C_{m} is the membrane capacitance. We use the equations and parameter values for the leak current and ionic currents as described in Terman et al. [211], adopting the modifications of Rubin and Terman [181] and those in Guo and Rubin [69] to match more closely *in vivo* firing patterns (Appendix A).

2.2.2 Network architecture

For the synaptic connections between the STN and GPe cells we use the structured, sparsely connected architecture given in Rubin and Terman [181] (Figure 2.1). The network consists of 2 subpopulations, each including 8 STN neurons and 8 GPe neu-

rons that are connected to each other via weak synaptic connections. Each subpopulation can be further divided into four groups of four neurons (Figure 2.1, STN 1, STN 2, GPe 1 and GPe 2), such that neurons within the same group provide synaptic inputs to the same target groups. Each STN group sends excitatory input to one GPe group of its owns subpopulation and also provides weak excitatory input to the corresponding group in the other subpopulation. Each GPe group inhibits one group of STN neurons of its own subpopulation. Within each subpopulation, there are also local inhibitory connections between GPe neurons. Finally, each cell (GPe and STN) receives a constant applied current input (I_{app} in equation (2.1)) representing net input from other brain structures. These currents are used to tune the firing rates and the network state, see Section 2.2.3.

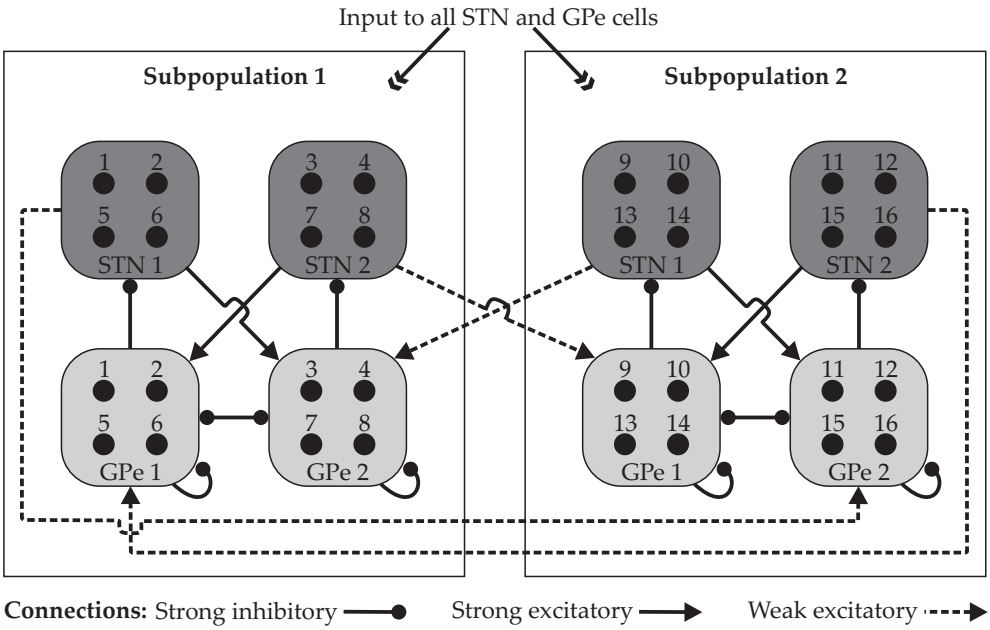

Figure 2.1 The structured, sparsely connected network architecture adopted from Rubin and Terman [181]. Based on the connectivity, the network is divided in to two subpopulations, each consisting of two STN groups and two GPe groups. Each group contains four cells, represented by solid circles and numbered separately for each cell type, projecting to and receiving input from the other groups as illustrated by the lines. A solid line denotes a strong connection, whereas a dashed line denotes a weak connection. Lines ending with arrows and open circles indicate excitatory glutamatergic and inhibitory GABAergic synaptic connections, respectively. Each GPe cell receives inhibitory input from two other GPe cells of its own subpopulation, and receives excitatory input from three STN cells, two of which from its own subpopulation. Each STN cell receives inhibitory input from two GPe cells of its own subpopulation. In addition to the synaptic inputs, all cells receive direct current injection as indicated with the two double arrowed lines. Note that the connections of individual cells are not shown.

As in Rubin and Terman [181] the synaptic current from $j \in J$ presynaptic cells of nucleus α to a postsynaptic cell i of nucleus β is modeled as:

$$I^i_{\alpha\to\beta} = g_{\alpha\to\beta}(V^i_{\mathrm{m},\beta} - E_{\alpha\to\beta}) \sum_{j=1}^{J} w_{ij} s^j_\alpha, \tag{2.2}$$

where $g_{\alpha\to\beta}$ and $E_{\alpha\to\beta}$ are the maximal synaptic conductance and reversal potential for connections from presynaptic cells of nucleus α to postsynaptic cells of nucleus β, respectively, with α and β representing STN or GPe. The summation is taken over cells in nucleus α with the synaptic weight (w_{ij}) that project to cell i of nucleus β. For both STN and GPe cells the kinetics of the rise and decay of the synaptic variable s^j_α are described by a first order process:

$$\frac{\mathrm{d}s^j_\alpha}{\mathrm{d}t} = \mathrm{A}_\alpha(1 - s^j_\alpha) S_\infty(V^j_{\mathrm{m},\alpha}) - \mathrm{B}_\alpha s^j_\alpha, \tag{2.3}$$

where $S_\infty(x) = 1/(1 + \exp(-(x - \theta_\alpha)/\sigma_\alpha))$. The kinetic parameters for STN and GPe are $[\mathrm{A}_\alpha, \mathrm{B}_\alpha, \theta_\alpha, \sigma_\alpha] = (5,\ 1,\ -9,\ 8)$, $(2,\ 0.04,\ -37,\ 2)$, respectively.

2.2.3 *Healthy and parkinsonian states of the network*

In PD patients and in animal models of PD, electrophysiological changes have been observed in neurons of the basal ganglia, including a tendency of neurons to discharge in bursts, increased interneuronal synchrony and oscillatory activity (Galvan and Wichmann [61], and references therein). As demonstrated in Terman et al. [211] a STN–GPe network model with the above mentioned single cell models can display correlated rhythmic activity, uncorrelated irregular spiking activity and propagating waves, depending on the architecture and strengths of synaptic connections between the STN and GPe, within the GPe and depending on the input to the network. Moreover, they have shown that a STN–GPe network connected via a sparse structured architecture is able to mimic a healthy situation where cells fire irregularly and activity is uncorrelated as well as a PD situation where cells fire bursts of action potentials at low frequency and where activity is highly correlated (clustered). Our network architecture has a sparse structured pattern of connections. The network can display both healthy and PD activity, depending on the strength of the synaptic connections between the cells and the inputs to them.

We determine appropriate coupling and input parameters such that the network model activity mimics either the experimentally observed activity in PD or healthy

conditions. First, we adjust the synaptic strengths for the connections from GPe to STN, STN to GPe and within the GPe by changing their maximal synaptic conductance ($g_{\mathrm{GPe}\to\mathrm{STN}}$, $g_{\mathrm{STN}\to\mathrm{GPe}}$ and $g_{\mathrm{GPe}\to\mathrm{GPe}}$), and the value of the applied current for both cell types ($I_{\mathrm{app,STN}}$ and $I_{\mathrm{app,GPe}}$) to model the PD activity. Except for $g_{\mathrm{GPe}\to\mathrm{GPe}}$, we take the values given by Guo and Rubin [69]: $I_{\mathrm{app,STN}} = 0$ µA cm^{-2}, $I_{\mathrm{app,GPe}} = -1.2$ µA cm^{-2}, $g_{\mathrm{GPe}\to\mathrm{STN}} = 0.9$ mS cm^{-2} and $g_{\mathrm{STN}\to\mathrm{GPe}} = 0.18$ mS cm^{-2}. The value for $g_{\mathrm{GPe}\to\mathrm{GPe}}$ is set to 0.1 mS cm^{-2}.

Second, having parameters such that the network displays PD-like activity, we look for a different parameter set for the healthy situation. Following the approach of Rubin and Terman [181], we vary only $I_{\mathrm{app,GPe}}$ and $g_{\mathrm{GPe}\to\mathrm{GPe}}$, leaving the other three parameters ($I_{\mathrm{app,STN}}$,$g_{\mathrm{GPe}\to\mathrm{STN}}$ and $g_{\mathrm{STN}\to\mathrm{GPe}}$) unchanged, for this transition. No synaptic plasticity is involved so far.

2.2.4 *Synaptic plasticity*

The model we described above considers the synaptic weight (w_{ij}) between presynaptic cell j to a postsynaptic cell i to be static. It is set equal to 1 for all connections, except for the weak excitatory connections which are set to 0.2. However, several experiments have shown that the strength of synaptic connections changes depending on the relative spike timing of the pre-synaptic and post-synaptic neurons within a short time window [27, 56, 127, 132, 192, 231]. This kind of synaptic plasticity is referred to as *spike-timing-dependent plasticity* (STDP). Although STDP has been described and observed extensively for excitatory synapses, it has also been observed in inhibitory synapses [71, 86, 227]. Experimental results show alterations in the coupling strength between GPe cells in parkinsonian conditions [158, 195]. In this study, the inhibitory connections within the GPe cells are subject to STDP. The synaptic weight (w_{ij}) is updated with an additive nearest-spike pair-based STDP rule:

$$w_{ij}(t_{n+1}) = w_{ij}(t_n) + \delta \Delta w_{ij}(\Delta t_{ij}), \tag{2.4}$$

where δ is the update rate and Δw_{ij} is the synaptic modification, which depends on the temporal difference $\Delta t_{ij} = t_i - t_j$ between the nearest onsets of the spikes of the pre-synaptic neuron j and post-synaptic neuron i. In experiments, the observed plasticity time windows, describing the relation between the time difference and the synaptic modification, vary substantially [40, 71, 86, 227]. Following Popovych and Tass [171] we use an asymmetric time window for STDP of inhibitory synapses, given by:

$$\Delta w_{ij}(\Delta t_{ij}) = \begin{cases} -\beta_1 \exp(-\frac{\gamma_1 |\Delta t_{ij}|}{\tau_{\text{STDP}}}), & \Delta t_{ij} \geq 0, \\ \beta_2 \frac{|\Delta t_{ij}|}{\tau_{\text{STDP}}} \exp(-\frac{\gamma_2 |\Delta t_{ij}|}{\tau_{\text{STDP}}}), & \Delta t_{ij} < 0. \end{cases} \tag{2.5}$$

This is an anti-Hebbian STDP update window (Figure 2.2A), i.e. the synaptic strength between the GPe cells is potentiated or depressed depending on whether the post-synaptic spike advances or comes after the pre-synaptic spike, respectively [171]. An anti-Hebbian weight modification is observed for inhibitory synapses [40, 86]. In our case the weight increase and decrease are independent of the present weight of a synapse. Therefore, an upper bound of 0.6 and a lower bound of 0.0001 is placed on each synaptic weight to avoid unbounded growth and negative conductances.

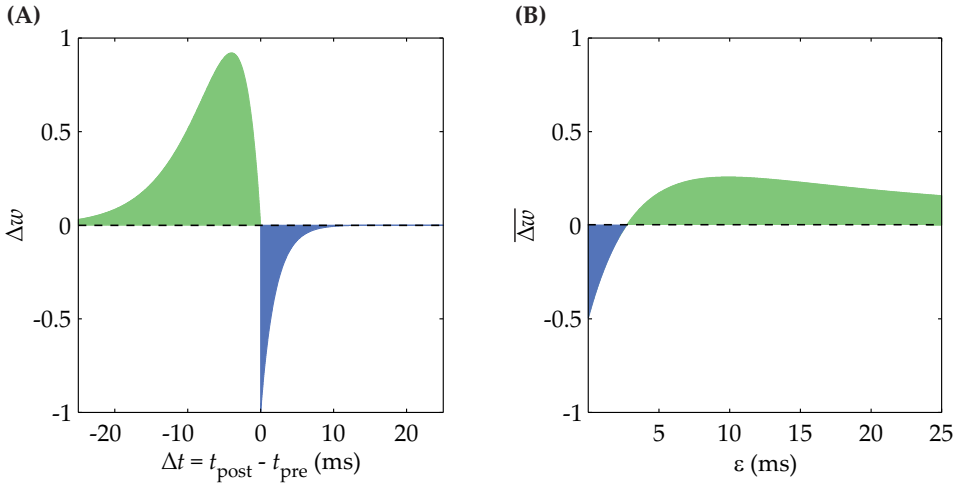

Figure 2.2 Time window for STDP of inhibitory synapses (**A**) and its effective time window (**B**) as defined by Popovych and Tass [171]. The STDP time window shows the prescribed change in synaptic weight changes as a function of the time difference between the pre- and post-synaptic spikes ($\Delta t = t_{\text{post}} - t_{\text{pre}}$). The synaptic weight is potentiated when a post-synaptic spike precedes a pre-synaptic spike, and depressed when a pre-synaptic spike precedes a post-synaptic spike. The effective time windows shows whether on average strengthening (uncorrelated spike trains, ϵ large) or weakening (correlated spike trains, ϵ small) of the synapse occur for uniformly distributed $\Delta t \in [-\epsilon, \epsilon]$.

In Popovych and Tass [171] the net effect of STDP, denoted as $\overline{\Delta w}$, resulting from the difference between the time windows for depression and potentiation [106], is calculated for uniformly distributed relative firing times Δt in the interval $\Delta t \in [-\epsilon, \epsilon]$ by:

$$\overline{\Delta w(\epsilon)} = \frac{1}{2\epsilon} \int_{-\epsilon}^{\epsilon} \Delta w(\xi) \mathrm{d}\xi. \tag{2.6}$$

The parameter values for the STDP window can be tuned such that the net effect of STDP results in down- or up-regulation of the synaptic weights between GPe cells when they fire in synchrony (Δt is narrowly distributed, i.e. ϵ small) or in uncorrelated manner (Δt is broadly distributed, i.e. ϵ large), respectively [171]. The parameter values for the STDP window are given in Table 2.1 and $g_{\mathrm{GPe}\to\mathrm{GPe}}$ (maximal synaptic conductance) is set to 1 mS cm^{-2} in the simulations with plasticity. Note that the coupling strength between GPe cells is given by the product of $g_{\mathrm{GPe}\to\mathrm{GPe}}$ and w_{ij} in simulations with STDP, whereas the coupling strength in simulations without STDP is given by $g_{\mathrm{GPe}\to\mathrm{GPe}}$.

Table 2.1 Parameters used in implementation of STDP

Parameter	Value
β_1	1
β_2	5
γ_1	4
γ_2	2
τ_{STDP}	8
δ	0.004

2.2.5 *Analysis of network activity*

The PD state in our model is characterized by synchronized activity within each cluster and cells firing in a burst-like pattern. These characteristics are readily observed visually in a raster plot of spike times. However, to quantify the level of network synchrony and burstiness, as well as how they are affected by stimulation and network parameters, we used the quantitative measures as described next.

Number of principle components

There are several measures that quantify the level of synchrony in the network, i.e. the extent to which cells in a population (GPe or STN) spike at the same points in time, including both firing time measures [115, 167, 200] and continuous time measures [66]. Most of these measures are not really suitable to assess the level of population synchrony if the population consists of clusters of cells which fire approximately synchronously within each cluster. The method proposed in Best et al. [24] is able to detect the number of synchronized clusters in a population. In short, the method is

based on principle component analysis (PCA), which means that eigenvectors (v_i) of the covariance matrix for the mean-adjusted voltage traces are computed and subsequently sorted by decreasing eigenvalues. Projection of the dataset onto the subspace generated by the first eigenvectors $\{v_1, v_2, \ldots, v_{n-1}, v_n\}$, $n \leq N$, where N is the number of STN (or GPe) cells in the network, captures the maximally possible variance within an n-dimensional subspace. After a certain linear transformation, n variables are sufficient to describe a certain percentage of the data. In terms of our network, if for example two variables will describe most of the population activity, it strongly suggests the existence of two clusters. The fraction of the variation in the data that is captured by the subspace spanned by the n largest eigenvectors equals η_n, where

$$\eta_n = \frac{\lambda_1 + \lambda_2 + \ldots + \lambda_n}{\lambda_1 + \lambda_2 + \ldots + \lambda_N}, \qquad n \leq N. \tag{2.7}$$

We report the number of principal components (eigenvectors) required to capture at least 90% of the variation in the data. Because of memory issues, we store only the spike times of the neurons instead of their membrane voltage traces. To perform PCA, each spike train i is transformed into a continuous waveform $\tilde{x}_i$ by convolving each spike with a Gaussian filter with a standard deviation $\sigma = 7.5$ ms,

$$\tilde{x}_i(t) = \sum_{k=1}^{S_i} \exp\left(-\frac{(t - t_k^i)^2}{\sigma^2}\right), \tag{2.8}$$

where S_i is the number of spikes in spike train i and t_k^i is the spike time of kth spike in spike train i.

Mean burst rate

The burst rate of individual neurons is estimated as the average burst count over the last 10 s simulation period. The mean population burst rate is then obtained by averaging the burst rates of all STN (or GPe) neurons. To detect bursts in the ordered sequences of spike times we use the modified Poisson surprise method of Hahn et al. [73] with a minimum surprise index of 1.5 and a minimum number of 3 spikes per burst.

2.2.6 Deep brain stimulation

One of our goals is to investigate how high frequency stimulation reshapes the synaptic conductances in our network model with STDP, thereby changing the firing pattern. We apply an external stimulation signal I_{stim} to the STN neurons, such that the equation governing the voltage of a STN cell (Equation 2.1) becomes:

$$C_{\text{m}}\frac{\mathrm{d}V_{\text{m}}}{\mathrm{d}t} = -I_{\text{L}} - I_{\text{ion}} - I_{\text{syn}} + I_{\text{app}} + I_{\text{stim}}. \tag{2.9}$$

As in Guo and Rubin [69] the external stimulation signal consists of a train of high frequency pulses,

$$P(t) = a_0 H_\infty(\sin(\omega_0 t) - a_1), \tag{2.10}$$

where $H_\infty(x) = 1/(1+\exp(-1000x))$ is a smooth approximation of the Heaviside step function, a_0 is the amplitude of the injected current and t is the time in milliseconds. Parameters $\omega_0 = 0.93$ and $a_1 = 0.7$, result in a pulse train with a frequency of 148 Hz ($1000\omega_0/2\pi$) and a pulse width of 1.7 ms ($(\pi - 2\arcsin(a_1))/\omega_0$).

In this study, the pulse train $P(t)$ is administered according to two different protocols. We apply the standard DBS, i.e. continuous stimulation, in which all STN cells receive exactly the same stimulation signal $I_{\text{stim}} = P(t)$. The other protocol is the so called coordinated reset (CR) stimulation, in which the four STN groups defined in Section 2.2.2 receive pulse trains via four different stimulation electrodes as show in Figure 2.3A. During a stimulation interval of length T_{s}, stimulation at electrode k is turned on and off as specified by the periodic step function:

$$\begin{aligned} F_k(t) = {} & H_\infty(\sin(2\pi(t-(k-1)\tau_{\text{CR}})/\rho))\times \\ & H_\infty(\sin(-2\pi(t-(k-2)\tau_{\text{CR}}+1)/\rho)), \qquad\qquad k=1,\ldots,4, \end{aligned} \tag{2.11}$$

where the period of the step function equals $\rho = \tau_{\text{CR}} + a_2\tau_{\text{CR}}$, such that τ_{CR} and $a_2\tau_{\text{CR}}$ are the ON period ($F_k(t) = 1$) and the OFF period ($F_k(t) = 0$) of the electrode, respectively (Figure 2.3B). We assume that each of the four neurons in a STN group receives exactly the same stimulation signal $I^k_{\text{stim}} = F_k P(t)$, originating only from its own electrode k. Although the stimulation administered at the four different electrodes has the same period ρ, with the same pulse train supply within the ON period, the ON periods at the four electrodes do not coincide because of the constant phase shift between the activation of any two consecutive stimulation electrodes (Figure 2.3B). This phase shift is set equal to the ON period of the electrode (τ_{CR}) in Equation 2.11,

which implies that $a_2 \geq 1$ as the off period cannot be shorter than the phase shift. In our CR-stimulation protocol, we set $\tau_{CR} = 45$ ms, which is approximately one fourth of the period of STN bursting activity.

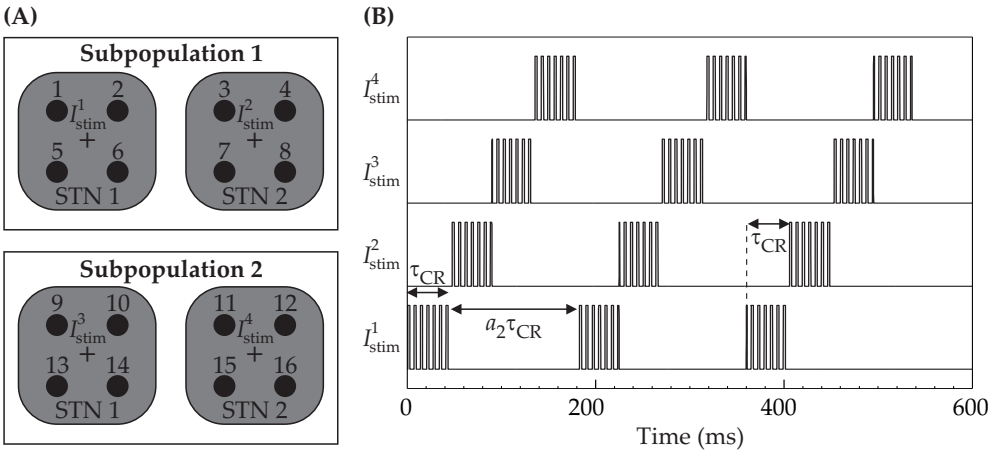

Figure 2.3 Stimulation protocol for coordinated reset (CR). (**A**) Schematic representation of the administration of $I^k_{stim}, k = 1,\ldots,4$, via four electrodes, indicted by the markers $+$, to the four STN groups defined in Section 2.2.2. Each STN group receives its own stimulation signal I^k_{stim}. (**B**) Time series of the stimulation signals. Within stimulation ON periods of length τ_{CR}, the stimulation signal consists of a train of high frequency pulses, given by Equation 2.10. The stimulation signal vanishes within stimulation OFF periods of length $a_2\tau_{CR}$. All stimulation signals are identical, but having a phase shift τ_{CR} between any two consecutive numbered stimulation signals. In this example $\tau_{CR} = 45$ ms and $a_2 = 3$.

2.2.7 Simulation

We implement the STN–GPe network model in MATLAB (Mathworks, Inc., Natick, MA, USA) and use the Euler method with fixed step size of 0.01 ms to integrate it. To explore the effect of the coupling strength between GPe cells ($g_{GPe\to GPe}$ or $w_{initial}$) and $I_{app,GPe}$ on the network dynamics, we simulate the network without plasticity for 12 s and the network with plasticity for 1000 s, for each setting. Stimulation is only administered to a clustered solution of the network with STDP where the GPe cells are weakly coupled to each other. Therefore, we set $w_{initial}$ to 0.1 and $I_{app,GPe}$ to -1.2 µA cm^{-2} in simulations with DBS and we run them for 1600 s with stimulation starting at $t = 1020$ s. Only the last 10 s of each simulation are used to compute the mean burst rate and the number of principle components.

2.3 Results

2.3.1 The STN–GPe network without plasticity

To obtain PD activity in the structured sparse connected network of 16 STN and 16 GPe cells without synaptic plasticity we adopted the parameters for coupling and the applied currents parameters from Guo and Rubin [69], except for $g_{\mathrm{GPe}\to\mathrm{GPe}}$ which was set to 0.1 mS cm^{-2}. Using these values, the STN cells in our network segregate into two rhythmically bursting clusters (checkerboard pattern), with synchronized activity within each cluster. In particular, the STN neurons within the same group of subpopulation 1 (Figure 2.1) and neurons in the corresponding group of subpopulation 2 synchronize their (bursting) activity. GPe cells in our network show similar clustering and bursting, see Figure 2.4B. This is in accordance with the results reported in Guo and Rubin [69]. We need 2 PCA components for each population to capture 90% of the activity, reflecting the checkerboard activity (Figure 2.4C and D). In both STN and GPe populations the mean burst rate is approximately 5 Hz (Figure 2.4E and F).

This clustering may be understood directly from the network architecture. Suppose that cells of group STN 1 excite cells of group GPe 2 to initiate firing (Figure 2.1). As a result, the cells of GPe 2 inhibit the cells of STN 2 and prevent them from firing if the inhibition is strong enough. We are now in a situation where only cells of cluster '1' (STN 1 and GPe 2) are active. Once the cells of STN 2 escape this suppression, their firing excites cells of GPe 1, which in turn represses cells of STN 1. The cells of cluster '1' become silent and the cells of cluster '2' (STN 2 and GPe 1) are active. The cycle repeats with the roles of the clusters reversed. The mechanism underlying the escape of the STN cells from their suppressed state is the deinactivation of the inward I_{T} current [24, 211]. Persistent inhibition from the GPe cells results in an increase of the availability of I_{T} current in the STN cells, and allows the alternation of the clusters.

On one hand, the amount of inhibition from the GPe cells to the STN cells is crucial for the generation of clustered rhythmic activity. If, for example, the inhibitory connections within the GPe cells, $g_{\mathrm{GPe}\to\mathrm{GPe}}$, is high, then the GPe cells of cluster '1' will not be able to sufficiently inhibit the STN cells in the other cluster, causing them to escape and fire rebound bursts before the first cluster has completed. On the other hand, oscillatory activity within the reciprocally connected STN–GPe network can only emerge when STN cells become sufficiently active and the spontaneous firing of the GPe cells cannot counterbalance it. The strength of the applied current to the GPe neurons, $I_{\mathrm{app,GPe}}$, representing the net input from other brain structures, controls its spontaneous firing rate. Thus, lowering the inhibitory input $I_{\mathrm{app,GPe}}$ or

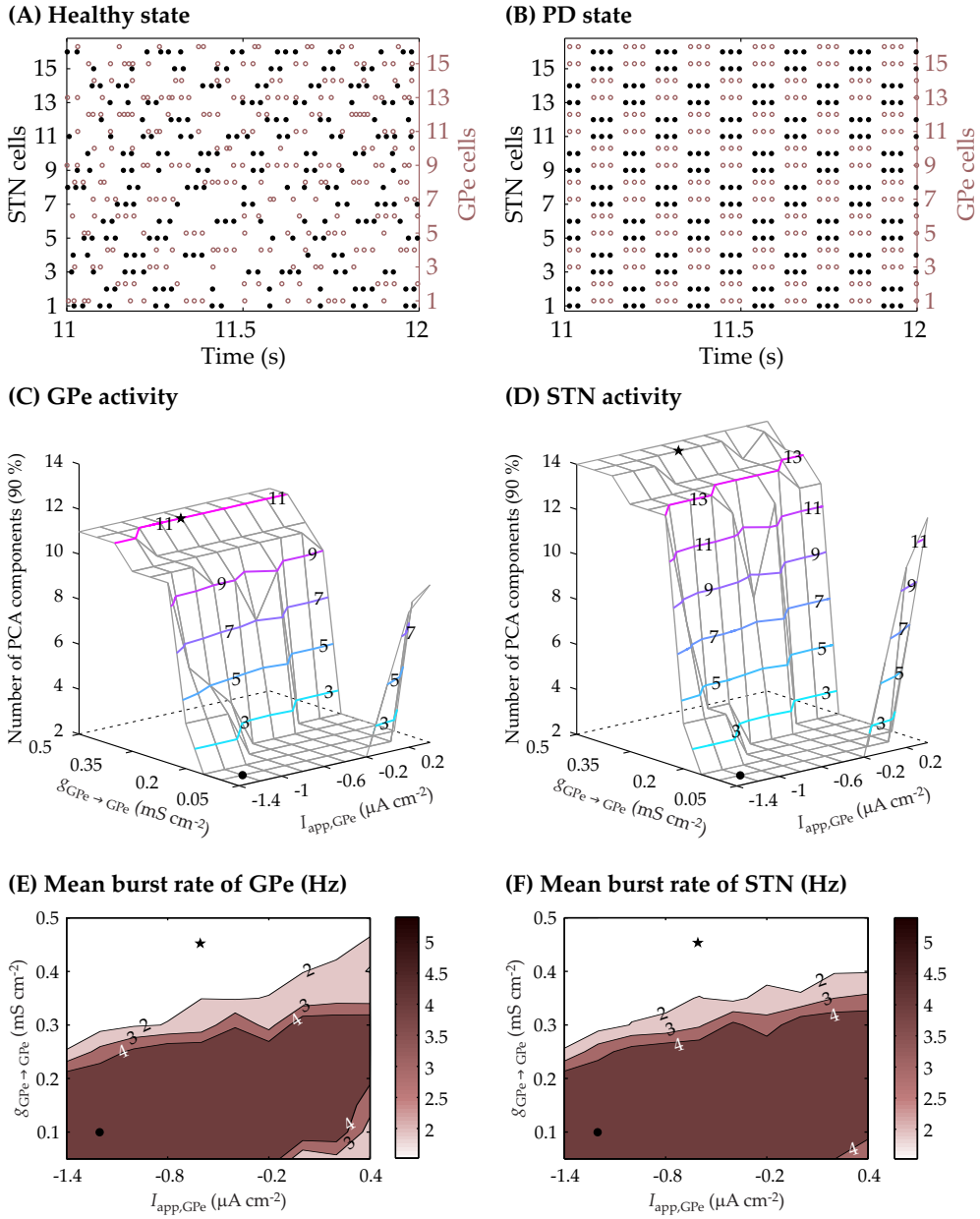

Figure 2.4 Behavior of the network without STDP for different choices for $I_{\text{app,GPe}}$ and $g_{\text{GPe}\to\text{GPe}}$. (**A**) and (**B**) show the spike times for all sixteen STN and GPe cells, illustrating the activity of the network in the two points indicated by $\star$ and $\bullet$ in (**C**)–(**F**). These points represent the healthy and PD state, respectively. In the healthy state the firing patterns of both types of cells are irregular and uncorrelated. In the PD state, cells fire in a bursty an clustered pattern around 5 Hz. The cell numbers correspond to the numbers in Figure 2.1. (**C**) and (**D**) are 3D contour plots of the number of PCA components required to capture at least 90% of the GPe and STN activity, respectively. (**E**) and (**F**) are contour plots of the mean burst rate of GPe and STN, respectively.

increasing the value of $g_{\mathrm{GPe}\to\mathrm{GPe}}$ can lead to the transition from a PD state to a more healthy state where the activity is irregular and uncorrelated. Due to dopamine loss in the striatum the level of inhibition to GPe is higher than in the healthy situation, which motivated the former parameter change. Rubin and Terman [181] based the change in intra-GPe inhibitory synaptic conductance on experimental results in rats [158, 195]. However, changes in conductances can either be the result of altered activity (via plasticity) or its cause [114].

In Figure 2.4A, $g_{\mathrm{GPe}\to\mathrm{GPe}}$ is increased from 0.1 to 0.45 mS cm^{-2} and $I_{\mathrm{app,GPe}}$ is increased from -1.2 to -0.6 µA cm^{-2}. As can be seen from the spike time raster plot of all sixteen STN and sixteen GPe, all cells display irregular firing times that are only weakly correlated. The activity in Figure 2.4A represents the healthy state of our network. For the GPe cells 11 PCA components (Figure 2.4C) are needed to capture 90% of the activity. For the STN cells 14 components are needed (Figure 2.4D), meaning that there is slightly more correlation between the GPe cells than between STN cells. The firing pattern of both cell types in the healthy state is less bursty (mean burst rate of 1–2 Hz) than in the PD state (mean burst rate of 5 Hz).

Figures 2.4C and D show how the level of synchrony in the GPe and STN changes as a function of $I_{\mathrm{app,GPe}}$ and $g_{\mathrm{GPe}\to\mathrm{GPe}}$. For both types of cells we distinguish clearly between two regions: one where almost all the components (10–14) are needed and one where only two components are needed. The region where we need 2 PCA components represents a synchronized state, whereas the other region represents a desynchronized state. The transition from the synchronized state to the desynchronized state is sharp when we increase $g_{\mathrm{GPe}\to\mathrm{GPe}}$ and keep $I_{\mathrm{app,GPe}}$ constant. The applied current $I_{\mathrm{app,GPe}}$ has a minor effect on the level of synchrony.

Figures 2.4E and F show the mean burst rate of the GPe and STN population as function of $I_{\mathrm{app,GPe}}$ and $g_{\mathrm{GPe}\to\mathrm{GPe}}$. For both populations, the mean burst rate depends mainly on $g_{\mathrm{GPe}\to\mathrm{GPe}}$. The STN and GPe bursting reduces quickly when the intra-GPe inhibitory synaptic conductance reaches a certain threshold. This threshold is around 0.25 mS cm^{-2} and depends mildly on $I_{\mathrm{app,GPe}}$.

2.3.2 *The STN–GPe network with plasticity*

The above mentioned results were obtained with a network where the synaptic connections between the cells are static. This network exhibits a healthy state characterized by desynchronized activity of both cell types and strong coupling between the GPe cells, and a PD state characterized by synchronized clusters of both cell types and weak coupling between the GPe cells. Thus, crucial for the network state is the synaptic strength of the inhibitory connections within the GPe. When these connec-

tions are regulated by a STDP rule, it may contribute to the stabilization of these states. These may coexist for the same value $I_{\text{app,GPe}}$ so that STDP leads to multiple stable synchronized and desynchronized states [171]. If STDP plays a role, it should support desynchronized dynamics in the healthy state and synchronized dynamics in the PD state. This would be the case if in the healthy state potentiation of the synaptic weights between GPe cells is favored, whereas in the PD state depression of these weights is favored.

Depending on the initial coupling strength between GPe cells, the network reaches either a stable healthy state (Figure 2.5A, $w_{\text{initial}} = 0.35$) or a stable PD state (Figure 2.5B, $w_{\text{initial}} = 0.1$). As expected, the synchronized dynamics of the PD state results in depression of almost all synaptic weights, thereby stabilizing the PD state (Figure 2.5B). The synaptic weights of connections between GPe cells of different clusters are not depressed, because the differences between their spike times are too large for the STDP rule. Although a number of weights strongly decay from their initial value in the healthy state, the mean synaptic weight is higher than initially (Figure 2.5A). Therefore, STDP has a positive effect in stabilizing the healthy state. The observed bimodal distribution of the weights in the healthy state is characteristic for uncorrelated spike trains subject to an additive STDP rule as we used here [147].

The effect of the initial coupling strength (w_{initial}) and $I_{\text{app,GPe}}$ on the final synchrony level (Figure 2.5C) and the mean burst rate (Figure 2.5D) of GPe cells are comparable to the corresponding result in the network without STDP where the coupling strength is fixed and given by $g_{\text{GPe}\to\text{GPe}}$ (Figure 2.4C and E, respectively). A major difference is that for high $I_{\text{app,GPe}}$ and low w_{initial} the network with STPD approaches the healthy state, whereas the network without STDP displays PD activity here. Thus, starting with w_{initial} low and $I_{\text{app,GPe}}$ high results in network dynamics that is not perfectly clustered at the beginning of the simulation. Due to STDP, this leads to potentiation of the weights, which in turn, further supports the declustering, which finally results in a stable desynchronized healthy state. On the other hand, the nearly clustered dynamics in a network without STDP is in the basin of attraction of the stable clustered PD state. STN cells show similar behavior (data not shown).

2.3.3 *Continuous stimulation versus CR-stimulation*

Depending on the original firing pattern, the network with STDP is 'learning' either pathological or healthy dynamics by adapting its pattern of the synaptic couplings between the GPe cells. As stimulation can change the firing pattern of the stimulated

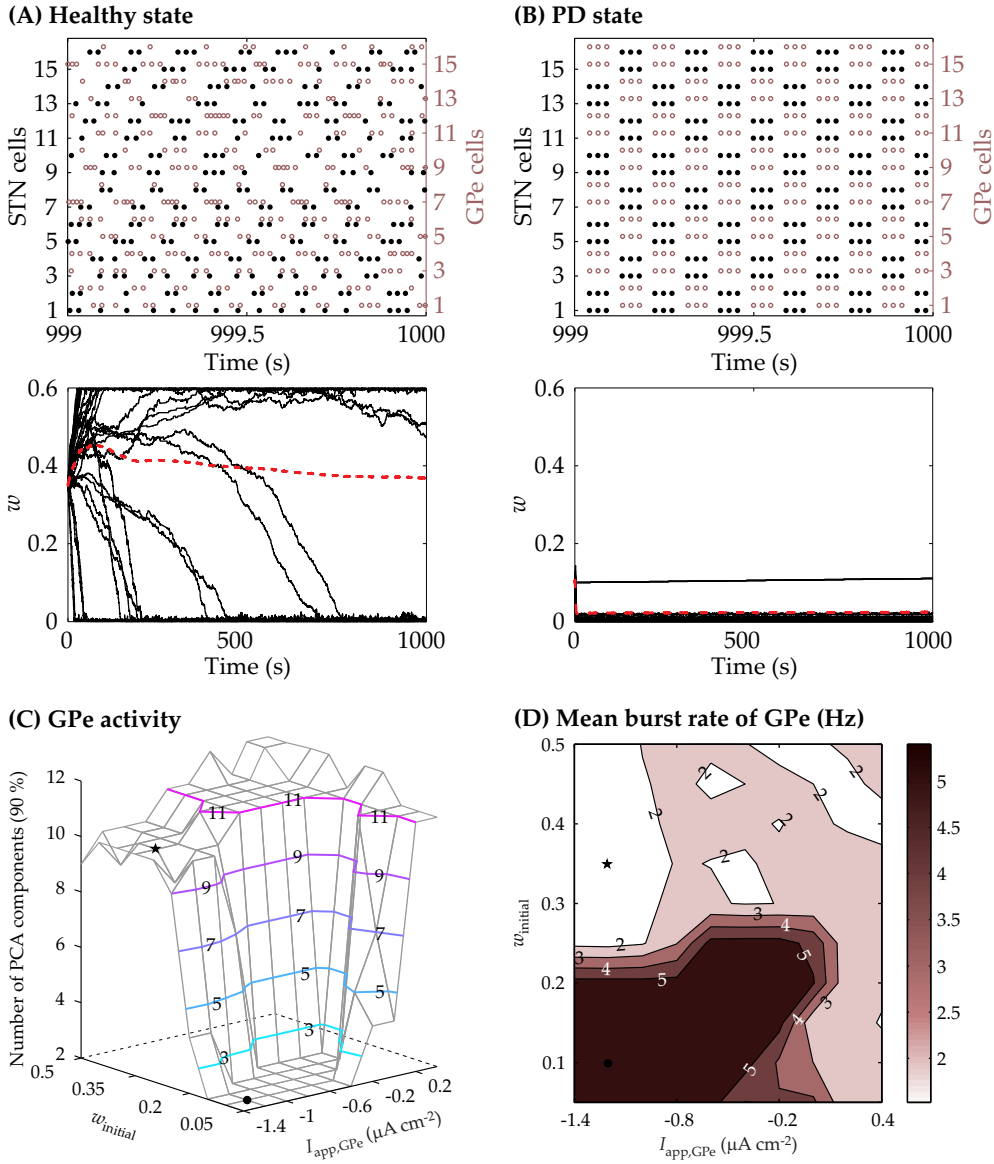

Figure 2.5 Behavior of the network with STDP for different choices for $I_{\text{app,GPe}}$ and w_{initial}. (**A**) and (**B**) illustrating the activity of the network in the two points indicated by ⋆ and • in (**C**)–(**D**), representing the healthy and PD state, respectively. The top panels show the raster plot of both cell types and the bottom panels show the time courses of the synaptic weights and the mean synaptic weight (red dashed line). The healthy state is characterized by asynchronous activity of both cell types and strong coupling between the GPe cells, whereas the PD state is characterized by synchronized clusters of both cell types and weak coupling between the GPe cells. The cell numbers correspond to the numbers in Figure 2.1. (**C**) and (**D**) are contour plots of the number of PCA components required to capture at least 90% of the GPe activity and the mean burst rate of GPe, respectively.

cells, it can be used to 'teach' the network with STDP to display more healthy activity. To illustrate the effect of continuous stimulation and CR-stimulation we first consider the STN–GPe network with STDP in a clustered solution where the GPe cells are weakly coupled to each other, see top panel of Figure 2.5B. For continuous stimulation all STN cells are locked to half of the stimulation frequency, which in turn, drives the GPe cells in the same tonic mode at 74 Hz (Figure 2.6A, bottom left). During continuous stimulation, the synaptic weights between the GPe cells quickly decay as a result of the synchronized activity of the GPe cells (Figure 2.6A, top). When the continuous stimulation is removed, the weights remain low. Continuous stimulation shifts the network from the two-cluster state to an even more synchronized state where all cells are perfectly synchronized and fire periodically at a rate of 21 Hz (Figure 2.6A, bottom right).

For the CR-stimulation we set a_2 to 3, such that it corresponds to the CR-protocol as proposed by Tass and colleagues. Now, the first stimulation site is turned on again when the last stimulation is turned off, i.e. during a cycle of length $\rho = 4\tau_{CR}$ each stimulation site is turned on once (Figure 2.3). The bottom left panel in Figure 2.6B shows the spike times of both cell types during CR-stimulation. Both cell types are entrained to the CR inputs, however, they sometimes fire single spikes in the OFF period of their stimulation site. This causes some desynchronization within the clusters, which in turn, leads to a gradually rise of mean synaptic weight during stimulation (Figure 2.6B, top). When CR-stimulation is switched off, the mean synaptic weight keeps rising until it reaches a value around 0.35. The distribution of the weights shows a similar bimodal distribution as we observed in the healthy state of the network (Figure 2.5A, bottom) and seems stable. Accordingly, the CR-stimulation steers the network away from a stable PD state to a stable healthy state (Figure 2.6B, bottom right).

2.3.4 Robustness of CR-stimulation

The above results show that CR-stimulation applied to a network with STDP in the PD state can reinforce the mean synaptic weight between GPe cells during stimulation. This results in a long-lasting redistribution of the weights and desynchronization corresponding to the healthy state. We test the robustness of the long-lasting effects of CR-stimulation with respect to the stimulation duration and amplitude as well as variation in the OFF period of the stimulation sites, which is controlled by a_2 (Equation 2.11). Figure 2.7 illustrates for three OFF periods the dependence of the effectiveness of CR-stimulation on stimulation duration and amplitude, via the number of PCA components and the mean burst rate measures for STN activity

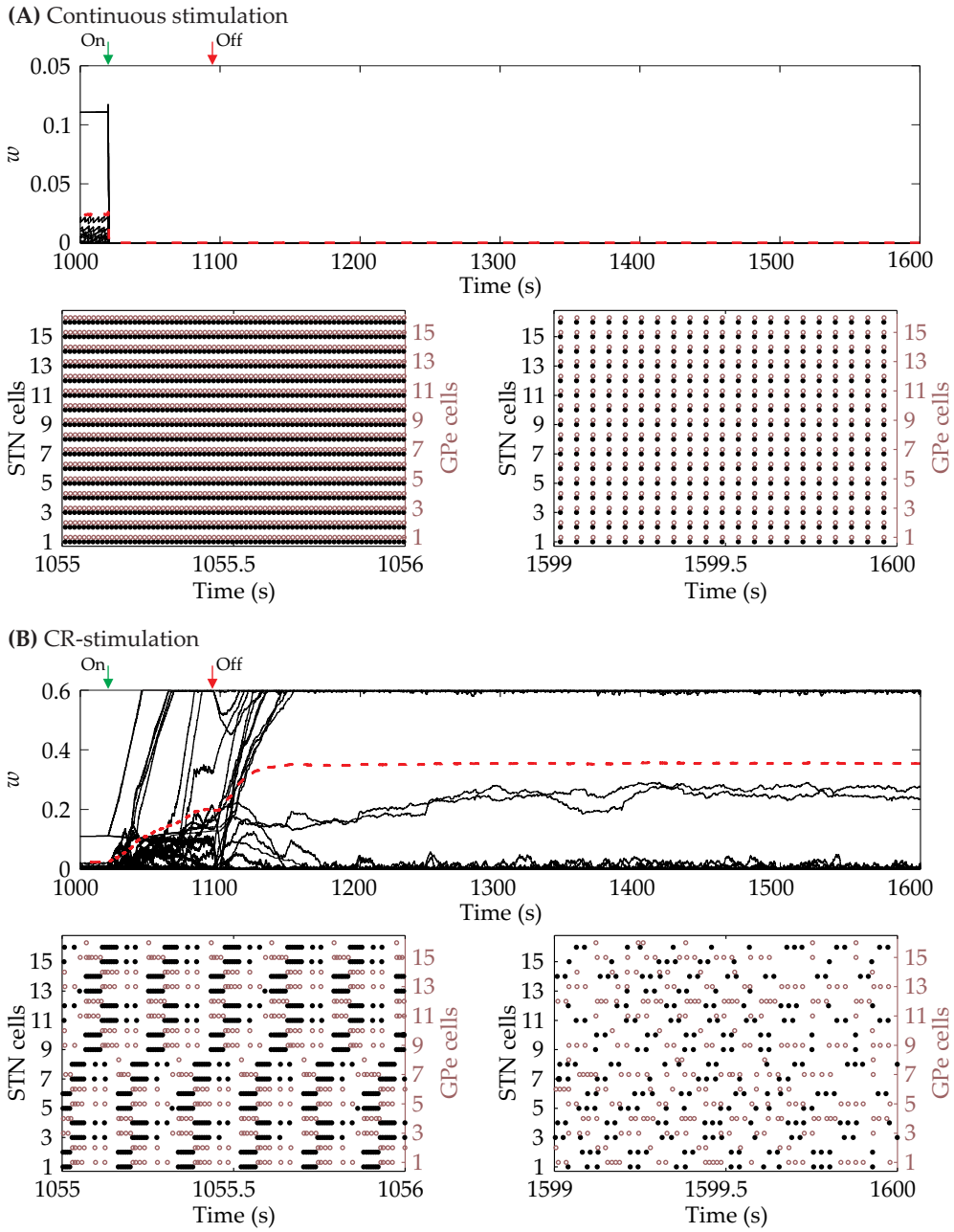

Figure 2.6 Effect of continuous stimulation (**A**) and CR-stimulation with $a_2 = 3$ (**B**) on the network activity. Stimulation is on from 1020 to 1095 s indicated by a green and a red arrow. Pulse train (2.10) is applied at 148 Hz with amplitude 100 µA cm^{-2} and pulse width of 1.7 ms. In both (**A**) and (**B**), the top panel shows the time courses of the synaptic weights and the mean synaptic weight (red dashed line). The bottom panels show spike times of both cell types during (left) and after (right) stimulation.

as described above. The CR-stimulation is considered effective when it induces the healthy state. Note that the healthy state in Figure 2.7 corresponds to regions where at least 10 PCA components are needed to capture 90% of the activity and where STN has a mean burst rate of lower than 2 Hz.

For the original CR-protocol as proposed by Tass and colleagues the stimulation is effective in the long duration, high amplitude region of the parameter space, see Figure 2.7A. As expected, the PCA and mean burst rate show that the stimulation duration and the amplitude used in Figure 2.6B belongs to the effective region of parameter choices, see Figure 2.7A, marker $+$.

Figure 2.8 depicts four examples of network dynamics from the region of parameter choices in Figure 2.7A (markers *) where CR-stimulation is not effective. For very low amplitude the clustering and bursting remains after stimulation (Figure 2.8A, right), whereas for slightly higher amplitude the bursting but not the clustering disappears after stimulation (Figure 2.8B, right). However, in both cases there is a phase shift between the checkerboard pattern of subpopulation 1 and the checkerboard pattern of subpopulation 2, such that we have a four-cluster state. This phase shift explains the reason why we need 4 PCA components to describe the STN activity in Figure 2.7A. For both cases the corresponding time course of the mean synaptic weight remains low (Figure 2.8A and B, left). Interestingly, the weights approach two different stable plateaus after stimulation with an amplitude of 60 μA cm^{-2} and duration of 75 s (Figure 2.8B, left), which may explain the disappearing of the bursts (two spikes instead of three spikes). Similar weight distribution and spike behavior is obtained when stimulation is applied with a higher amplitude (100 μA cm^{-2}), but a shorter duration (10 s), see Figure 2.8C. When we increase the duration from 10 s to 30 s, the CR-stimulation is only effective for subpopulation 2 (Figure 2.8D).

For the CR-protocol with OFF period $1.5\tau_{CR}$, the ON periods of the stimulation sites partially overlap with each other, leading to stimulation that is less desynchronous and closer to continuous. As can be seen from Figure 2.7B the stimulation is less effective compared to the original CR-protocol. Remarkable is the observation that one of the low amplitudes is effective and that it becomes ineffective when the amplitude is too high. When the OFF period is long, e.g. $3.8\tau_{CR}$, the stimulation does not work across the range of amplitude and duration we consider here. This is explained by the fact that for $a_2 > 3$, there is a period in which the whole network receives no stimulation. If this period is long, the weights may return to their original values of the PD state.

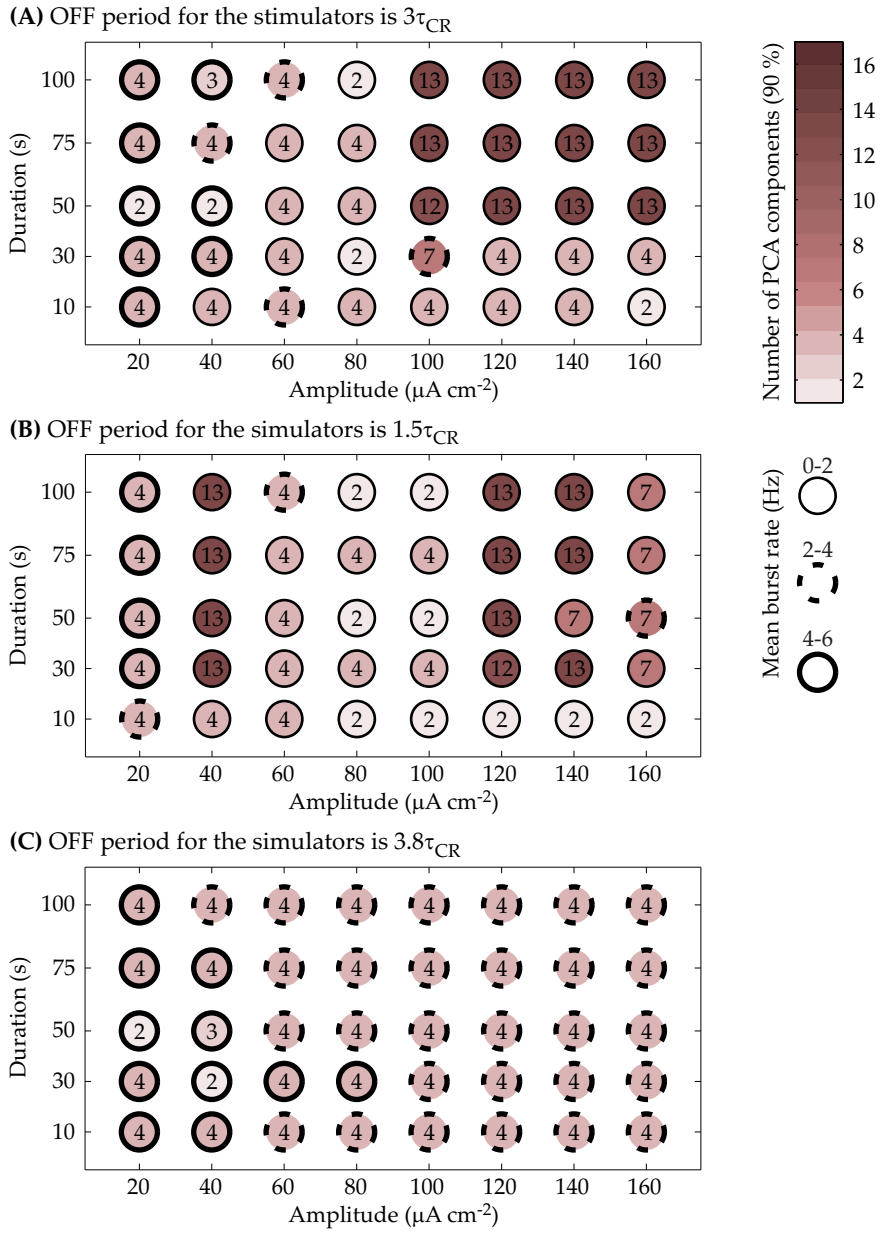

Figure 2.7 Effectiveness of CR-stimulation, measured via the number of PCA components (color coded and explicit indicated in each circle) and mean burst rate (circle outline coded) for STN activity, for three OFF periods over a range of stimulation durations and amplitudes. (**A**) $a_2 = 3$: original CR-protocol; (**B**) $a_2 = 1.5$: ON periods partially overlap; (**C**) $a_2 = 3.8$: contains a stimulus free period after each stimulation cycle. Healthy activity corresponds to regions where at least 10 PCA components are needed and where the mean burst rate is lower than 2. Pulse train (2.10) is applied at 148 Hz with pulse width of 1.7 ms. The markers $+$ and $*$ indicate the stimulation settings used in Figure 2.6B and 2.8, respectively.

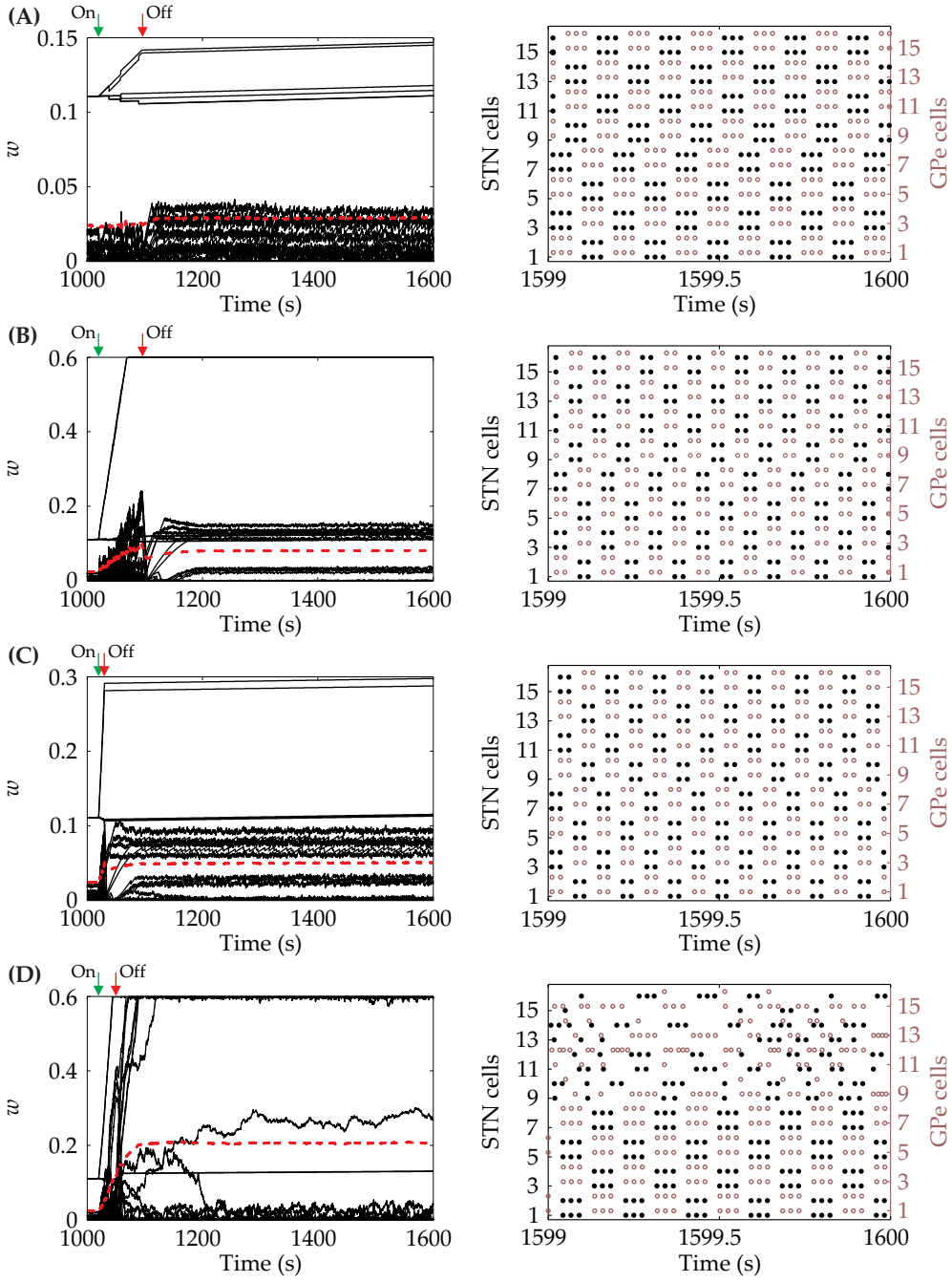

Figure 2.8 Response of the network in PD to different ineffective CR-stimulation amplitudes a_0 (μA cm^{-2}) and durations T_s (s). (**A**) $a_0 = 20$ and $T_s = 75$; (**B**) $a_0 = 60$ and $T_s = 75$; (**C**) $a_0 = 100$ and $T_s = 10$; (**D**) $a_0 = 100$ and $T_s = 30$. For each setting the time courses of the synaptic weights (left, red dashed line corresponds to the mean) and the raster plot of both cell types after stimulation (right) are shown. The other CR-stimulation parameters are as in Figure 2.6B.

2.4 Discussion

In this Chapter we have investigated, with a biophysically plausible model, the role of synaptic plasticity in stabilizing firing patterns in the basal ganglia. In particular, we used an existing network of synaptically-connected, conductance-based model cells from the STN and GPe [69, 181, 211], which we have extended with spike-timing-dependent plasticity (STDP). The original STN–GPe network model displays PD or healthy activity with a structured, sparsely connected network architecture by choosing appropriate parameter values for the coupling strengths and appropriate bias currents to both cell types. The healthy state is characterized by asynchronous activity of both cell types and strong coupling between the GPe cells, whereas the PD state is characterized by synchronized clusters of both cell types and weak coupling between the GPe cells (Figure 2.4). Implementing a STDP rule for the inhibitory connections between the GPe cells, leads to the stabilization of both states (Figure 2.5). Moreover, our results suggest that CR-stimulation may profit from STDP to teach the network to fire in a less pathological manner. The CR-stimulation should be as desynchronous as possible and applied sufficiently long with sufficiently high amplitude to be effective (Figure 2.7). In contrast, STDP has a negative effect when continuous stimulation is employed, in the sense that the network becomes more synchronized after the stimulation (Figure 2.6A).

In order to contribute to the stabilization of the network states, the STDP rule for the inhibitory connections between the GPe cells should have the property that it down- or up-regulates the synaptic weight between GPe cells when they fire in synchrony or in an uncorrelated manner, respectively. The desynchronized dynamics in the healthy state and synchronized dynamics in the PD state is then supported. This can be achieved by choosing a time window for STDP such that the net effect of STDP results in the desired up/down regulation of the synaptic weights. It is not crucial which time window for STDP, e.g. Hebbian or anti-Hebbian and symmetric or asymmetric, is chosen as long as the effective time window is comparable to Figure 2.2. We realize that this is a strong assumption which needs to be verified in an experimental setting.

Guo and Rubin [69] investigated, using a similar STN–GPe network, the effect of CR-stimulation on the relay function of the thalamus. From their simulations they conclude that CR-stimulation can change the firing pattern of STN cells in a way that it restores the thalamus relay fidelity during stimulation. However, they do not have synaptic plasticity in the network model. As a consequence, the network quickly returns to the clustered PD state when stimulation is switched off, thereby disrupting the relay function of the thalamus again. As we already mentioned in the introduction of this chapter, Hauptmann and Tass [82] use a simplified network of only

STN cells, where all cells are coupled to each other via STDP-controlled excitatory synapses, to explore the performance of CR-stimulation in terms of its desynchronizing effect on the synchronized STN bursts. They show that desynchronizing stimuli can lead to down-regulation of the synaptic connection within the STN as a consequence of the STDP rule, which in turn supports the desynchronization of the STN bursts and finally results in a stable healthy state where bursts are uncorrelated. As we already put forward, the all-to-all connections within the STN are highly questionable. We have shown that through indirect, synaptic-mediated stimulation the synaptic connections within the GPe cells can be reshaped as a consequence of the STDP rule, such that desynchronization of the GPe cells occur, which in turn results in desynchronization of the STN cells. We add to the results of Hauptmann and Tass [82] that the redistribution of the synaptic weights within the GPe can be the working mechanism of CR-simulation administered to STN cells.

In Popovych and Tass [171], indirect, synaptic-mediated CR-stimulation was also considered for a network of spiking Hodgkin–Huxley neurons. Each neuron was connected to all other neurons via STDP-controlled inhibitory and excitatory synapses. Instead of explicit modeling and stimulating the target population, they modeled the stimulation-induced activity as post-synaptic potentials to the population of Hodgkin–Huxley neurons. They concluded that both direct electrical and indirect, synaptic-mediated CR-stimulation applied to strongly coupled and synchronized population of spiking neurons can lead to long-lasting redistribution of the synaptic weights and desynchronization. In contrast to this work, we explicit model a target population (STN) for direct electrical CR-stimulation that is reciprocally and synaptically connected to another population (GPe) with intranuclear STDP-controlled synapses.

Experimental studies have linked synchronization in the basal ganglia-thalamocortical circuit that occurs at frequencies within the 3–10 Hz band [44, 120, 197, 207] and beta band (13–30 Hz) [111, 113, 175, 223] with PD. The beta (13–30 Hz) oscillations are probably driven from the motor areas of the cortex, but at tremor frequencies (i.e. 3–10 Hz) it is the opposite direction of connectivity that dominates the synchronized activity [32]. It has been shown that the hyperdirect cortico-subthalamic pathway can be crucial for the expression of abnormal beta oscillations in the STN–GPe network in parkinsonism [131]. Recently, Yamawaki et al. [228] have shown that low frequency stimulation of glutamatergic STN afferents enhances the synaptic efficacy in dopamine-intact brain slice of rat and that high frequency stimulation depresses the synaptic efficacy in dopamine-depleted tissue. They propose that dopamine-depletion leads to increase in weight of cortico-subthalamic synapses, which in turn promotes the transmission of pathological cortical activity to STN. Moreover, their results suggest that the mechanism of the therapeutic effect of STN–

DBS in PD is to depress the cortico-subthalamic synapses. The model of Hahn and McIntyre [72] was able to switch from parkinsonian to healthy activity by reducing the influence of the cortical beta input. In our model we only observe tremor related oscillations, therefore it would be interesting to extend our model with connections from the cortex to STN (hyperdirect pathway) and subject these excitatory connections to STDP.

CHAPTER 3

The pedunculopontine nucleus as an additional target for deep brain stimulation

Abstract The pedunculopontine nucleus (PPN) has been suggested as a target for DBS. In this Chapter we propose a single compartment computational model for a PPN Type I cell and compare its dynamic behavior with experimental data. The model shows bursts after a period of hyperpolarization and spontaneous firing at 8 Hz. Bifurcation analysis of the single PPN cell shows bistability of fast and slow spiking solutions for a range of applied currents. A network model for STN, GPe and GPi produces basal ganglia output that is used as input for the PPN cell. The conductances for projections from the STN and the GPi to the PPN are determined from experimental data. The resulting behavior of the PPN cell is studied under normal and parkinsonian conditions of the basal ganglia network. The effect of high frequency stimulation of the STN is considered as well as the effect of combined high frequency stimulation of the STN and the PPN at various frequencies. The relay properties of the PPN cell demonstrate that the combined high frequency stimulation of STN and low frequency (10 Hz, 25 Hz, 40 Hz) stimulation of PPN hardly improves the effect of exclusive STN stimulation. Moreover, PPN–DBS at low stimulation amplitude has a better effect than at higher stimulation amplitude. The effect of PPN output on the basal ganglia is investigated, in particular the effect of STN–DBS and/or PPN–DBS on the pathological firing pattern of STN and GPe cells. PPN–DBS eliminates the pathological firing pattern of STN and GPe cells, whereas STN–DBS and combined STN–DBS and PPN–DBS eliminate the pathological firing pattern only from STN cells[1].

[1] Adapted from M. A. J. Lourens, H. G. E. Meijer, T. Heida, E. Marani, and S. A. van Gils. The pedunculopontine nucleus as an additional target for deep brain stimulation. *Neural Networks*, 24(6):617630, 2011.

3.1 Introduction

Currently, deep brain stimulation (DBS) for Parkinson's disease (PD) is widely applied in the subthalamic nucleus (STN), the globus pallidus pars interna (GPi) and the ventral intermediate thalamic nucleus. For many patients STN/GPi–DBS is successful for cardinal symptoms, but has only limited effect for axial symptoms, such as gait disturbances and postural instability. Stimulation of these targets mainly affects the thalamocortical output of the basal ganglia to cortical motor areas, whereas the axial muscles involved in locomotion and posture are mainly controlled from the brain stem [154]. These symptoms are particularly resistant to dopaminergic drugs. This suggests the involvement of non-dopaminergic pathways in the pathophysiology of these symptoms [77]. Since the pedunculopontine nucleus (PPN) in the brain stem connects to nuclei in the basal ganglia and the spinal cord and its role in locomotion and postural control [77, 161], this nucleus has been suggested as a target for DBS to improve gait and postural instability [169].

The PPN is a rostral brain stem structure consisting of cholinergic and non-cholinergic neurons belonging to the ascending reticular activating system and the mesencephalic locomotor region [138]. The PPN can be subdivided into two parts based on neuron density and neurochemical characteristics: the pars compacta (PPN_c) and the pars dissipata (PPN_d) [160]. The PPN_c consists mainly of large cholinergic neurons [98]. The PPN_d consists of small and medium sized neurons with approximately the same number of cholinergic and non-cholinergic neurons [77]. Non-cholinergic PPN neurons are mostly glutamatergic, but also noradrenergic, dopaminergic, GABAergic (interneurons) and peptidergic [161].

The main input from the basal ganglia to the PPN are the GABAergic projection from GPi and the substantia nigra pars compacta (SN_c), predominantly to the non-cholinergic neurons of the PPN_d [161]. The glutamatergic neurons of the PPN_d play an important role in the regulation of the basal ganglia and spinal cord [161]. The cholinergic PPN_c is a principal component in a feedback loop from the spinal cord and limbic system back into the basal ganglia and thalamus [161].

Three types (I, II and III) of the PPN neurons have been characterized based on their intrinsic electrical membrane properties as obtained from intracellular recording [105, 202–204]. Type I neurons are characterized by low threshold calcium spikes (LTS), which give rise to a burst of fast action potentials after the offset of a hyperpolarizing current. The neurons also fire bursts of spikes when a depolarized stimulus is given during hyperpolarization. Type I neurons are non-cholinergic [105] and probably glutamatergic [203]. Type II neurons do not burst, but instead they fire single action potentials with a large afterhyperpolarization in response to a depo-

larizing injected current. About 50% of type II neurons are cholinergic. Type III has neither the characteristics of both Type I and Type II.

In contrast to the high frequency stimulation of STN/GPi, stimulation of PPN should be applied with low frequency (20–25 Hz) to improve gait disturbances and postural instability [134, 169]. For these symptoms low frequency stimulation of the PPN combined with standard DBS of the STN seems to be clinically more effective [60, 196]. So the question arises why PPN should be stimulated at low frequencies. Despite real therapeutic successes, the fundamental physiological mechanisms underlying the effect of DBS are still not understood.

Pathophysiology of PD is characterized by increased firing rates of cells in the basal ganglia, a tendency towards bursting and abnormal synchronization in the cells of STN and GP [32]. In particular, the synchronization at low frequencies (<30) are thought to be related to motor impairment in PD [32]. A hypothesis is that high frequency stimulation of basal ganglia nuclei masks the pathological synchronized firing patterns of the basal ganglia with a regularized firing pattern. In the usual targets for high frequency stimulation in the basal ganglia, the neurons fire spontaneously at frequencies around 50 Hz and can easily follow the high frequencies of the stimulation. By following the high frequencies of the stimulation, the basal ganglia neurons are driving in a tonic mode, that prevents them relapsing into the pathological synchronized firing pattern. On the other hand, PPN neurons fire spontaneously at lower frequencies around 10 Hz and high frequency stimulation would probably silence rather than drive them. Androulidakis et al. [7, 8] shows that when akinesia is successfully alleviated in PD by L-Dopa, this is associated with the return of a 10 Hz component in the correlation between the PPN and the sensorimotor cortex. It seems that low frequency stimulation will assist PPN to return to its natural 10 Hz oscillations, which in turn facilitates locomotion and postural control.

The aim of this Chapter is to investigate, with a computational model, how the PPN responds to physiological and pathological inputs of the basal ganglia. Moreover, we will investigate the effects of DBS in STN and PPN on the behavior of the network. To achieve this aim we first develop a computational conductance-based model for PPN, as such model is not yet available. We model PPN Type I neurons, because projections from the basal ganglia are primarily to the glutamatergic PPN neurons (Type I) and these neurons provide the prominent descending PPN output to the spinal cord. Second, we generate basal ganglia input to the PPN Type I model using the basal ganglia model as proposed by Rubin and Terman [181]. The model of Rubin and Terman [181] has well defined physiological and pathological (parkinsonian) states. To investigate the effect of STN–DBS and/or PPN–DBS we look at relay capability of the PPN cell to relay excitatory cortical input. Finally we make projec-

tions from the PPN back to the basal ganglia to investigate the effect of STN–DBS and/or PPN–DBS on the pathological firing pattern of STN and GPe cells.

3.2 Methods

3.2.1 PPN model

We have modeled the PPN Type I neuron as a single compartment model. Based on the work of Takakusaki and Kitai [202] we include in our model a persistent sodium current ($I_{\mathrm{Na,p}}$) and T-type calcium current (I_{T}). The persistent sodium current is responsible for subthreshold membrane oscillations in PPN Type I neurons, which underlies spontaneous repetitive firing. T-type calcium current is responsible for bursts of low threshold spikes. To produce action potentials in response to depolarizing current the model includes a sodium current (I_{Na}) and potassium current (I_{K}). The resting potential is defined by sodium ($I_{\mathrm{Na,L}}$) and potassium ($I_{\mathrm{K,L}}$) leak currents. In addition the model contains a hyperpolarization-activated current (I_{hyp}) to recover faster from hyperpolarization and facilitate the burst. The time-derivative of the membrane potential ($V_{\mathrm{m,PPN}}$) of the PPN type I neuron is given by:

$$C\frac{\mathrm{d}V_{\mathrm{m,PPN}}}{\mathrm{d}t} = -I_{\mathrm{Na,L}} - I_{\mathrm{K,L}} - I_{\mathrm{Na}} - I_{\mathrm{K}} - I_{\mathrm{T}} - I_{\mathrm{hyp}} - I_{\mathrm{Na,p}} + I_{\mathrm{app}}, \tag{3.1}$$

where C is the membrane capacitance, I_{app} is the applied current. The ionic currents are conductance-based and described according to the Hodgkin–Huxley formalism, except for the T-type calcium current which includes the Goldman–Hodgkin–Katz ion current equation (Appendix B). The exact voltage dependence and kinetics of PPN ionic currents are based on similar neurons, namely the thalamocortical relay neuron [48, 88, 135] and the pre-Bötzinger neuron [182, 183], as there are no reports in literature of such data for the PPN.

3.2.2 The Network model

In order to investigate the effect of the basal ganglia input to the PPN cell, we have generated such input using the basal ganglia model as proposed by Rubin and Terman [181]. They modeled the indirect pathway of the basal ganglia that includes a population of STN, GPe, GPi and thalamic relay cells. In their model each STN, GPe and GPi cell is represented as a single compartment conductance-based model. Our

network consist of 8 STN cells, 8 GPe cells, 8 GPi cells and 1 PPN cell and excludes the thalamic relay cells.

For the synaptic connections between the STN and GPe cells we use the structured sparsely connected architecture (Figure 3.1), as in Terman et al. [211]. This network can reproduce both correlated rhythmic activity (clustered) and uncorrelated spiking. Each STN cell receives inhibitory input from two GPe cells. Each GPe cell receives excitatory input from one STN cell and inhibitory input from two immediate GPe neighbors. Each GPe cell also receives a constant current input representing striatal input. Each GPi cell receives excitatory input from one STN cell and inhibitory input from one GPe cell [181]. Finally, four STN cells and four GPi cells project excitatory (glutamatergic) respectively inhibitory (GABAergic) to the PPN cell, see Figure 3.1. As in Rubin and Terman [181] the synaptic current to the PPN is modeled as:

$$I_{\alpha\to\mathrm{PPN}} = g_{\alpha\to\mathrm{PPN}}(V_{\mathrm{m,PPN}} - E_{\alpha\to\mathrm{PPN}})\sum_{j\in J} s_\alpha^j, \tag{3.2}$$

where $I_{\alpha\to\mathrm{PPN}}$ is the synaptic current from structure α to the PPN cell, α is STN or GPi, $g_{\alpha\to\mathrm{PPN}}$ is the maximal synaptic conductance and $E_{\alpha\to\mathrm{PPN}}$ the reversal potential. For STN we take $g_{\mathrm{STN}\to\mathrm{PPN}} = 0.15$ mS cm^{-2} and $E_{\mathrm{STN}\to\mathrm{PPN}} = 0$ mV, and for GPi we take $g_{\mathrm{GPi}\to\mathrm{PPN}} = 0.1$ mS cm^{-2} and $E_{\mathrm{GPi}\to\mathrm{PPN}} = -95$ mV. The summation is taken over the subgroup of STN/GPi cells (J) that project to the PPN cell. Each synaptic variable s_α^j satisfies a first-order differential equation of the form:

$$\frac{\mathrm{d}s_\alpha^j}{\mathrm{d}t} = \mathrm{A}_\alpha(1 - s_\alpha^j)S_\infty(V_{\mathrm{m},\alpha}^j) - \mathrm{B}_\alpha s_\alpha^j, \tag{3.3}$$

where $S_\infty(x) = 1/(1+\exp(-(x-\theta_\alpha)/\sigma_\alpha))$. The kinetic parameters for STN and GPi are $[\mathrm{A}_\alpha, \mathrm{B}_\alpha, \theta_\alpha, \sigma_\alpha] = (5, 1, -9, 8)$, $(2, 0.1, -37, 2)$, respectively.

3.2.3 *Normal and parkinsonian states of the basal ganglia*

Depending on the architecture and strengths of synaptic connections between the STN and GPe, within the GPe, and the striatal input to the STN–GPe network the model shows correlated rhythmic activity, uncorrelated spiking and propagating waves. It has been found in experiments that during PD there is an increased synchrony between nuclei in the basal ganglia while neurons fire in a bursty mode. As demonstrated in Terman et al. [211], STN and GPe cells connected through a

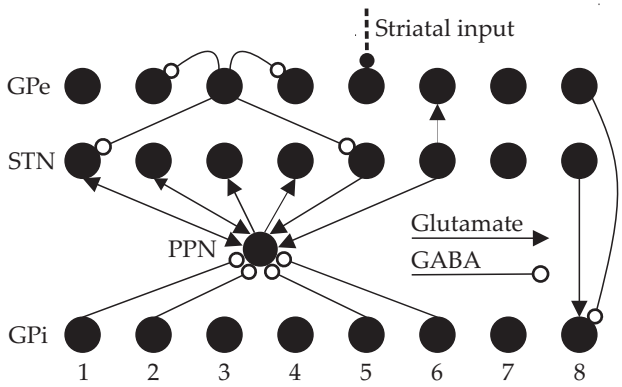

Figure 3.1 The network architecture. For the STN–GPe connection the structured sparsely architecture from Terman et al. [211] is adopted. GPe cell i inhibits its two immediate GPe neighbors ($i+1$ and $i-1$) as well as two STN cells ($i-2$ and $i+2$) by skipping the three STN cells located nearest to it. Here i runs from 1 to 8. In addition, GPe cells uniformly receive constant current inhibition from striatum. Each STN cell sends excitation to its nearest GPe cell (same index). Each GPi cell receives inhibition from the nearest GPe cell and excitation from the nearest STN cell. The PPN cell receives inhibition from GPi cell 1,2,5 and 6 and excitation from STN cell 1,2,5 and 6. In our PD simulations the STN cells 1, 2, 5 and 6 are active as a cluster. In our network of section 3.2.6 the PPN cell sends also excitation to STN cell 1, 2, 3 and 4. The network architecture has a periodic structure. Lines ending with arrows and open circles indicate excitatory glutamatergic and inhibitory GABAergic synaptic connections, respectively.

structured sparse architecture can fire irregularly with weak correlation between the cells as well as in clusters with high correlation between the cells. By using a structured sparse architecture we mimic a basal ganglia input to the PPN cell that represents a normal (uncorrelated spiking) or PD (correlated rhythmic activity) situation, see top and middle panels of Figure 3.2. Following the approach of Pirini et al. [168], Rubin and Terman [181], only two parameters are used to switch between the normal and the PD state: the indirect striatal current to GPe cells ($I_{\text{striatum}\to\text{GPe}}$) and the intra-GPe inhibitory synaptic conductance ($g_{\text{GPe}\to\text{GPe}}$). In the normal state we use $I_{\text{striatum}\to\text{GPe}} = 1.1\ \mu\text{A cm}^{-2}$ and $g_{\text{GPe}\to\text{GPe}} = 1\ \text{mS cm}^{-2}$. In the PD state $I_{\text{striatum}\to\text{GPe}} = -3.5\ \mu\text{A cm}^{-2}$ and $g_{\text{GPe}\to\text{GPe}} = 0.05\ \text{mS cm}^{-2}$. The increase in inhibitory striatal input to the GPe in PD is motivated by the fact that the activation of the D2-receptors in the striatum in PD is decreased, due to dopamine depletion in PD. This decreased activation leads to less inhibition of the striatal input to the GPe. Rubin and Terman [181] motivated the decrease of the intra-GPe inhibitory synaptic conductance in PD on experimental results in rats [158, 195].

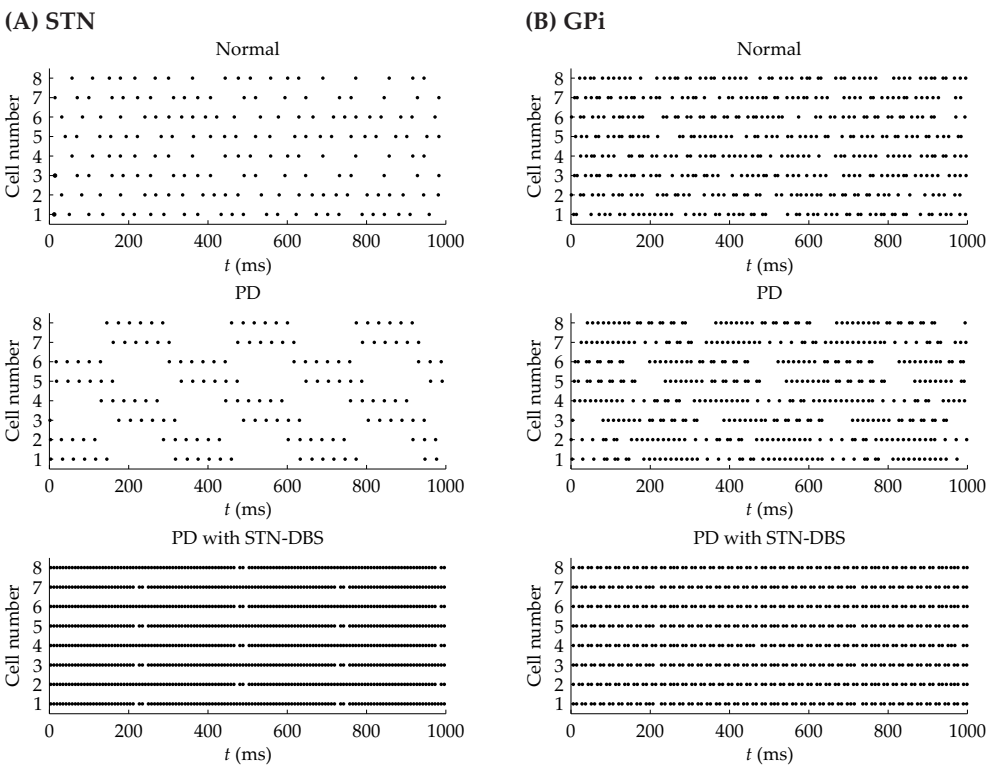

Figure 3.2 Raster plots of the spike times for all eight STN cells (**A**) and all eight GPi cells (**B**) in the normal (top), PD (middle) and PD with STN–DBS (bottom) state. In the normal state the firing patterns of both types of cells are irregular and uncorrelated. In the PD state STN cells fire in a bursty and clustered pattern around 3 Hz and the cells within each cluster are almost synchronized (small lag). The GPi cells fire in a similar manner, but are less bursty. In the PD state with STN–DBS the STN cells are locked to the DBS frequency and GPi cells are partially locked by half the DBS frequency.

3.2.4 Deep brain stimulation

In our network model we apply DBS to STN and PPN. As in Rubin and Terman [181] the effect of DBS on its target cells is modeled as a train of positive current pulses, injected directly into the target cells:

$$I_{\mathrm{DBS}} = i_{\mathrm{D}} H_\infty(\sin(2\pi f_{\mathrm{DBS}} t))(1 - H_\infty(\sin(2\pi f_{\mathrm{DBS}}(t + \delta_{\mathrm{DBS}})))), \tag{3.4}$$

where $H_\infty(x) = 1/(1 + \exp(-1000x))$ is a smooth approximation of the Heaviside step function, i_{D} is the amplitude of the injected current, f_{DBS} is the frequency of the DBS pulse train and δ_{DBS} is the duration of each impulse.

In the case of STN–DBS we assume that each STN cell receives the same DBS signal. STN–DBS is only applied in the PD state, with $i_D = 400$ µA cm^{-2}, $f_{DBS} = 130$ Hz and $\delta_{DBS} = 0.15$ ms. Pirini et al. [168] have demonstrated that these values for STN–DBS ensure a 1:1 ratio between DBS pulses and the action potentials of the STN cells (Figure 3.2A, bottom).

Our PPN cell receives DBS in the PD state of the network as well in the PD with STN–DBS state, as the combined stimulation seems to be clinically more effective [60, 196]. The settings for PPN–DBS are $\delta_{DBS} = 0.15$ ms, $f_{DBS} = 10$–25–40 Hz and $i_D = 10$–100 µA cm^{-2}. We use these frequencies as it was claimed that 25 Hz was optimal [134, 169].

3.2.5 Cortical input

In addition to input from the basal ganglia the PPN Type I cell also receives excitatory cortical input [98]. To investigate the functionality of the PPN cell under normal, parkinsonian, parkinsonian with STN–DBS and/or PPN–DBS conditions, we test the relay capability of the PPN cell with excitatory, conductance-based, synaptic current $I_{Cort.}$:

$$I_{Cort.} = g_{Cort.} s (V_{m,PPN} - E_{Glut.}), \tag{3.5}$$

where s is the synaptic variable of the presynaptic cortex cell. The maximal conductance ($g_{Cort.}$) and the reversal potential ($E_{Glut.}$) are set to 0.15 mS cm^{-2} and 0 mV, respectively. At each spike of the cortex cell the synaptic variable is reset to 1, after which it decays exponentially with time constant $B_{Cort.}$:

$$\frac{ds}{dt} = -B_{Cort.} s. \tag{3.6}$$

$B_{Cort.}$ is set to 1 ms^{-1}. The spikes for the cortical input are selected from a Poisson distribution, with an enforced pause of 10 ms between spikes to avoid excessive firing. We use cortical Poisson inputs with mean rates of 12, 25 and 45 Hz.

3.2.6 PPN output to basal ganglia

The two key functions of the PPN is to relay and to regulate the basal ganglia activity [138]. In particular, the function of the PPN Type I cell can be seen as regulator of

the basal ganglia [161]. These functions imply that the PPN and the basal ganglia are highly interconnected. To investigate the regulation function of the PPN Type I under normal, parkinsonian, parkinsonian with STN–DBS and/or PPN–DBS conditions, we have also extended our model with PPN connections back to the basal ganglia. The major projections from the PPN to the basal ganglia are the projections to the STN and SN_c [98]. The PPN projections to STN are distributed uniformly throughout the STN [98] and are cholinergic, glutamatergic and GABAergic [138]. We choose for a total of four glutamatergic projections by our PPN Type I cell; two to adjacent STN cells, that connect to PPN, forming reciprocal connections, and two to adjacent STN cells, which are not connected to PPN (Figure 3.1).

The synaptic current from PPN to STN cell j ($I_{\mathrm{PPN}\to\mathrm{STN},j}$) is modeled as:

$$I_{\mathrm{PPN}\to\mathrm{STN},j} = g_{\mathrm{PPN}\to\mathrm{STN}}(V_{\mathrm{m,STN},j} - E_{\mathrm{PPN}\to\mathrm{STN}})s_{\mathrm{PPN}}, \tag{3.7}$$

where s_{PPN} is the synaptic variable of the PPN cell and $V_{\mathrm{m,STN},j}$ the membrane potential of STN cell j. The maximal synaptic conductance($g_{\mathrm{PPN}\to\mathrm{STN}}$) and the reversal potential $E_{\mathrm{PPN}\to\mathrm{STN}}$ are set to 0.15 mS cm^{-2} and 0 mV, respectively. The dynamics of the synaptic variable of the PPN cell is modeled with Equation 3.3 and use the same kinetic parameters as we used for the STN cell, namely $[A_\alpha, B_\alpha, \theta_\alpha, \sigma_\alpha] = (5, 1, -9, 8)$

We use the same parameters setting that we employed for the network without feedback to switch between a normal and PD behavior.

3.2.7 Simulation

The PPN Type I model and the network model are implemented in MATLAB (Mathworks, Inc., Natick, MA, USA). To simulate the firing properties of the isolated PPN cell we use a stiff integrator (ODE15s in MATLAB) with maximum step size 0.1 ms and relative tolerance 10^{-6}. We exclude effects of initial transients by ignoring the first 400 millisecond of PPN cell simulations. The bifurcation analysis of the PPN cell is done within MATCONT, a bifurcation analysis tool [50]. For the network model without projections from PPN to STN the same numerical method is used except for the relative tolerance, which is now set to 10^{-4} for the integration of the STN–GPe–GPi network. For the simulation of the STN–GPe–GPi network we ignore the first 6 seconds before we use it as input to the PPN cell. For the simulations with PPN projections to the STN we used the fourth-order Adams Predictor-Corrector method with fixed step size of 0.01 ms to integrate the STN–GPe–GPi–PPN network. To speed up the calculation we have made a minor modification to the PPN model. The voltage depending time constants for the (in)activations gating variables of the

persistent sodium channels are bounded from below by 0.01 ms. This modification does not effect the response of the PPN cell to depolarizing and hyperpolarizing stimuli. For these simulations we ignore the first 2 seconds.

Spectral analysis is done with MATLAB using Neurospec and is based on Halliday et al. [74] (http://www.neurospec.org). Autospectra of the PPN spike times are calculated by dividing 10 second simulation data in 6 equal-length segments, providing a resolution of 0.6 Hz, and by averaging their Fourier transform. For additional smoothing of the autospectra we use a Hanning filter. The spike times are obtained from the voltage trace by a thresholding method (threshold is -20 mV).

To quantify the reliability and accuracy with which the PPN cell responds to the excitatory cortical inputs (Equation 3.5) we use the relay index (RI): The ratio of successfully relayed input and the total number of excitatory inputs. Specifically, for each excitatory cortical input, we record a successfully relayed input if at least one PPN spike occurs within a window of 5 ms after the input arrives. Thus a RI of zero means no relay at all of the Poisson input, whereas a RI of one means a perfect relay. Each RI is averaged over 10 trials of 10 second simulation. The cortical Poisson input in each trial is different, but has the same mean rate.

3.3 Results

3.3.1 Firing properties of the isolated PPN neuron

The cell fires spontaneously at approximately 8 Hz (Figure 3.3). The cell responds with high frequency spiking when a small depolarizing stimulus is given (Figure 3.3). When the PPN cell is hyperpolarized, a burst appears at the end of the stimulus period or when a depolarizing stimulus is given during hyperpolarization (Figure 3.3).

3.3.2 Bifurcation analysis of the isolated PPN neuron

Figure 3.4 shows the bifurcation diagram of the PPN model with the applied current (I_{app}) as parameter. As the applied current increases the stable equilibrium (rest state) becomes unstable via a subcritical Hopf bifurcation (H_1), with unstable limit cycles bifurcating. The equilibrium is unstable until the second Hopf bifurcation (H_2). This Hopf bifurcation is supercritical, which means that stable limit cycles emerge. A stable limit cycle corresponds to continuous spiking.

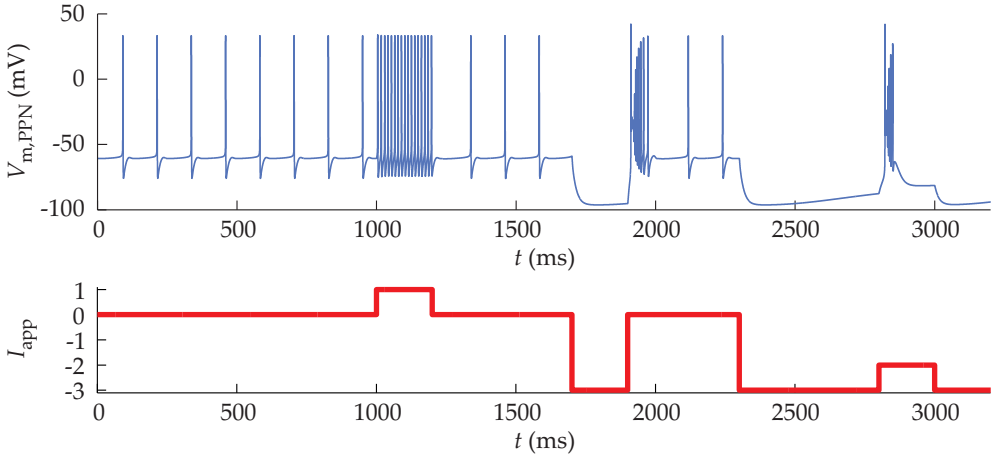

Figure 3.3 Properties of the PPN model Type I: first second spontaneous firing at approximately 8 Hz; After the first second response to a depolarizing stimulus; last 1.5 second response to a hyperpolarizing stimulus and depolarizing stimulus during hyperpolarization. Below the voltage trace the applied stimulus is shown (I_{app} (μA cm^{-2})).

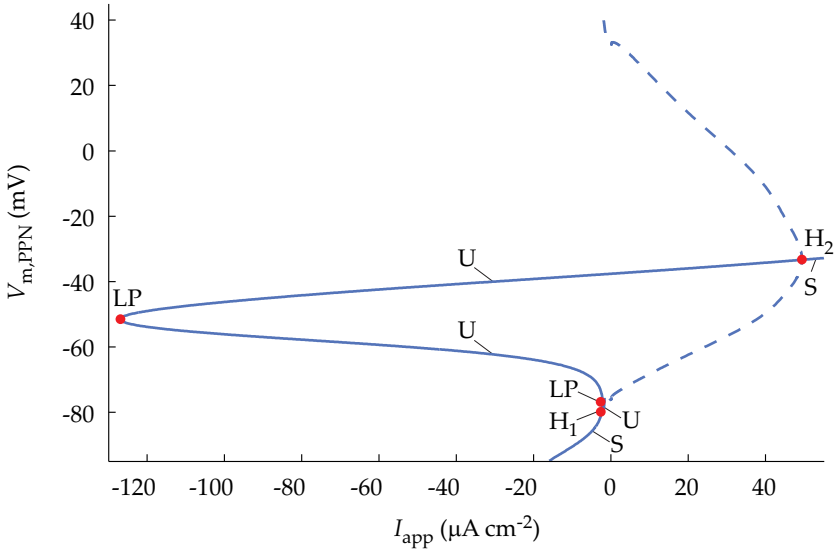

Figure 3.4 Bifurcation analysis of the PPN model with I_{app} as free parameter. Solid curve shows the equilibrium value of the membrane potential ($V_{m,PPN}$). Labels S and U denote stable and unstable branches respectively. H_1 is a subcritical Hopf bifurcation, H_2 is a supercritical Hopf bifurcation and LP is a limit point bifurcation. Dashed curve shows the min/max value of the stable limit cycle.

Continuation of the limit cycle starting from H_2 shows a decrease in frequency as the applied current decreases. The limit cycle becomes unstable via a limit point bifurcation of limit cycles (Figure 3.5, LPC_1). Continuing the limit cycle further it regains stability through a period doubling bifurcation (Figure 3.5). The period then is nearly constant around 100 ms. This low frequency spiking limit cycle corresponds to the spontaneous firing of the PPN.

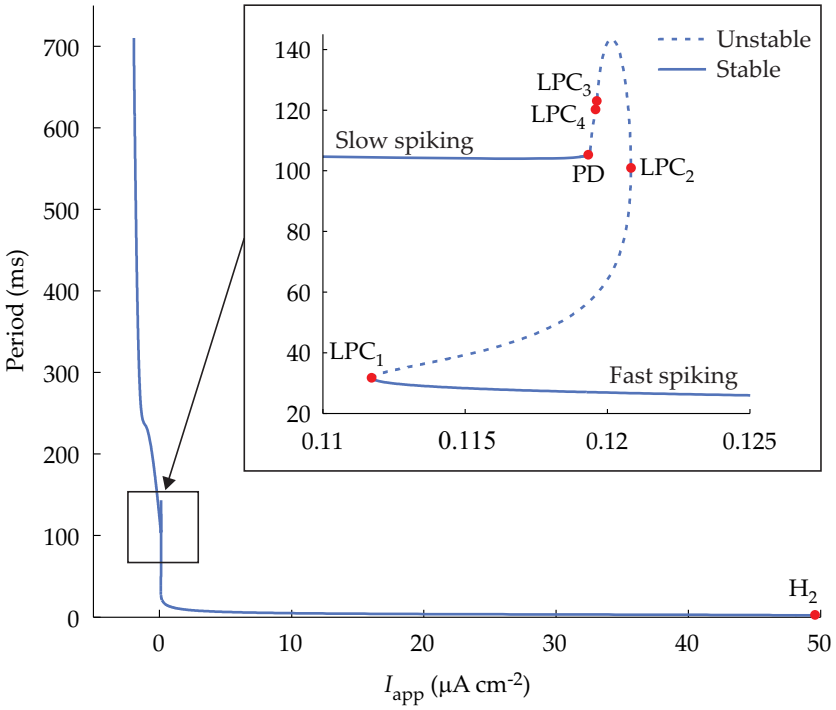

Figure 3.5 Partial information about dynamical behavior: period of the spiking solutions as function of I_{app}. LPC is a limit point bifurcation of limit cycles and PD is a period doubling bifurcation.

Both tonic spiking regimes have a type II phase response curve (Figure 3.6), meaning that a perturbation of the limit cycle can produce a phase advance or phase delay depending on the timing. The phase shift of both the low and high frequency spiking solution becomes larger upon increasing, respectively decreasing, I_{app} towards the bifurcation points where they lose stability.

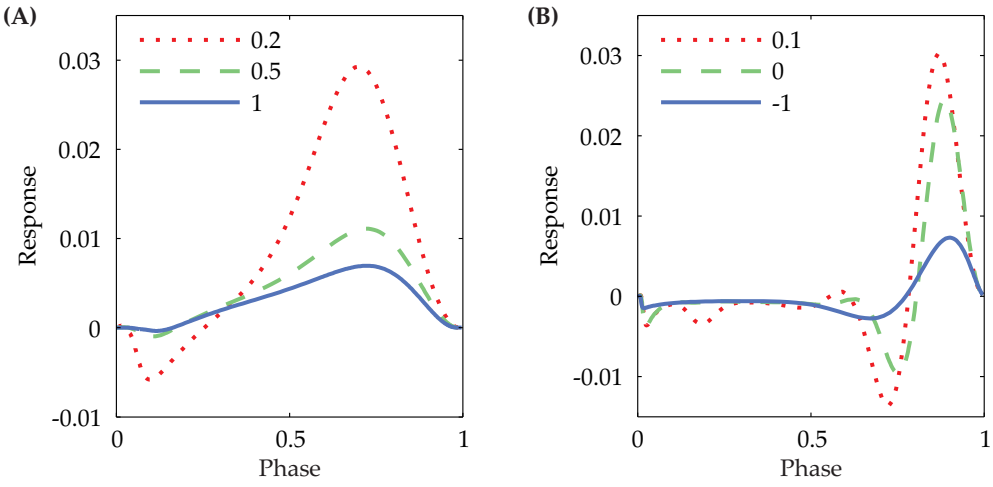

Figure 3.6 PRCs of limit cycles in the PPN model, at different parameter values I_{app} (μA cm^{-2}): (**A**) high frequency spiking; (**B**) low frequency spiking

3.3.3 PPN with basal ganglia input

Normal

Figure 3.7 shows the mean frequency of the PPN cell with normal input for different choices for the strength of the synaptic conductances from STN and GPi to PPN. The mean frequency is calculated from the reciprocal of the mean interspike interval over a period of 10 seconds. This figure was almost equal to the average number of spikes per second indicating that the response was not very bursty. We simulate a STN lesion in our model by setting the STN conductance to zero and adjust the GPi conductance to get a firing rate according to experiments of Breit et al. [31] (2.9–6.6 Hz). Having the GPi conductance we then adjust the STN conductance to obtain a firing rate of the PPN cell under normal conditions. Experiments in anesthetized rat [185], and in monkeys [133] show that the majority of the PPN cells with a narrow spike width have a irregular firing pattern and a discharge rate of 10–20 Hz during spontaneous activity. It is proposed that the narrow spike width PPN cells are non-cholinergic and probably correspond to Type I cells [202]. This procedure yields a 10 Hz irregular firing rate for the normal input when we set $g_{\mathrm{GPi}\to\mathrm{PPN}} = 0.1$ mS cm^{-2} and $g_{\mathrm{STN}\to\mathrm{PPN}} = 0.15$ mS cm^{-2}, see Figure 3.7. We will not change these settings between the normal and PD states.

The top panel of Figure 3.8A shows the total synaptic input from STN and GPi to the PPN cell during the normal state. In the normal state, the STN and GPi cells fire irregularly and uncorrelated (Figure 3.2) leading to an irregular total synaptic

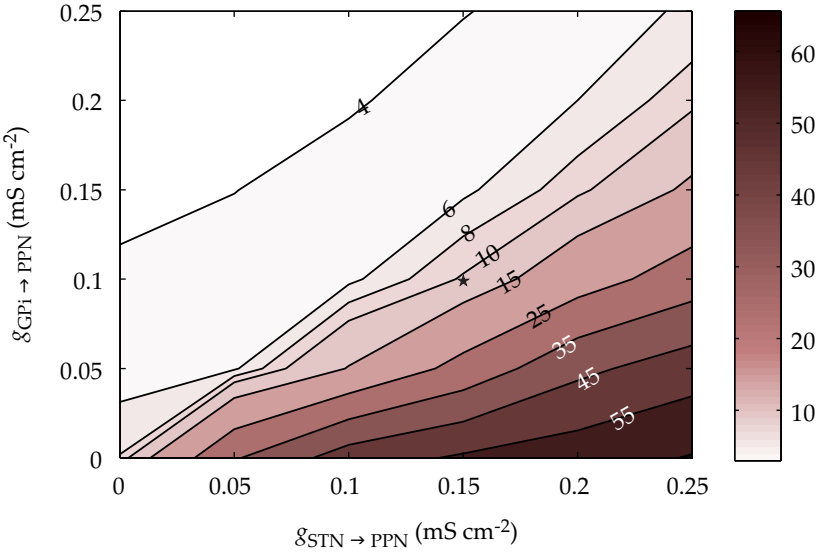

Figure 3.7 Contour plot of the mean frequency of the PPN in the normal state for different choices for $g_{GPi \to PPN}$ and $g_{STN \to PPN}$. See text for details about calculation of the mean frequency. The marker $\star$ indicates the values for the chosen parameters.

input of the four STN and GPi cells projecting to PPN. The PPN cell fires with a mean frequency of 10.3 Hz which is slightly faster than its spontaneous behavior (Figure 3.8A, middle). In the autospectrum there is no clear peak above the confidence level (Figure 3.8A, bottom). We conclude that the PPN cell fires in an irregular manner in response to irregular (Normal) input.

PD

The STN cells fire in a bursty and clustered pattern in the PD state (Figure 3.2A). One cluster projects to the PPN cell resulting in excitation from STN in this bursting pattern around 3 Hz. The GPi cells behave similarly but fire less bursty (Figure 3.2B) resulting in flatter level of inhibition, see top panel of Figure 3.8B. The inhibitory input of GPi is relatively high compared to the excitatory input of STN, preventing the PPN from firing. At the onset of the STN clustered input the excitation to PPN becomes sufficiently high to overcome the inhibition of GPi, allowing the PPN to fire. In response to this increased excitation of the STN the inhibitory input of GPi increases, preventing the PPN cell to fire with the burst frequency of the STN input. The PPN cell responds with subthreshold oscillations during the STN clustered input. This regular input of STN and GPi resulting in a regular firing pattern of the PPN cell with a mean frequency of 3.19 Hz (Figure 3.8B, middle). This regularity is

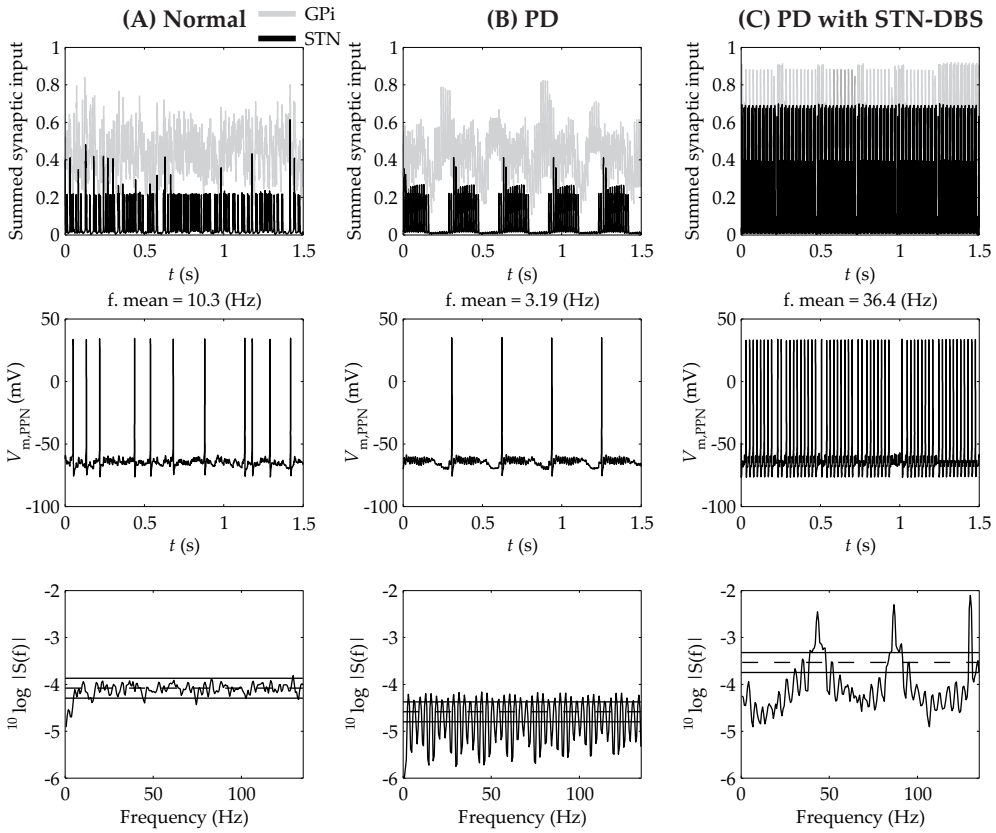

Figure 3.8 Response of the PPN cell to inputs from the STN and GPi under normal (**A**), PD (**B**) and PD with STN–DBS (**C**) conditions. Top: total synaptic input from GPi and STN received by the PPN cell under the different conditions. The synaptic input of GPi is defined as the normalized sum of the synaptic variables over the four GPi cells projecting to the PPN cell. Same definition holds for the STN input. Middle: voltage trace of the PPN cell. Bottom: autospectrum of the PPN spike times; see Section 3.2.7 for computational details.

also reflected in the autospectrum of the PPN output. Clear peaks occur at the mean frequency and its superharmonics 6.4 Hz , 9.6 Hz , 12.8 Hz, etc. (Figure 3.8B, bottom).

PD with STN–DBS

Applying STN–DBS in the PD state, the bursting element in the STN input disappears and the STN input becomes tonic (130 Hz, DBS frequency)(Figure 3.8C, top). Also the GPi inhibition becomes more tonic. As a result the level of excitation to PPN is higher and the mean firing rate increases to 36.4 Hz (Figure 3.8C, middle). The autospectrum has a clear peak at the STN–DBS frequency and its subharmonics

86.7 and 43.3 Hz, but no clear peak at the PPN mean frequency(Figure 3.8C, bottom). Thus, STN–DBS makes the regular firing pattern of the PPN cell in PD more irregular, and introduces components of its frequency in the PPN output.

3.3.4 Effect of PPN–DBS

Figure 3.9 shows the response of the PPN cell to PPN–DBS with amplitude of 100 μA cm^{-2} and frequencies of 10, 25 and 40 Hz. In the PD state and without STN stimulation, the PPN cell is locked to its own stimulation frequency. This can be seen from the peaks in the autospectra at the PPN–DBS frequency and its subharmonics (Figure 3.9A). At the higher frequencies (25 and 40 Hz) this locking is perfect, meaning the PPN cell fires with its own stimulation frequency. When STN–DBS is applied in the PD state and the PPN cell is stimulated, the locking of the PPN cell to its own stimulation frequency is less prominent, as seen in Figure 3.9B. STN–DBS disturbs the total synchronization between the PPN cell and its own stimulation. This effect of STN–DBS is less if the PPN–DBS frequency increases. This can be seen from the peaks at the STN–DBS frequency and its subharmonics in the autospectra of 10 and 25 Hz PPN stimulation, whereas the autospectrum of 40 Hz PPN stimulation has no clear peaks at the STN–DBS frequency.

Figure 3.10 shows again the effect of PPN–DBS, but now with a lower stimulation amplitude of 10 μA cm^{-2}. In both network states (PD and PD with STN–DBS) and for all stimulation frequencies, the PPN–DBS is too weak to lock the PPN firing to the stimulus frequency. The regular 3 Hz firing of the PPN cell in the PD state disappears as the PPN–DBS frequency increases and becomes more irregular (peaks at 3 Hz and superharmonics disappear). The effect of STN–DBS is compared to the weak PPN–DBS strong and dominates the firing behavior of the PPN cell.

3.3.5 Relay function of the PPN cell

Table 3.1 shows the relay index (RI) of the PPN cell for the different situations and for three mean rates of the Poisson trains. The RI in the normal state for the three different forms of input is almost the same as in the PD state: except for the Poisson trains with mean rate 45 Hz the normal state is slightly better than the PD state. Compared to the normal and the PD state, STN–DBS improves the relay function of the PPN cell for the Poisson trains with mean rates 25 and 45 Hz. The relay functionality during high frequency STN–DBS is almost never higher with additional PPN–DBS. When PPN–DBS is applied, a lower amplitude (10 μA cm^{-2}) and higher frequency (40 Hz)

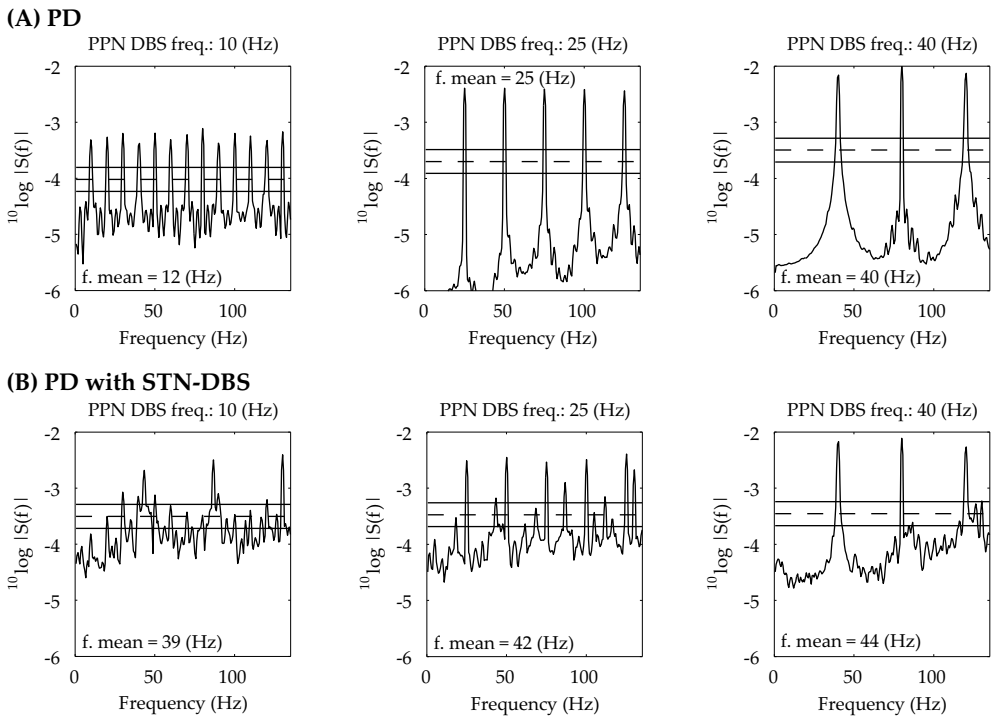

Figure 3.9 Autospectrum of the PPN spike times with PPN–DBS applied. The PPN–DBS settings are $\delta_{\mathrm{DBS}} = 0.15$ ms, $f_{\mathrm{DBS}} = 10 - 25 - 40$ Hz and $i_{\mathrm{D}} = 100$ µA cm^{-2}. f. mean is the mean firing frequency of the PPN cell

shows better results than a higher amplitude (100 µA cm^{-2}) and lower frequencies (10 and 25 Hz).

3.3.6 The closed loop network

Normal, PD and PD with STN–DBS

In section 3.3.3 we considered the output of the PPN receiving input of the basal ganglia in three different states. In this section we consider again the three different states of the basal ganglia, but now we include feedback of the PPN Type I cell to the STN cells as described in section 3.2.6, to form the closed loop network.

Similarly as for the network without connections from the PPN to STN we examine how the mean frequency of the PPN cell with normal input changes as function of the synaptic conductances $g_{\mathrm{GPi}\to\mathrm{PPN}}$ and $g_{\mathrm{STN}\to\mathrm{PPN}}$, see Figure 3.11. The result closely resembles the result of the network without feedback of PPN to STN (Fig-

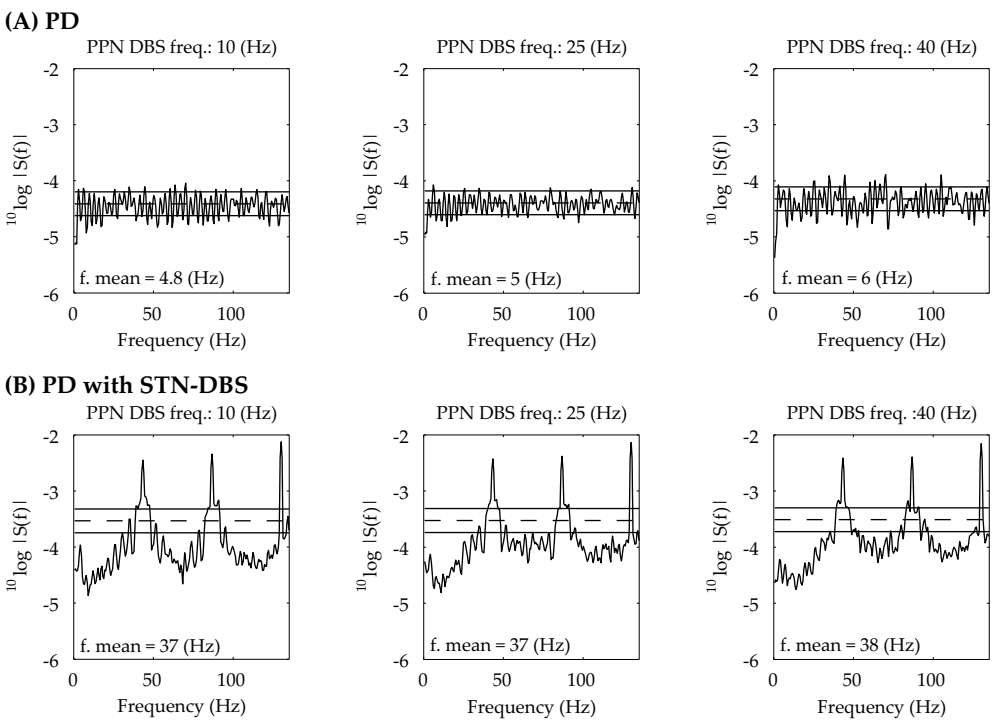

Figure 3.10 Autospectrum of the PPN spike times with PPN–DBS applied. The PPN–DBS settings are $\delta_{\text{DBS}} = 0.15$ ms, $f_{\text{DBS}} = 10 - 25 - 40$ Hz and $i_{\text{D}} = 10$ µA cm^{-2}. f. mean is the mean firing frequency of the PPN cell

ure 3.7). We conclude that the feedback of PPN to STN has a minor effect on the mean frequency of the PPN under normal input conditions. For the other simulations we use $g_{\text{GPi}\to\text{PPN}} = 0.1$ mS cm^{-2} and $g_{\text{STN}\to\text{PPN}} = 0.15$ mS cm^{-2}.

The top panel of Figure 3.12 shows the total synaptic input from STN and GPi to the PPN cell in the three different basal ganglia states. The total synaptic input in all three states is very similar to the case when there is no feedback of PPN to STN. We observe that the firing pattern of the basal ganglia cells in the normal and PD state is not altered by our adding projections from the PPN to STN. Moreover, the PPN cell responds to these synaptic inputs in a similar manner as without the PPN to STN connections (Figure 3.12, middle and bottom). The PPN cell fires irregular in the normal state with a mean frequency of 8.7 Hz. In the PD state, the firing pattern is regular and the mean frequency is decreased to 3.39 Hz. STN–DBS makes the regular firing pattern of the PPN cell in PD more irregular, and introduces components of its frequency in the PPN output.

Table 3.1 The Relay index (RI) of the PPN cell for the different situation in response to a cortical Poisson input to the PPN cell with mean frequency of 12, 25 and 45 Hz and conductance of 0.15 mS cm^{-2}. For STN–DBS the DBS settings are $i_{D,STN} = 400$ µA cm^{-2}, $f_{DBS,STN} = 130$ Hz and $\delta_{DBS,STN} = 0.15$ ms and for PPN–DBS the pulse width is $\delta_{DBS,PPN} = 0.15$ ms.

State	Mean frequency of the cortical Poisson input					
	12 Hz		25 Hz		45 Hz	
Normal	0.75		0.71		0.65	
PD	0.75		0.71		0.64	
PD with STN–DBS	0.70		0.74		0.76	
	$i_{D,PPN} = 100$	$i_{D,PPN} = 10$	$i_{D,PPN} = 100$	$i_{D,PPN} = 10$	$i_{D,PPN} = 100$	$i_{D,PPN} = 10$
PD:						
PPN–DBS of 10 Hz	0.66	0.75	0.65	0.71	0.60	0.65
PPN–DBS of 25 Hz	0.57	0.75	0.59	0.72	0.57	0.66
PPN–DBS of 40 Hz	0.54	0.77	0.54	0.73	0.55	0.67
PD with STN–DBS:						
PPN–DBS of 10 Hz	0.71	0.70	0.72	0.74	0.74	0.77
PPN–DBS of 25 Hz	0.67	0.69	0.72	0.73	0.71	0.77
PPN–DBS of 40 Hz	0.66	0.69	0.67	0.73	0.68	0.78

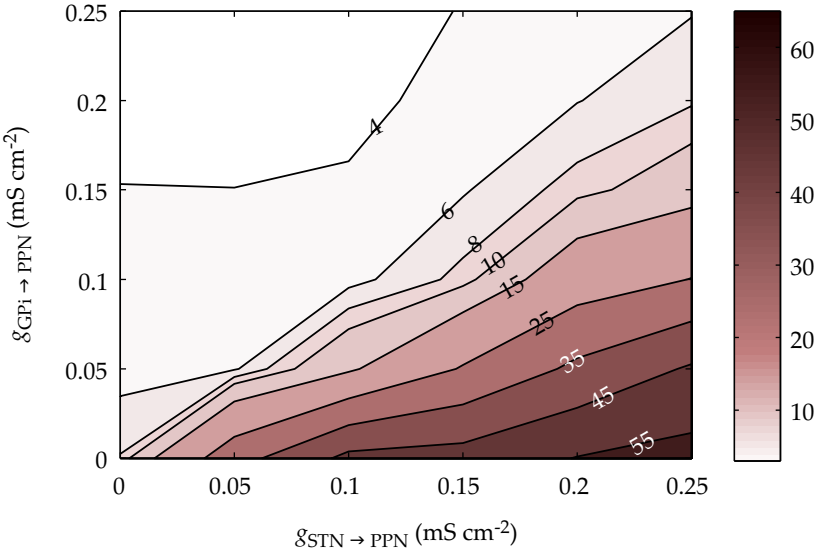

Figure 3.11 Contour plot of the mean frequency of the PPN for different choices for $g_{GPi \to PPN}$ and $g_{STN \to PPN}$. The PPN receives normal input and sends excitatory input to the STN cells. The synaptic conductance from PPN to STN is constant and set to 0.15 mS cm^{-2}.

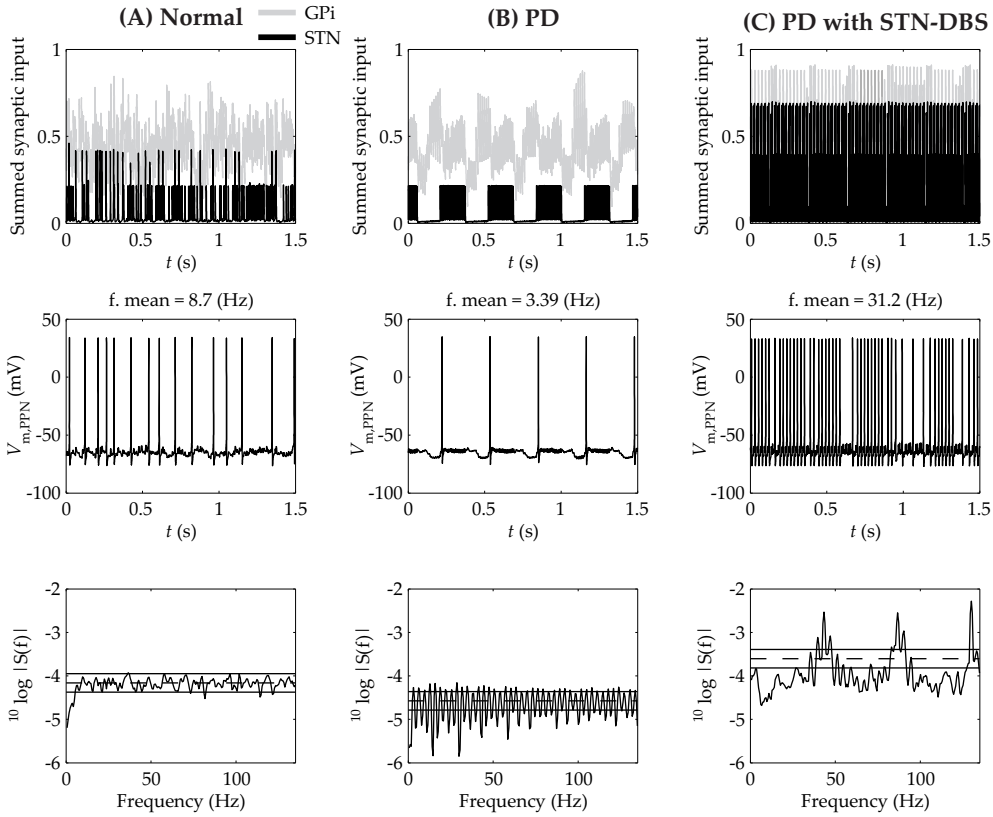

Figure 3.12 Response of the PPN cell to inputs from the STN and GPi under normal (**A**), PD (**B**) and PD with STN–DBS (**C**) conditions. The PPN cell sends also projections back to the STN; see Section 3.2.6. Top: total synaptic input from GPi and STN received by the PPN cell under the different conditions. The synaptic input of GPi is defined as the normalized sum of the synaptic variables over the four GPi cells projecting to the PPN cell. Same definition holds for the STN input. Middle: voltage trace of the PPN cell. Bottom: autospectrum of the PPN spike times; see Section 3.2.7 for computational details.

Effects of PPN and STN–DBS in the closed loop network

Figures 3.13 and 3.14 show the effect of PPN–DBS (no STN–DBS) with low and high stimulation amplitude on STN and PPN activity,respectively. Initially, without external stimulation (until 1 s), the STN cells fire in a bursty and clustered pattern, which characterize the PD state. The PPN cell fires regularly around 3 Hz. When PPN–DBS is switched on, indicated by the arrow at 1 s, low amplitude (10 μA cm^{-2}, Figure 3.13) stimulation changes the firing pattern of the PPN cell from regular to irregular while doubling its mean firing rate to 6 Hz. This low amplitude stimulation of the PPN influences the activity of the STN clusters only episodically. In contrast,

at high stimulation amplitude (100 μA cm^{-2}, Figure 3.14), the PPN activity is immediately overwritten by the stimulation, i.e. firing becomes locked to the stimulus. In turn some of the STN cells start firing regularly at a rate around 20 Hz. For low stimulus frequencies some clustering and bursting remains.

Next STN–DBS is turned on as well. We observe that the PPN activity becomes similar as described in section 3.3.4 (Figures 3.9B and 3.10B) and STN cells are locked to the STN–DBS.

STN–DBS does not interrupt the GPe bursty clustered firing patterns, also not when combined with PPN–DBS (Figure 3.15A). PPN–DBS alone does disrupt this pattern and eliminates this activity from the entire network (Figure 3.15B). The GPe cells start firing regularly at a rate around 20 Hz, like the STN cells do (Figure 3.14). Switching on STN–DBS reintroduces the clusters in GPe activity (not shown). Finally we stress that in all simulations we see that effects of PPN–DBS in the GPe and STN cells appears after several seconds.

3.4 Discussion

This Chapter investigates the response of a single PPN Type I cell to various inputs of the basal ganglia representing physiological, pathological and therapeutic cases. In particular, we look at the PPN spike output, that modulate the basal ganglia, and the relay of excitatory inputs as these are the key functions of the PPN cells [138].

First, we have developed a computational model for a PPN Type I cell and tuned it such that it reproduced known firing patterns [202]: Bursts after a period of hyperpolarization and spontaneous firing at 8 Hz (Figure 3.3). The model shows that switching between low and high frequency spiking is possible. Bifurcation analysis confirms this and reveals that there is a bistability between high and low frequency tonic spiking (Figure 3.5). For increasing current our PPN model shows an increasing frequency with a maximum of 450 Hz at $I_{\text{app}} = 50\mu$A cm^{-2}, where the periodic orbit disappears through a Hopf bifurcation (Figure 3.5). For higher currents the PPN cell is silent due to a depolarization blockade. Recently, Simon et al. [191] did whole patch clamp recordings on rat brain stem slices and found that PPN cells have a gamma frequency (40–60 Hz) plateau when they are depolarized with increasing current steps. This behavior was not significantly different among the three PPN cell types, except that PPN Type I cells fire faster than PPN Type II or PPN Type III cells during the beginning of the current injection. Simon et al. [191] did not show hyperpolarization steps. In addition they did not observe an abrupt switch between high and low frequency spiking as the applied current increases. In the low frequency range where we operate this discrepancy can be neglected.

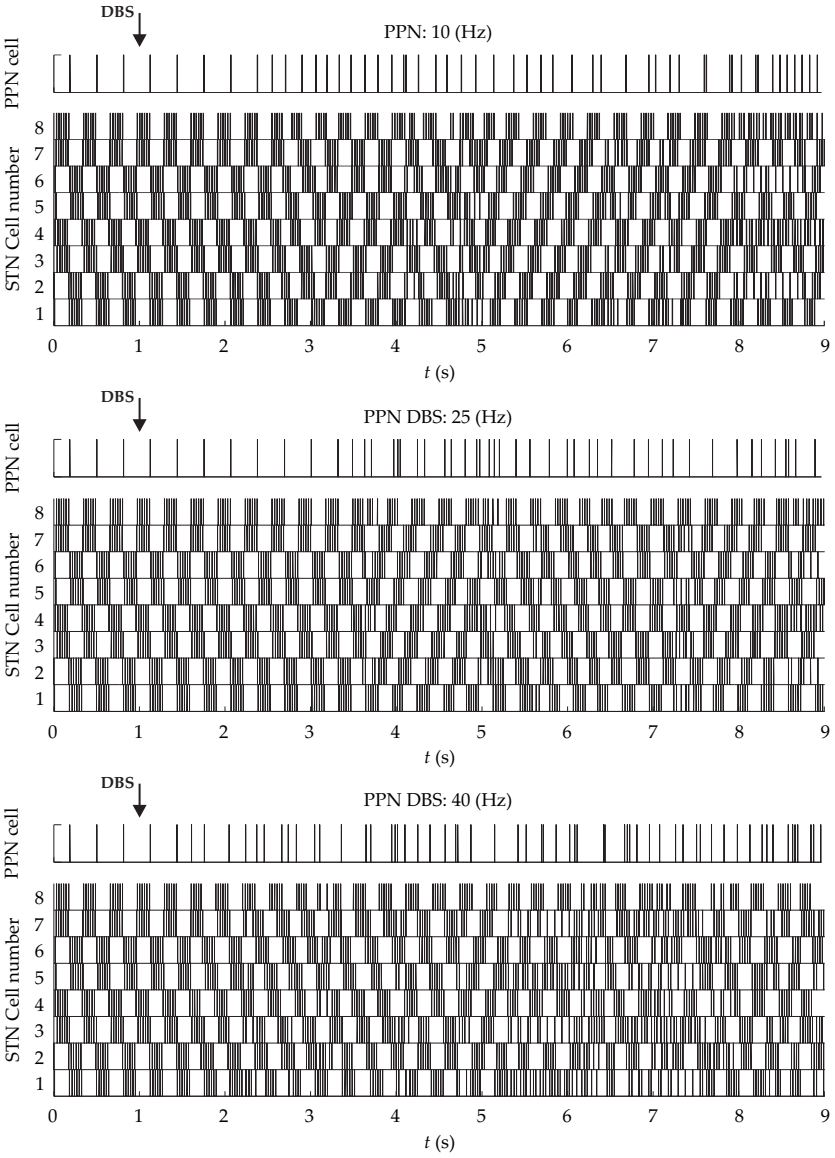

Figure 3.13 Response of the STN cells in PD to different PPN–DBS frequencies with low amplitude (10 μA cm^{-2}). For each PPN–DBS setting the spike trains of all eight STN cells and the PPN cell are shown. The arrow above the PPN spike trains at 1 s indicates when PPN–DBS is switched on. The pulse width for all settings is 0.15 ms

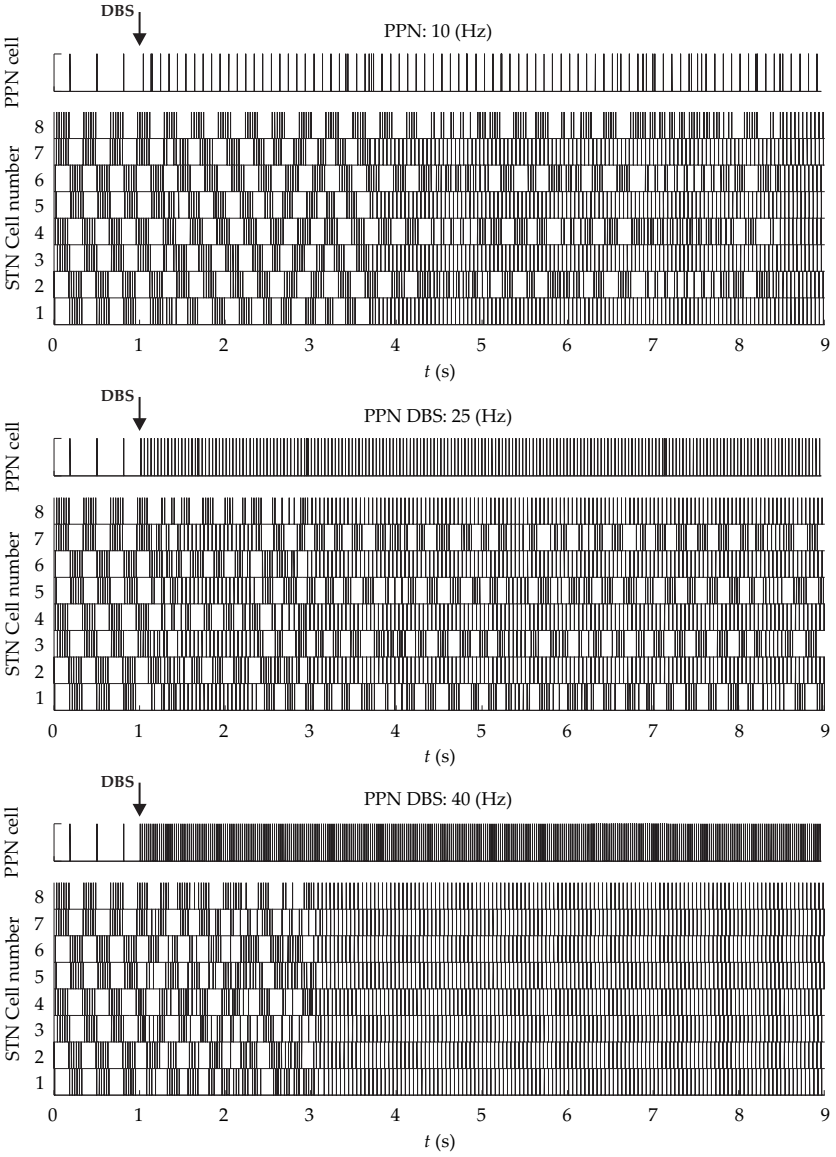

Figure 3.14 Response of the STN cells in PD to different PPN–DBS frequencies with high amplitude (100 μA cm^{-2}). For each PPN–DBS setting the spike trains of all eight STN cells and the PPN cell are shown. The arrow above the PPN spike trains at 1 s indicates when PPN–DBS is switched on. The pulse width for all settings is 0.15 ms

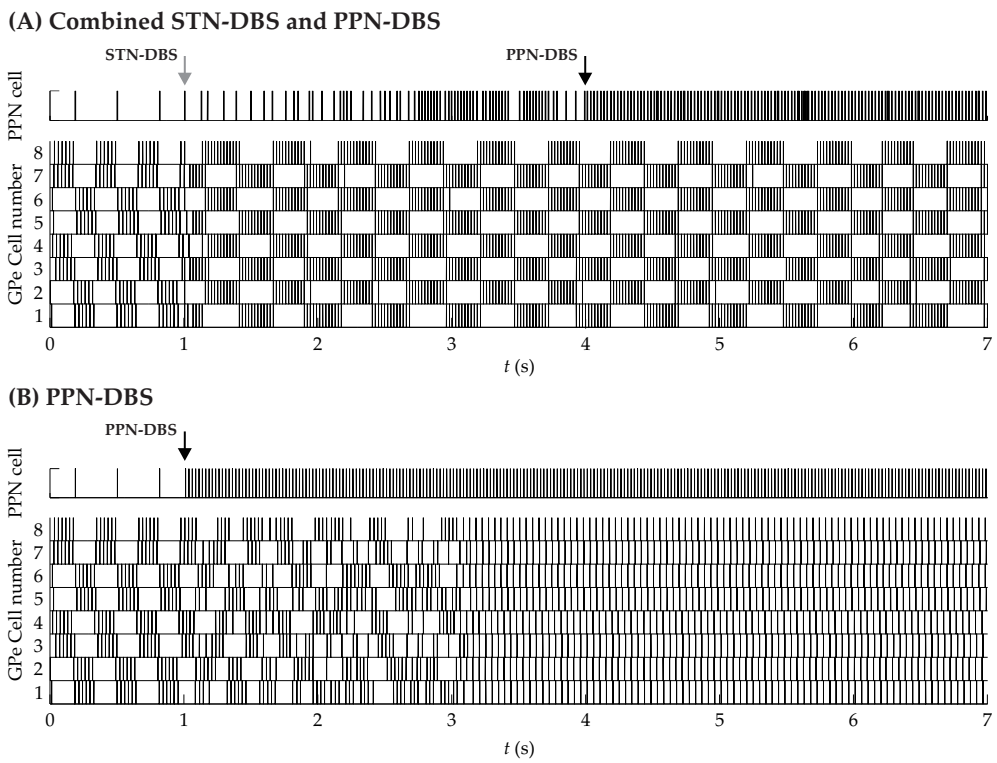

Figure 3.15 Effect of PPN–DBS and STN–DBS on the activity of GPe cells. PPN–DBS is applied with high amplitude (100 μA cm^{-2}) at 40 Hz and STN–DBS is applied at 130 Hz with amplitude of 400 μA cm^{-2}. For both stimulus a pulse width of 0.15 ms is used. Stimulation start at 1 s and 4 s indicated by the arrow. With STN–DBS clusters remain and longer in duration. Addition of PPN–DBS shows no change (**A**). With only PPN–DBS (**B**) the GPe clusters are disrupted after some transients

The PPN is an output structure to many brain structures and receives modulatory input from the basal ganglia. We generated such basal ganglia input for three scenarios (Normal, PD and PD with STN–DBS) using an existing computational model of the STN–GPe–GPi subnetwork [181]. The response of the PPN model depends on the balance between the excitatory input from STN and inhibitory input from GPi, see Figures 3.7 and 3.11. In general, the firing pattern of the PPN cell is more irregular for normal input, while the rate decreases and the pattern regularizes under PD conditions.

Experimental results are not conclusive about the balance between excitatory and inhibitory inputs to PPN and our simulations depend critically on this balance. On the one hand, Nandi et al. [153] have shown that injection of a GABA antagonist into the PPN of MPTP treated primates markedly attenuates akinesia. This result suggests that in PD the neuronal activity of the PPN is suppressed by an excess of

inhibition from GPi and SN_r leading to the hypoactivity symptoms. On the other hand, Breit et al. [31] shows that in anesthetized dopamine depleted rats PPN cells fire more irregularly and in bursts with an increased firing rate as compared to controls (18–20 Hz vs. 10–11 Hz). After lesion of the overactive STN in PD, the activity of the PPN is diminished, suggesting that the PPN is under major control of the STN.

In our model STN–DBS can modulate the activity of the PPN cell via a direct projection and via an indirect pathway via GPi. Florio et al. [58] found that in normal and dopamine depleted rats approximately 40% of the recorded PPN neurons respond to STN–DBS, resulting from an unbalance between the excitatory and inhibitory pathways. Our simulations with and without PPN feedback to the STN show an increased mean firing rate of the PPN if STN–DBS is applied. This suggests that the PPN cell receives more direct than indirect STN–DBS input. As a result the PPN cell locks to the STN–DBS input, but does not fire on every cycle. On the contrary, Florio et al. [58] found that approximately 85% of the responding PPN neurons responded to STN–DBS with inhibition, suggesting that the STN–DBS influence via the indirect inhibitory inputs are stronger. Moreover, they found that the balance between excitatory and inhibitory effects of the STN–DBS is independent from the dopaminergic nigral neurons. The balance is disturbed in rats with entopeduncular (rodents equivalent of GPi) lesion. In that case 75% of the PPN neurons become responsive to STN–DBS and are mostly (85%) excited by the STN–DBS.

A first report on PPN stimulation in human has shown that low frequency (20–25 Hz) stimulation of the pedunculopontine nucleus have acute improvement in motor function, such as gait and postural stability [169]. For frequencies higher than 30 Hz, the improvement in motor scores was variable, while very high frequencies ($>$180) worsened motor scores. Stefani et al. [196] studied at combined stimulation of the PPN and STN. Their key finding was that PPN–DBS with medication was inferior to medication only, while it improved motor scores in combination with medication and STN–DBS as compared to medication and STN–DBS only. These results were obtained after 6 months. Another clinical validation of PPN–DBS did not show significant improvements in combination with or without medication and with or without STN–DBS, after 1 year [57]. One may conclude that results of PPN–DBS vary from case to case.

To investigate the effect of STN–DBS and/or PPN–DBS in the network without projections from PPN to STN, we look at relay properties of the PPN cell (relay index). For the relay properties of the PPN cell it turns out that combined high frequency stimulation of the STN and PPN stimulation at low frequencies (10 Hz, 25 Hz and 40 Hz) is almost never better than exclusive STN stimulation. There are some doubts about the validity of the relay index. In the first place the main function of PPN Type I cells is to regulate the basal ganglia activity. No improvement in the relay

capability does not imply that PPN–DBS will not improve the basal ganglia activity. Second, the way we define the relay index. We record a successfully relayed excitatory cortical input if at least one PPN spike occurs in a specific time window after the input. As the PPN cell has a spontaneous activity, the spike can be the result of the cortical input or the result of its own spontaneous activity.

We also investigate the effect of STN–DBS and/or PPN–DBS on the pathological firing pattern of STN and GPe. For this purpose we extended our network with feedback projection from PPN to STN. Our main finding is that high amplitude (100 μA cm^{-2}) PPN–DBS alone eliminates the pathological bursty clustered firing pattern from the STN and GPe cells and replaces it with regular firing pattern around 20 Hz. This 20 Hz is independent from the stimulus frequency, but for the low frequencies (10 and 25 Hz) some clustering and bursting remain. In contrast STN–DBS and combined STN–DBS and PPN–DBS eliminate the pathological firing pattern only from the STN cells and lock the STN activity to the STN–DBS. We conclude that PPN–DBS alone is the best way to eliminate the clusters and thereby the low frequency (3 Hz, associated with tremor) oscillations from the entire network model. However PPN–DBS creates a 20 Hz oscillation in the STN and GPe cells, which could also be pathological. Bradykinesia is associated with maintained oscillations in the β band in the STN [112].

Capozzo et al. [41] have reported the effect of PPN–DBS on STN cells depend on the frequency and intensity of the stimulus. PPN stimulus with low frequency (10–40 Hz) and moderate intensity (50–400 µA) has an activated working on STN neurons. Either a higher intensity or a higher frequency of the stimulus suppress the STN firing. We have only looked at low frequencies ($\leq$40 Hz) and moderate intensities (10 and 100 μA cm^{-2}). We observe also an activated working on STN cells. Galati et al. [60] have shown in PD patient that PPN DBS at 25 Hz change the mean firing of STN neurons. In particular, the firing rate of the bursting STN neurons decrease and the firing rate of the irregular and regular STN neurons increase.

In many respects, our modeling approach is a first investigation how the PPN could be integrated into a larger network. A first extension can be made by investigating how various experimentally recorded LFP's would generate input to the PPN. Here a distinction must be made between medication on and off since axial signs are unresponsive to medication in late stages of PD. For instance, Androulidakis et al. [7, 8] found prominent 7–11 Hz oscillations in on medication states. Subsequently, Weinberger et al. [224] found prominent beta oscillations in LFP in three PD patients off medication. Neuronal firing did not show these oscillations, rather there pattern was bursty or regular. More recently, Tsang et al. [213] showed beta synchronization in pre-movement activity in the on medication state, but not in the off medication.

It is important to note that these inconsistencies could be due to slightly different recording areas.

Second, one could study the effect of the output of the PPN model on receiving descending pathways and nuclei, e.g. to spinal motor neurons. For the connection to motor neurons it would be interesting whether experimental results of Pierantozzi et al. [166] can be reproduced with our model. They hypothesize that PPN–DBS acts on spinal cord excitability improving the reticulospinal pathway. This could be tested with the output of our model.

Further tuning of our PPN Type I model according to recent data of Simon et al. [191] should be done. This requires more about the dynamics of the ionic currents, than currently available. At present the dynamics is based on neurophysiological data of the thalamocortical relay neuron ($I_{\mathrm{Na,L}}$, $I_{\mathrm{K,L}}$, I_{Na}, I_{K}, I_{T} and I_{hyp}) and the pre-Bötzinger neuron ($I_{\mathrm{Na,p}}$).

CHAPTER 4

Functional neuronal activity and connectivity within the subthalamic nucleus

Abstract In this Chapter we characterize the functional neuronal activity and connectivity within the subthalamic nucleus (STN) in patients with Parkinson's disease (PD). For this purpose, single units were extracted from intra-operative micro-electrode recording (MER) of 18 PD patients who underwent STN deep brain stimulation (DBS) surgery. The firing rate and discharge pattern of simultaneously recorded spike trains and their coherence were analyzed. To provide a precise functional assignment of position to the observed activities, for each patient we mapped its classified multichannel STN MERs to a generic atlas representation with a sensorimotor part and a remaining part. Within the sensorimotor part we found significantly higher mean firing rate ($P < 0.05$) and significantly more burst-like activity ($P < 0.05$) than within the remaining part. Coherence analysis of spike patterns between simultaneously recorded neuron pairs have demonstrated that significant coherent beta band activity (13–30 Hz) more often was present in the sensorimotor part of the STN than elsewhere in the STN ($P = 0.015$). In other frequency bands, there were no significant differences in coherence. We conclude that the sensorimotor part of the STN distinguishes itself from the remaining STN with respect to beta coherence, firing rate and burst-like activity. Interestingly, postoperative evaluation of target stimulation areas in the investigated PD patients with DBS shows a significant preference for the sensorimotor part of the STN. Our firing behavior analysis may help to discriminate the STN sensorimotor part for the placement of the DBS electrode[1].

[1] Adapted from M. A. J. Lourens, H. G. E. Meijer, M. F. Contarino, P. van den Munckhof, P. R. Schuurman, S. A. van Gils, and L. J. Bour. Functional neuronal activity and connectivity within the subthalamic nucleus in Parkinson's disease *Clinical Neurophysiology*, 2012.

4.1 Introduction

The striatal dopamine depletion, as observed in Parkinson's disease (PD), alters neuronal firing rates in basal ganglia nuclei, increasing firing rates in the striatum, the globus pallidus pars interna and the subthalamic nucleus (STN) and a slightly decreased discharge in the globus pallidus pars externa [83]. On the other hand, the type of discharge pattern, i.e., the interneuronal synchronization of basal ganglia neurons, is thought to be as important as the rate of discharge in the execution of smooth movements [19, 21, 28, 80]. In PD patients several alterations in the discharge pattern and interneuronal synchronization have been observed in neurons of the basal ganglia, including a tendency of neurons to discharge in bursts, an increased synchronization of discharge rate between neighboring neurons, and rhythmic and oscillatory behavior [32, 33, 62, 110, 120].

State of art models are inferring synchronously oscillating activity in one or several nuclei of the basal ganglia as being strongly related to PD motor symptoms, with the STN playing a pivotal role [80, 96]. Furthermore, it is recognized that the STN is subdivided in functionally segregated areas, including the sensorimotor, associative and limbic area [17, 75, 162]. It is also hypothesized that symptom-specific topography within STN is determined by distinct neuronal oscillatory activity, with beta-frequency oscillations (13–30 Hz) correlating to bradykinesia and rigidity [111, 113, 175, 223]. Theta-frequency oscillations in the basal ganglia (3–8 Hz) have been associated with both Parkinsonian tremor and essential tremor [44, 120, 197].

Deep brain stimulation (DBS) is an established therapy to reduce PD motor symptoms, when medication does no longer produce satisfying results [16, 76]. The STN is a commonly used target of DBS for PD. During the stereotactic surgery, to verify and refine the position of the DBS target, often micro-electrode recording (MER) is performed with up to five parallel tracks. Spiking activity and noise levels are visually inspected and interpreted real-time during surgery, but the obtained MER signals can also be analyzed more extensively and quantitatively off-line.

A way to obtain more knowledge about the functional anatomical network structure within the STN is to study the coherence between firing behavior of the STN neurons. Coherence between neuronal firing patterns is a quantitative measure to characterize neuron's synchronous activity which is a consequence of neuronal interconnections. In the current study we analyzed local coherence from the MER signal, i.e., the coherence between single units lying within the capture area of the micro-electrode (distance <150 μm). Also the global coherence was analyzed, i.e., the coherence between units that are identified on different micro-electrodes (distance >2 mm).

As a result of this analysis the spatial distribution of coherences within the STN across different frequency bands was obtained and we were able to relate coherent activity and connectivity in the different frequency bands to the sensorimotor part and the limbic associative part of the STN. In addition, we investigated the firing rate and discharge pattern of individual cells within the different areas of the STN. If the obtained information about neuronal activity is distinct for the two STN regions, it might be used to refine further the electrode implantation for DBS in the sensorimotor part.

4.2 Methods

Data of STN spiking activity obtained during DBS surgery in PD patients as part of the routine procedure was retrospectively retrieved. The position of each recording in each patient was mapped onto a generic STN. We generated spike trains from single units using spike sorting from the recorded activity. If a recording contained activity of reliably identified multiple units, the firing rate and discharge pattern of each unit were analyzed as well the interneuronal correlation of their activity. The Medical Ethical Committee of the Academic Medical Center in Amsterdam was officially consulted and denied the need for an approval for this study.

4.2.1 Patients

Micro-electrode recordings (MER) from PD patients who underwent stereotactic surgery from January 2008 until April 2011 for implantation of stimulating electrode in the STN were considered. In total MER data from 18 PD patients, with at least two simultaneously recorded single units, were used. MERs of 11 patients were bilateral. Demographic data and clinical information were retrospectively collected from the patient files (Table 4.1). The presence of tremor was preoperatively evaluated by a neurologist or Parkinson nurse specialized in movement disorders.

4.2.2 Surgical and micro-electrode recording procedure

The procedure for STN–DBS was a one-stage bilateral stereotactic approach, using MER to delineate the borders of the STN. Frame-based three-dimensional MRI reconstructions were used for STN targeting and trajectory planning. For this purpose

Table 4.1 Clinical and demographic characteristics of the patients included in the study, at the time of STN surgery. Also the number of micro-electrodes that are used for target localization, and the number of extracted neurons per STN side are given.

Patient	Gender, age (years)	Disease duration (years)	Total UPDRS-off score	Brain side	Tremor in the contra-lateral hemibody	UPDRS-off subscore contralateral side	Number of electrodes	Number of extracted neurons
1	M, 69	13	16	L	Yes	5	5	6
2	M, 59	9	35	R	No	9	5	10
3	M, 64	15	25	L	No	8	5	6
				R	No	7	5	7
4	M, 64	14	28	L	Yes	11	5	4
5	M, 62	12	46	L	Yes	14	5	15
				R	Yes	14	5	6
6	F, 57	18	47	L	No	15	5	19
				R	Yes	15	5	2
7	M, 59	13	59	L	No	21	5	6
8	M, 56	7	36	R	Yes	15	3	4
9	M, 62	27	46	R	No	17	5	6
				L	No	13	4	18
10	F, 51	6	38	L	No	17	4	4
11	F, 58	12	59	L	Yes	20	4	11
				R	Yes	19	3	10
12	M, 55	6	36	L	No	12	5	13
				R	No	13	4	6
13	M, 64	8	30	R	No	11	5	15
				L	No	8	3	9
14	M, 56	18	43	L	Yes	26	4	8
				R	Yes	10	4	8
15	M, 68	32	49	L	Yes	17	4	2
				R	Yes	14	4	8
16	M, 63	12	51	R	Yes	17	3	9
				L	Yes	14	3	10
17	M, 47	13	35	L	Yes	17	3	2
18	F, 68	18	77	L	Yes	29	4	6
				R	Yes	21	4	18

Abbreviations: M, male; F, female; L, left; R, right; UPDRS-off, Unified Parkinson's disease rating scale off medication.

the Leksell stereotactic frame and Leksell Surgiplan software (Elekta Instruments AB, Stockholm, Sweden) were used. On T1 MRI scans the position of the anterior commissure (AC) and posterior commissure (PC) were marked by the neurosurgeon and standard STN coordinates were obtained 12 mm lateral, 2 mm posterior and 4 mm below the midcommissural point (MCP). Adjustments were then made according to individual anatomy as visible on axial and coronal T2 MRI sequences, providing the stereotactic cartesian (x, y, z) coordinates of the STN target point. The trajectories of the micro-electrodes, that were attached to the frame and placed in a microdrive, were expressed in the stereotactic space by the arc and ring angle relative to the frame and by the STN target point. The microdrive depth zero of the central electrode corresponded to the MRI based STN target point. The paths were defined using the following criteria: anterior angulation to intercommissural line of 15–20°, lateral angulation from midline 20–30°, entry on top of a gyrus and avoiding sulci, cortical surface veins, and lateral ventricles. Under local anesthesia a 12 mm diameter burr-hole in the skull was made centered on the stereotactically identified entry point. All patients were awake during the entire recording session and without any sedatives. Surgery was performed following overnight withdrawal of anti-Parkinson medication.

Extracellular single/multi-unit micro-recordings were performed from small polyamide-coated tungsten micro-electrodes (FHC micro-electrode 291; impedance 1.1 ± 0.4 MΩ measured at 220 Hz, at the beginning of each recording session) with 20 μm exposure, mounted on a sliding cannula. Three to five steel cannulas and micro-electrodes (Table 4.1) were used and were placed in a so-called Ben's gun, with a central cannula directed to the planned STN coordinates and four parallel cannulas equally spaced around the central position with a center-to-center distance of 2.0 mm (anterior, posterior, lateral and medial cannulas). Starting 6–8 mm above the MRI-calculated STN target, the micro-electrodes were advanced simultaneously in 0.5-mm-steps by a manual microdrive. Advancing was stopped when electrical activity typical of substantia nigra cells was recognizable in at least one of the electrodes or when a significant decrease of electrical activity was present in all recordings. Clinical testing was performed at several sites by an experienced movement disorders neurologist. The permanent quadripolar DBS electrode (Model 3389) was implanted at the site with the best therapeutic window, i.e., best effect on motor symptoms and higher threshold for side-effects. The final position of all DBS electrodes was verified by co-registration of post-operative CT with pre-operative MRI [43].

Signals were recorded with the amplifiers (10,000 times amplification) of the Leadpoint system (Medtronic, Minneapolis, MN), and were analog bandpass filtered between 500 and 5000 Hz (-3 dB; 12 dB/oct). Data were digitized and stored for off-line analysis using both the Leadpoint system and a CED 1401 interface controlled by

Spike2 (Cambridge Electronic Design, Cambridge, UK). The Leadpoint system sampled its analog output signal at 12 kHz using a 16-bit A/D converter and afterward up-sampled it internally to 24 kHz. On each insertion depth of the electrodes, multi-unit segments were stored with Leadpoint for 10–20 s together with depth information, while the whole MER session was stored with Spike2. To obtain the Spike2 data the digital output of Leadpoint system was fed into a 16-bit D/A converter, and its output was filtered with a 3 kHz low-pass filter (-3 dB; 6 dB/oct). The signal was digitized again with a sampling rate of 20 kHz, using the CED 1401 interface. To annotate the Spike2 data with depth information we matched it with the 10–20 s Leadpoint recordings. All further processing and data analysis were performed off-line using MATLAB (Mathworks, Inc., Natick, MA, USA) and the annotated Spike2 data. Before we used the raw Spike2 data for spike train extraction it was filtered between 300 and 5000 Hz using a 2nd order non-causal Butterworth filter.

4.2.3 Fitting an atlas STN to MER

We determined for each STN recording the specific location inside the STN. For this we mapped the spatial stereotactic coordinates of the MER onto a generic atlas representation of the STN available within the software package Cicerone [140]. Details of the creation of this STN atlas, in the form of a three-dimensional polygon surface, can be found in Butson et al. [35]. The Leksell stereotactic coordinate system is a right-handed coordinate system, the positive x-axis being orientated to the left, the positive y-axis pointing anterior and the positive z-axis pointing downwards, the origin of the stereotactic coordinate system thus being in the superior posterior corner on the right side. We converted the coordinates such that the origin was at midpoint of the AC–PC line (MCP) and y orientation was retained, whereas the x and z orientation were reversed (Figure 4.1). This was done to get the same origin and orientation as the AC–PC coordinate system of the generic atlas used. Depending on how well the neurosurgeon aligns the stereotactic y-axis with the AC–PC line, there may be a small angle between the axes of the two coordinate systems. The location of each MER site could then be defined as a specific point in the AP–PC coordinate system (Figure 4.1).

During surgery the entrance and exit of STN were discerned visually by the neurophysiologist as an increase and decrease, respectively, in the background noise amplitude and neuronal firing [18, 29, 39]. In this way, each MER point was classified to be inside or outside the STN. We adopted the method of Luján et al. [125] to fit the MER points to the atlas representation of the STN. The method of Luján et al. [125] fits MER points that are identified to lie in either the STN or the thalamus to

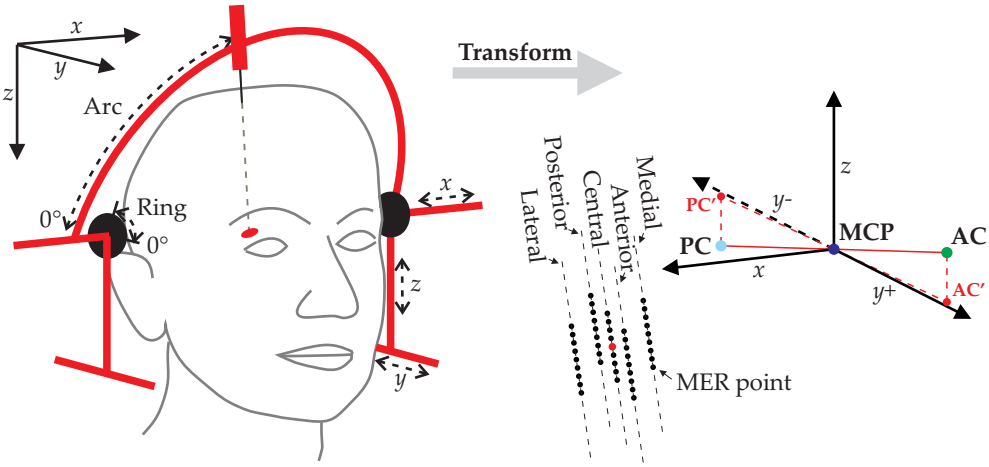

Figure 4.1 Schematic representation of the used coordinate systems. Left: Leksell stereotactic frame is used to define coordinates inside the brain. Attached to the frame is a semi-circular arc with a movable micro-electrode carrier. The arc is positioned in x, y, z direction, indicated by the dashed arrows on the right, in such a manner that its center corresponds with a planned target. The electrodes are always directed towards the target regardless of the position of the carrier on the arc (arc angle) or angling of the arc relative to the xy-plane (ring angle). Right: transformed stereotactic coordinate system with midcommissural point (MCP) as the origin. The trajectories of the micro-electrodes of a patient through the planned target (red point) with respect to the transformed coordinate system are shown. The anterior commissure (AC) and posterior commissure (PC) points, and the AC–PC line of the patient are shown as well. The points AC' and PC' are the projections of AC and PC on the xy-plane.

their corresponding atlas representations by minimizing a cost function, which depends on a set of bounded linear transformations. In contrast with Luján et al. [125], we used all MER points to fit those inside the STN to the atlas STN: the number of 'inside STN classified MER points' (blue locations, Figure 4.2) was maximized to lie inside the atlas STN and the inclusion of 'outside STN classified MER points' (red locations, Figure 4.2) were minimized to lie inside the STN.

The cost function for finding the optimal location of the atlas STN with respect to the MER points depended only on the Euclidean distances between the MER points and the surface of the atlas STN:

$$f(\mathbf{u}) = \sum_j w_j I_j \|\mathbf{x}_{\text{MER},j} - \mathbf{x}_{\text{STN center},j}(\mathbf{u})\|^2, \tag{4.1}$$

where $\mathbf{x}_{\text{MER},j}$ and $\mathbf{x}_{\text{STN center},j}$ are the x, y, z coordinates of the MER point j and its nearest polygon's centroid on the STN surface in the AP–PC coordinate system, respectively. The set of linear transformations of the atlas STN is defined by $\mathbf{u}$, which

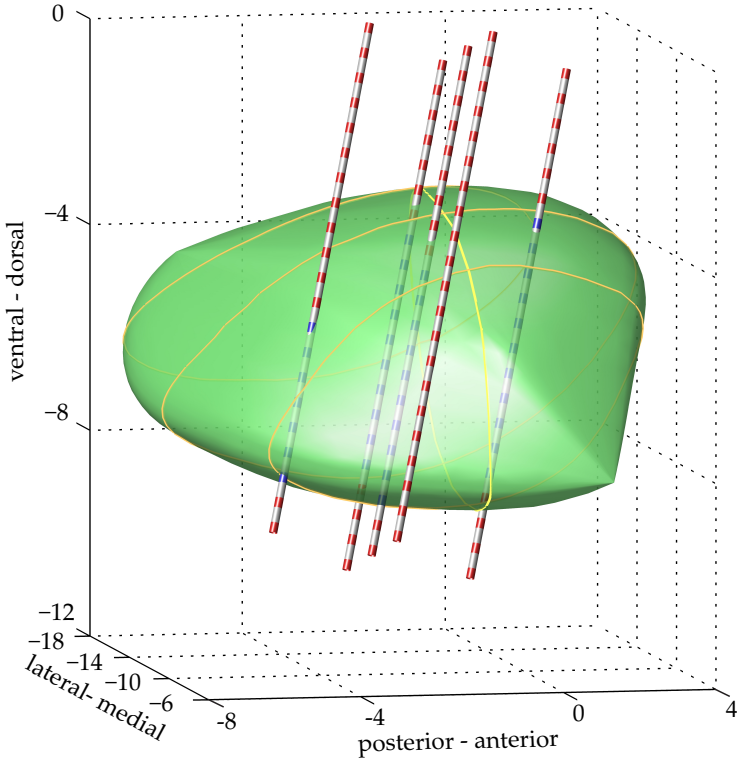

Figure 4.2 3D view of a single patient's left side atlas STN (green volume) fitting to the MER points (blue and red dots). The blue dots are 'inside STN classified MER points'. Initially, the center of the atlas STN is placed on the planned target point and oriented to the y-axis of the stereotactic coordinates system. From there the STN is translated, scaled and rotated to find the best fit.

allowed a maximum translation and rotation of 10 mm and 10°, respectively, in each direction, and a maximum scaling of $\pm 20\%$ along each axis. The boolean operator I was set to 1 if an 'inside STN classified MER point' was outside the atlas STN or an 'outside STN classified MER point' was inside the atlas STN. For 'inside STN classified MER points' we used a weight of $w = 20$, whereas for the remaining MER points we used a weight of $w = 5$.

To minimize the cost function we used the optimization toolbox within MATLAB. For each patient 50 realizations of the transformation vector were obtained using the global optimization algorithm simulated annealing (function *simulannealbnd*, default setting except for function tolerance of 10^{-4}, fast temperature update and *StallIterLimit* of 6000). Each realization was used as starting point of a local optimization solver to refine the realization (function *fmincon*, default setting except for a maximum of 1000 iterations and 3500 function evaluations, constraint tolerance of 10^{-1},

parameter tolerance of 10^{-2}, function tolerance of 10^{-4} and centered finite differences to estimate the gradients). The global optimization solver was initialized by placing the center of the atlas STN, defined in AC–PC coordinates, on the preoperative MRI defined target position. Furthermore, the atlas STN was rotated such that the AC–PC line was aligned with the y-axis of the stereotactic coordinates system. For each patient the realization with the minimal cost function was taken as optimal solution. In the case of more than one optimal solution, the realization with minimal cost function and minimal transformation of the atlas STN was used.

Based on its afferent and efferent connections, the STN is subdivided into three functional different territories: the sensorimotor part, the associative part and the limbic part. The medial third of the anterior two-thirds of the STN contains the limbic and a portion of the associative territories. The ventral aspect of the antero-lateral two-thirds of the STN composes the other portion of the associative territory. The dorsal aspect of the antero-lateral two-thirds and the posterior third of the STN are related to sensorimotor circuits [17, 75, 162]. We have divided the atlas STN into two regions: a part that consists mainly of the sensorimotor part described above and a remaining part that consists mainly of the associative part described above (Figure 4.3).

4.2.4 Location of active DBS electrode contact

After surgery, all contact points were tested in each patient to verify the therapeutic window: by stimulating at 60 μs and 130 Hz, the range of voltage between the threshold for effect on motor symptoms as defined by UPDRS III and the threshold for side-effects was evaluated. This procedure was performed by the Parkinson nurse specialized in DBS, blinded to the intra-operative data and micro-electrode recordings. The contact point with the best therapeutic window (lower threshold for benefit/best effect and higher threshold for side effects) was chosen for chronic stimulation. Patients came back to the outpatient clinic regularly after a period of about 6 weeks to verify the effect of chronic stimulation. At this point stimulation was increased or contact point changed if needed. For the present study, we collected clinical data from patient files and extracted the contact point that was used for chronic stimulation at least 6 months after surgery, that is when clinical conditions were considered stable.

The stereotactic microdrive depth of the center of the clinically most effective electrode contact was calculated as follows:

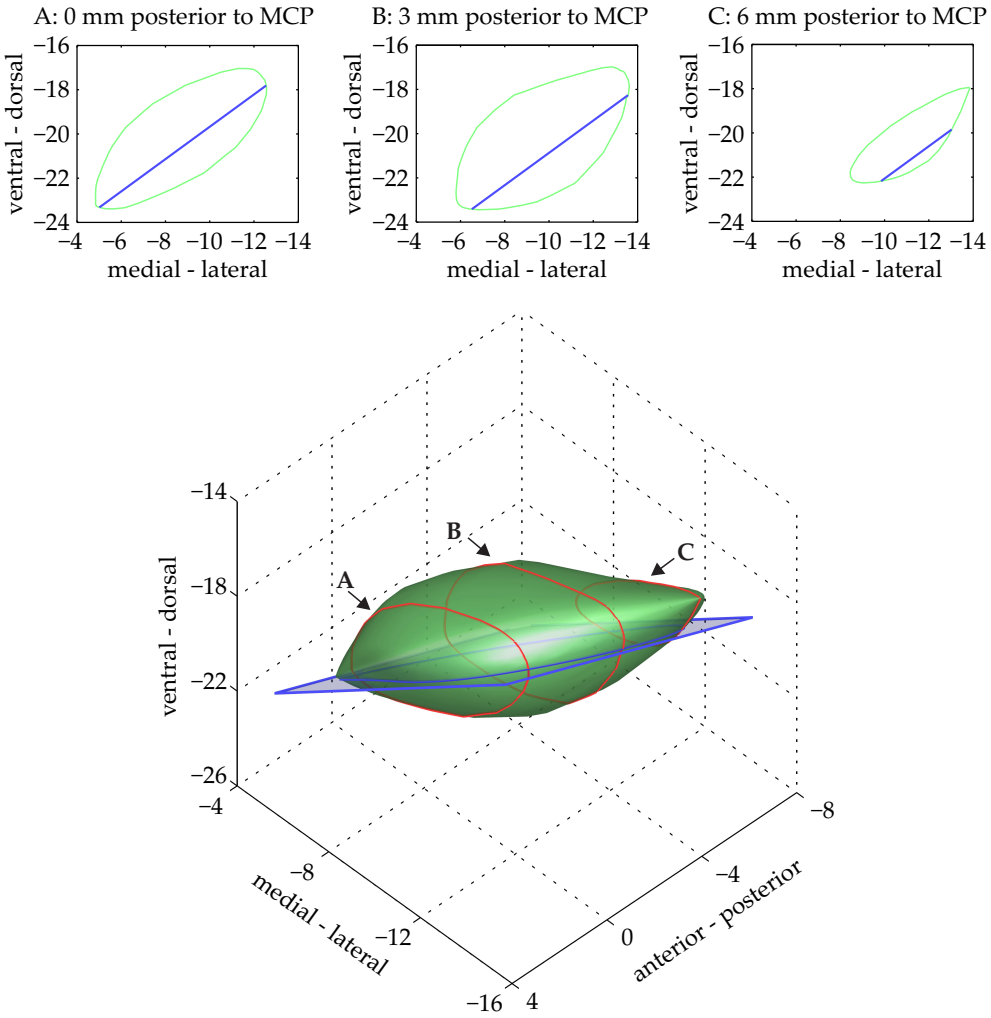

Figure 4.3 Based on afferent and efferent connections the STN was subdivided into a dorsal sensorimotor part and a ventral associative (remaining) part. Top: shows three coronal slices of the atlas STN. In each slice the blue line indicates the border between the dorsal and ventral part. Bottom: three-dimensional representation of the atlas STN subdivision. The blue plane indicates the border between dorsal and ventral part and the three red contours indicate the location of the above coronal slices.

$$D_{\text{active contact}} = D_{\text{contact zero}} - 1.5 I_{\text{contact}} - 0.75, \tag{4.2}$$

where $D_{\text{contact zero}}$ is the implanted depth of the bottom of contact zero (also retrospectively collected from the patient files), 1.5 is the center-to-center distance in millimeter of two adjacent contacts, I_{contact} is the contact number chosen for chronic DBS ($I_{\text{contact}} = 0$, 1, 2 or 3) and 0.75 is half of the contact length in millimeter. The AP–PC

coordinates of the active contact could then be defined by matching its depth with the MER trajectory where the DBS electrode was implanted.

4.2.5 *Data preparation*

Selection of stable MER

Only stable MER fragments that were recorded inside the STN for at least 10 s duration were used for analysis. To test the stability of the MER fragment we adopted the approach of Moran et al. [144]. Each fragment was divided into consecutive 1-s segments, which were split into 20 pieces of 50 ms. For each 50 ms piece, the root mean square (RMS) was calculated, yielding 20 RMS values for each 1-s segment. MER fragments were considered unstable if they failed to pass the Bartlett's test for equal variances of the RMS across all one second segments with $P < 0.0001$. Only the longest stable part of the MER fragment was further analyzed.

Spike sorting: spike detection, feature extraction and clustering

A typical MER fragment consisting of action potentials (spikes), background noise is shown in Figure 4.4. The spikes are generated by neurons located approximately within 150 µm from the electrode tip [36, 142]. Normally, on one needle, spikes may be recorded from 1 up to maximally 5 neurons. The background noise consists of neuronal activity from neurons lying further away from the electrode tip, and instrument and electrode noise. To obtain the neural activity of individual nearby neurons, the spikes have to be extracted from stable MER fragments. Moreover, each detected spike has to be assigned, with a high degree of reliability, to putative neurons.

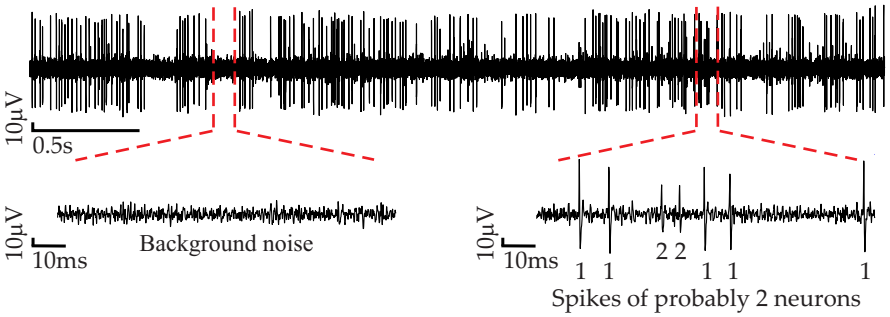

Figure 4.4 Example of a stable micro-electrode recording fragment that shows action potentials and background noise in the insets.

For detailed method for spike sorting see Appendix C. In short, local maxima of the MER signal that exceed 4.5 times the noise-level, which was estimated with the 'envelope' method [51], were flagged as a spike event. Subsequently, the waveform of each detected spike was obtained from the MER by extracting a data window of 1.2 ms around the time of the spike event. To remove waveforms that considerably overlap (overlapping spikes), spike events that occurred within 1 ms from each other were ignored (Figure 4.5A). A wavelet based method [89, 118, 174] was used to extract the six most discriminative wavelet coefficients of the spike waveform (Figure 4.5B). The six extracted wavelet coefficients were used as feature for the clustering step. For the clustering, a classification expectation maximization algorithm [42] was used, as implemented in KlustaKwik version 1.7 [81]. Finally, the sorted spike waveforms were transformed to spike trains that contained only the points in time when neurons fired (Figure 4.5C).

Evaluating the quality of the spike sorting

To address the question whether the sorted clusters of waveforms truly represented single neurons, a series of tests was performed. Failures in the identification of spikes (false negative) or assignment of a spike or noise event to a wrong cluster (false positive) are typical examples of sorting errors and may occur at each stage of the spike sorting algorithm. The overlap between pairs of clusters of sorted spike waveforms leads to both false negative and false positive errors. Cluster isolation was assessed using a projection method based on the Fisher's linear discriminant [84]. For any pair of clusters found on a single electrode, a Fisher's linear discriminant axis can be calculated from the mean and the covariance matrix of the two clusters [84]. Projecting every spike waveform of the two clusters onto the Fisher's linear discriminant between them resulted in two distributions of a single one-dimensional quantity (F_1 and F_2). The overlap between the histograms of F_1 and F_2 with bin width h and N bins was calculated according to:

$$FLD_{\text{overlap}} = \frac{\sum_i^N \mathbf{1}(F_{1,i}F_{2,i}) \min(F_{1,i}, F_{2,i}) h_i}{\min(\sum_i^N F_{1,i}h_i, \sum_i^N F_{2,i}h_i)}$$

with

$$\mathbf{1}(x) = \begin{cases} 0, & x = 0 \\ 1, & \text{otherwise.} \end{cases} \tag{4.3}$$

We considered a cluster to be well-isolated if the overlap with all other clusters recorded simultaneously on the same electrode satisfied $FLD_{\text{overlap}} \leq 0.05$.

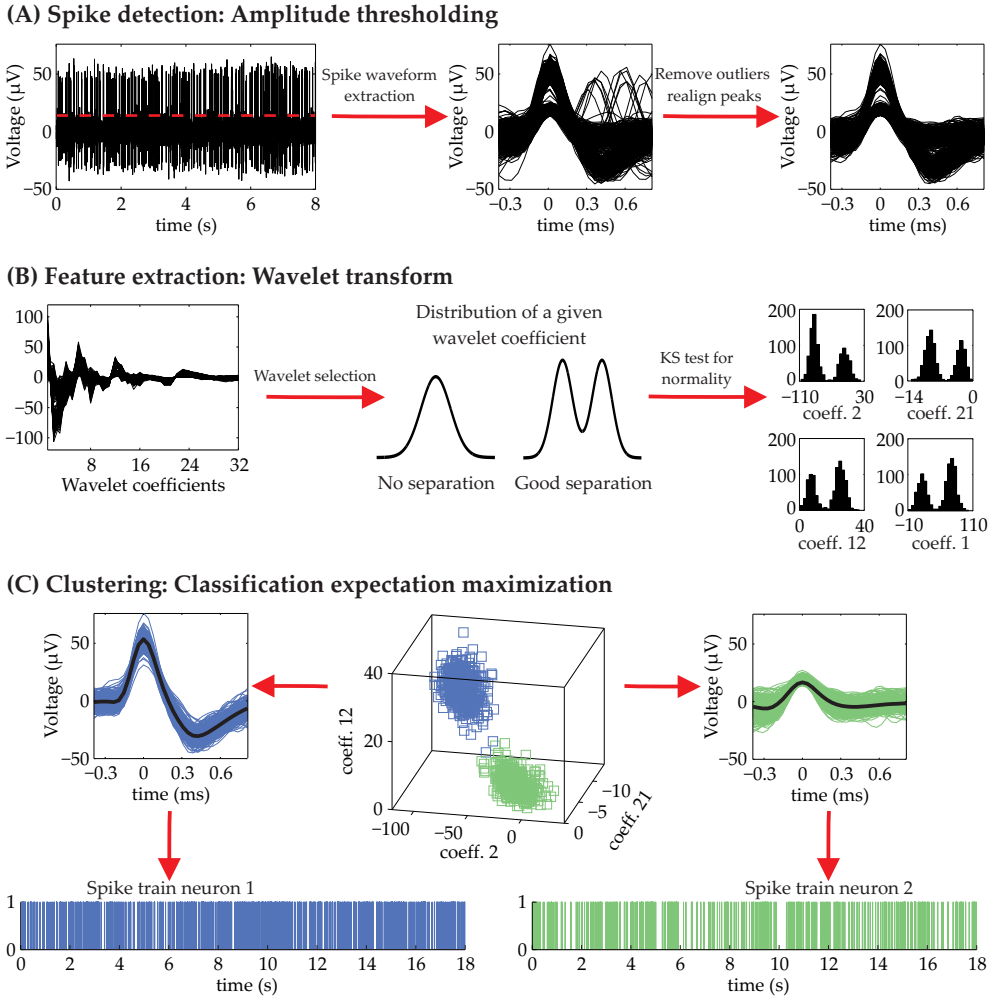

Figure 4.5 Illustration of the spike sorting algorithm on a stable 18-s long MER fragment of the left STN of patient 6: (**A**) Maxima with values above the threshold are detected as spikes. Left: first 8 s of the MER fragment. Red dashed line is the threshold, which is 4.5 times the noise-level, calculated according to Dolan et al. [51]. Middle: spike waveforms, extracted from the 18-s long MER fragment and aligned to their peak at time zero. Right: spike waveforms after removal of artefacts and overlapping spikes, and realignment of the peak. (**B**) A set of wavelet coefficients representing the relevant features of the spike waveforms is selected using the Kolmogorov–Smirnov test (KS test) for normality. Left: each curve represents the wavelet coefficients, calculated with a fourth-level discrete Haar wavelet transform, for a given spike waveform. Middle: schematic representation of possible distributions of a wavelet coefficient. Coefficients with a multi-modal distribution are candidate to use for spike waveform classification. Right: distribution of the four wavelet coefficients with the highest deviation from normality. (**C**) Selected wavelet coefficients serve as the input for the classification expectation maximization algorithm (KlustaKwik) [81]. Top: clustering algorithm identified the activity of two neurons with different spike waveform and separate cluster in the projection of the three wavelet coefficients with highest deviation from normality. Bottom: the sorted spike waveforms are transformed to spike trains.

A well-isolated cluster may still contain spikes from two neurons with very similar extracellular spike waveform. The multi-unit contamination was graded by evaluating the refractory period violation [54]. Finally, only clusters that were well-isolated and with a fraction of interspike intervals (ISIs) within the refractory period of 1.5 ms out of the total ISIs less than 2.5% were included.

We also neglected the MER fragment if the total number of overlapping spikes, i.e., if a spike occurs within 1 ms from another spike, was larger than 10% of the total detected spikes. The peak amplitude distribution of a cluster of spikes was fitted with a Gaussian distribution to estimate the number of spikes with peak amplitude below the detection threshold [84]. A cluster (neuron) was classified correctly if $\leq$ 10% of the spikes were subthreshold, otherwise it was classified as environmental.

In case a neuron was classified as correctly and not as environmental, an isolation score was calculated, which indicates how far the noise and the spike cluster are separated [101]. This isolation score takes values in the interval $[0, 1]$, where a score of 1 indicates perfect isolation. Thus, only correctly classified neurons with an isolation score ≥ 0.75 were included in the analysis.

Finally, we included only those neurons (correct or environmental) which had a roughly stable discharge rate over the recording period and a firing rate exceeding 10 spikes per second. Due to the limited recording duration, the stability of the discharge rate of the spike train was evaluated by visual inspection rather than statistical tests [67].

4.2.6 Spike train analysis

Firing rate and discharge pattern

For each identified neuron the mean firing rate over the recording period was calculated. The type of firing pattern of each identified neuron, i.e., regular, irregular and bursting was assessed as follows. Its discharge density histogram was estimated [104] and compared to three reference probability density functions (PDF) as proposed by Labarre et al. [116]. For the reference functions (1) a Gaussian PDF with mean 1 and variance 0.7, (2) a Poisson PDF with mean 1 and (3) a Poisson PDF with mean 0.8 were used to represent regular, irregular and bursting activity, respectively. The smallest distance of the estimated discharge density histogram of the neuron to the three reference PDFs determined the type of neuron.

Additional information about the firing pattern of a spike train was obtained by the coefficient of variation (CV) and the asymmetry index (AI) of its ISI (interspike interval) distribution. The CV is a measure for the variability of a spike train, defined

as the ratio of the standard deviation to the mean ISI. For a Poisson spike train (irregular) the CV equals 1 and for a perfect regular spike train the CV equals 0. The AI is defined as the ratio of the mode to the mean ISI. For a bell-shaped ISI-distribution the AI is close to one, while for a positively skewed ISI-distribution it is less than one.

Coherence analysis

To quantify the synchronization between two spike trains we used the notion of coherence ($C_{xy}(\lambda)$). The magnitude squared coherence provides a bounded measure of linear correlation between 2 stationary random processes $x(t)$ and $y(t)$ at frequency λ on a scale from 0 (no correlation) to 1 (perfect correlation):

$$|C_{xy}(\lambda)|^2 = \frac{|S_{xy}(\lambda)|^2}{S_{xx}(\lambda)S_{yy}(\lambda)}, \tag{4.4}$$

where S_{xx} and S_{yy} are the power spectral density of $x(t)$ and $y(t)$, respectively, and S_{xy} is the cross spectral density between $x(t)$ and $y(t)$.

We used the spectral estimation technique as described in Halliday et al. [74] and implemented in Neurospec (http://www.neurospec.org) to obtain these quantities for the spike trains. This spectral estimation technique is based on averaging of the modulus squared Fourier transform (periodogram) of disjoint segments of the spike train. Spike trains were divided into non-overlapping disjoint segments of 2^{14} samples and the mean value of each segment was subtracted. The finite Fourier transform of each disjoint segment was calculated without using a tapering window, providing a frequency resolution of 1.22 Hz. For additional smoothing of the spectra we used a Hanning filter.

The statistical significance of the coherence was assessed by estimating the distribution of the magnitude squared coherence under the null hypothesis of $|C_{xy}(\lambda)|^2 = 0$ (independent spike trains) and establishing a 99% confidence level from this distribution. To estimate the distribution, independent pairs of spike train 1 and 2 were created by randomly shuffling the ISIs of spike train 1. In the case both spike trains were recorded by the same micro-electrode, the ISIs of both spike trains were shuffled under the constraint that the union of the resulting shuffled spike trains had ISIs larger than 1 ms. This was done to mimic the dead time in the spike sorting. The magnitude squared coherence was computed for 1000 surrogate data pairs, and the 99th percentile of the coherence distribution was used as the 99% confidence level to determine significant coherence at each frequency.

The coherence spectrum was split up into five frequency bands: theta (3–8 Hz), alpha (8–13 Hz), beta (13–30 Hz), lower gamma (30–60 Hz) and upper gamma (60–100 Hz). Coherence between two spike trains at a given frequency band was judged as significant if at least one peak value of the magnitude squared coherence at that frequency band exceed the 99% confidence level.

4.2.7 Statistical analyses

Statistical analysis was performed using statistical software PASW Statistics 18 (SPSS Inc., Chicago, IL, USA). The mean firing rate and the ISI-distribution parameters (CV and AI) were not normally distributed for the two neuron groups formed by the STN region (sensorimotor or remaining) as assessed by the Shapiro–Wilk test. Therefore, comparison of these continuous variables between the two neuron groups was computed using the Mann–Whitney U-test. Electrophysiological differences in firing pattern between two neuron groups were evaluated by a Chi-square test. In the case the Chi-square test was significant, i.e., proportions of the firing pattern were not equal across the two STN region, we used Goodman *post hoc* comparative tests to determine which firing patterns were significantly different. This approach calculates for each contrast a Z-statistic and compares it to a critical value. We used the Scheffé critical value, which is found by taking the square root of the critical value in the original omnibus Chi-square test ($S^* = \sqrt{\chi^2_{\nu:1-\alpha}} = \sqrt{\chi^2_{2:1-0.05}} = \pm 2.45$, ν is degree of freedom and α is significant level). A contrast was considered to be significant as $|Z| > |S^*|$. The same approach was used to analyze the difference in firing pattern between tremor and no-tremor patients.

To analyze the difference in coherence between the sensorimotor part and remaining part of the STN, each calculated coherence was assigned to one of the two STN regions. If the recording sites of both spike trains were located in the same STN region the coherence was assigned to that region, otherwise the coherence was assigned to the STN region where the average position of both recording sites was located. The number of neuron pairs that exhibit a significant synchronization of their activity within a given frequency band as well as for the entire bandwidth from 3 to 100 Hz was determined for each STN region. The Fisher's exact test was then used to compare these numbers between the two STN regions. The same approach was used to analyze the difference in coherence between tremor and no-tremor patients and between local and global coherence.

A paired Student's t-test was used to compare mean values of the fitting. A probability level of $P < 0.05$ was considered to be statistically significant. All data are presented as means $\pm$ standard deviation.

4.3 Results

4.3.1 Fitting an atlas STN to MER

For each of the 29 STNs, the set of classified MER points was fitted to a generic atlas representation of the STN (Table 4.1). To evaluate whether the optimization method or the AC–PC line aligning method (Section 4.2.3) was better, we compared the percentage of correctly fitted MER points and the summed Euclidean distance of incorrectly fitted MER points to the atlas STN surface (fitting error). Figure 4.6 shows the distributions of the percentage of correctly fitted MER points and fitting error of all STNs for both methods. The optimization fitting method resulted in an atlas STN transformation that correctly fitted an average of $93.6 \pm 4.7\%$ of the classified MER points, while the AC–PC line aligning method only fitted $65.8 \pm 14.9\%$. The percentage of correctly fitted MER points was significantly improved by the optimization fitting method (paired t-test, $P < 0.000000005$). Also the fitting error was significantly smaller for the optimization fitting method than for the AC–PC line aligning method (paired t-test, $P < 0.00000005$; 1.4 ± 1.3 mm and 23.4 ± 15.8 mm, respectively).

Application of the optimization fitting method resulted in only five neurons fitted outside the STN of a total of 248 neurons localized with MER inside the STN. Evaluation of the final position of the active contact in the patients 1 year after surgery showed that in 21 cases they were located in our defined sensorimotor 'atlas STN', and in four cases within the remaining STN. In one case there was no DBS electrode implanted and in three cases the active contacts were located slightly above the dorsal border of the STN.

4.3.2 Spike train extraction

For spike train extraction 130 different sites within the STN were used. From the 130 sites 93 were located within the sensorimotor part of the STN and 37 were located within the remaining part of the STN. Per site 1–3 neurons, that satisfied our quality criteria, were extracted (see Section 4.2.5). This resulted in a total of 177 neurons (105 classified as correct and 72 as environmental) within the sensorimotor STN and 71 neurons (37 classified as correct and 34 as environmental) within the remaining STN. Mean duration of a spike recording in the sensorimotor and remaining part was 12.2 s and 13.2 s, respectively. Figure 4.7 illustrates the spike analysis that is performed for all simultaneously recorded neurons.

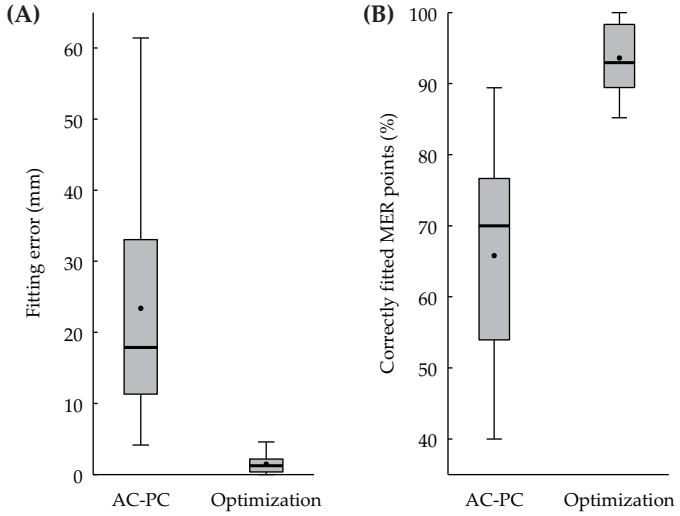

Figure 4.6 The fit performance of the optimization method is compared with its starting point (AC–PC line aligning). A box plot comparison of the percentage of correctly fitted MER points by the atlas STN (**A**) and fitting error (**B**). The lower line of each box indicates the 25th percentile (Q_1), the upper line indicates the 75th percentile (Q_3), and the horizontal lines above and below the boxes (whiskers) represent the data range. The bold line inside the box indicates the median, while the dot indicates the mean.

4.3.3 Firing rate and discharge pattern

Neurons within the sensorimotor part of the STN fired on average at a significantly higher rate than those within the remaining part of the STN (Mann–Whitney *U*-test, $P < 0.05$; 29.8 ± 13.2 Hz and 26.7 ± 12.9 Hz, respectively). The distributions of firing rates for neurons within the sensorimotor and remaining part are shown in Figure 4.8A, and mean values are summarized in Table 4.2.

Both STNs region displayed neurons with a regular, an irregular and a bursty firing pattern as determined by the method of Labarre et al. [116] (Figure 4.8D and Table 4.2). The most frequently observed neuronal firing pattern of both STN regions was irregular followed by bursty and then regular. Comparison of proportions of neurons in the three firing patterns demonstrated a statistically significant difference between the sensorimotor and remaining part of the STN ($\chi^2(2) = 10.7, P < 0.005$). Goodman *post hoc* tests revealed that bursty neurons were significantly more observed in the sensorimotor part than in the remaining part of the STN ($Z = 3.40, S^* = \pm 2.45, P < 0.05$). No significant differences were found with respect to the other two firing patterns (irregular: $Z = -1.84$; regular: $Z = -1.63$).

In addition, comparisons of AI and CV of the ISI-distributions for the extracted spike trains between the two STN parts demonstrated a significantly lower mean of

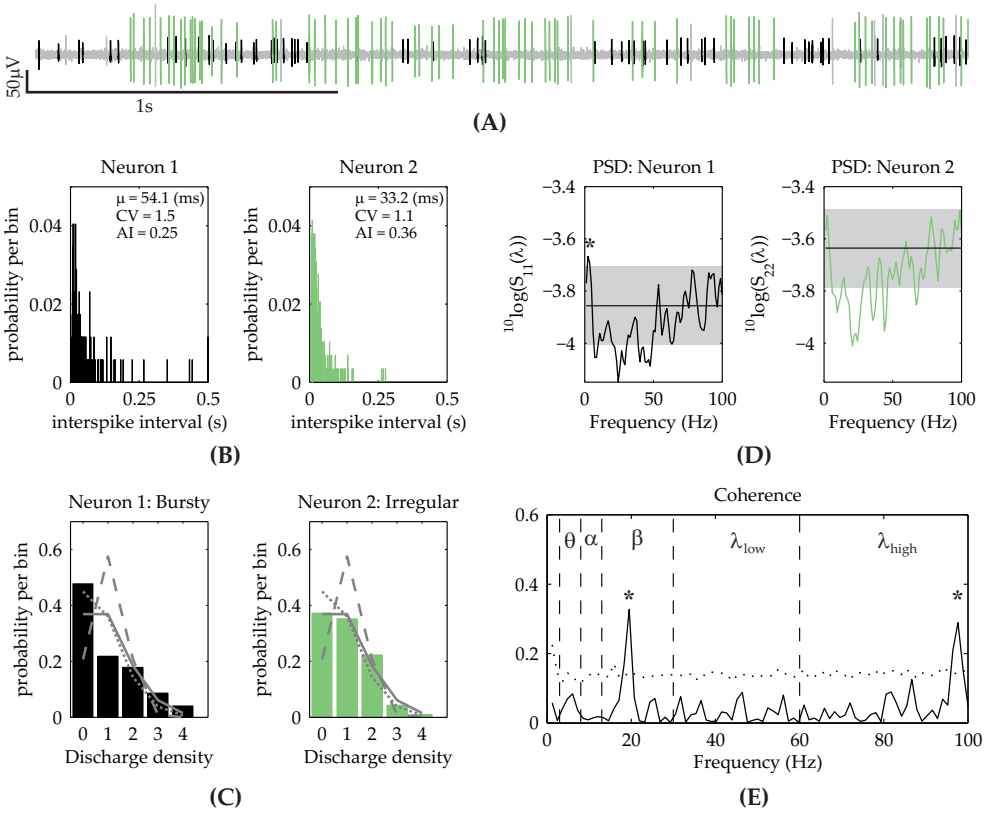

Figure 4.7 Spike analysis of two simultaneously recorded neurons of patient 1. (**A**) Part of a raw MER of 10 s duration with the two extracted neurons displayed in black and green. (**B**) Interspike interval (ISI) distribution of both neurons with a CV > 1 and small AI. This means they have a high variable discharge rate and positively skewed ISI-distribution. For each neuron the ISI-distribution was constructed with a resolution of 1 ms and a maximal time interval of 500 ms. (**C**) Histograms of the discharge density of both neurons. The histograms are constructed by dividing a spike train into consecutive interval of length t, the mean ISI (μ), and count the number of spike in each interval. The three curves on the histograms represent the reference functions: dashed curve for Gaussian PDF (regular firing: mean 1 and variance 0.7), solid curve for Poisson PDF (irregular firing: mean 1) and dotted curve for Poisson PDF (bursty firing: mean 0.8). The density histograms of neuron 1 fit well with the dotted curve (bursty) and neuron 2 with the solid curve (irregular). (**D**) Power spectral density (PSD). Shaded area indicates 95% confidence interval of the absence of oscillatory activity and the horizontal line inside the shaded area indicates the asymptotic value of the spectrum. Neuron 1 shows a significant peak at 2.5 Hz. (**E**) Coherence function between the two neurons with the dotted line as the 99% confident level and the dashes vertical lines indicating the borders of frequency bands. There is a large significant peak in the beta band, and also a significant peak in the high gamma-band.

AI and higher mean of CV (Mann–Whitney U-test, $P < 0.001$; Table 4.2, Figure 4.8B and C) for the sensorimotor part, which is in line with the finding that STN spike activity in this part is more bursty.

Neurons extracted from tremor ($n = 129$) and non-tremor patients ($n = 119$) had a comparable distribution of the firing pattern ($\chi^2(2) = 1.07, P = 0.59$, see Table 4.3).

Table 4.2 Electrophysiological characteristics of the spike trains within the sensorimotor and remaining part of the STN.

STN region	Firing pattern	n (%)	mean firing rate (Hz)	CV of the ISI	AI of the ISI
Sensorimotor	Regular	10 (5.6)	43.3 ± 25.1	0.72 ± 0.09	0.57 ± 0.19
	Irregular	106 (59.9)	32.1 ± 11.3	1.07 ± 0.17	0.28 ± 0.12
	Bursty	61 (34.5)	23.7 ± 10.6	1.41 ± 0.26	0.20 ± 0.10
	Total	177 (100)	$29.8 \pm 13.2^{*}$	$1.17 \pm 0.28^{**}$	$0.27 \pm 0.14^{**}$
Remaining	Regular	9 (12.7)	28.5 ± 13.5	0.79 ± 0.16	0.57 ± 0.27
	Irregular	51 (71.8)	26.5 ± 13.7	0.99 ± 0.16	0.39 ± 0.18
	Bursty	11 (15.5)	25.7 ± 8.2	1.40 ± 0.18	0.22 ± 0.07
	Total	71 (100)	26.7 ± 12.9	1.03 ± 0.23	0.38 ± 0.20

Values for firing rate, CV and AI are means $\pm$ standard deviation. Percentage values for the firing pattern in parentheses. Asterisks denote significant differences between the neurons in the sensorimotor and remaining part of the STN (Mann–Whitney U-test; $^{*}P < 0.05$ and $^{**}P < 0.001$). Note that statistics analysis is only performed on values of the total neurons in each STN region. *Abbreviations*: CV, coefficient of variation; AI, asymmetry index; ISI, interspike interval; STN, subthalamic nucleus.

Table 4.3 Distribution of the three firing patterns for neurons extracted from tremor and non-tremor patients.

Tremor	Firing pattern	n (%)
Yes	Regular	12 (9.3)
	Irregular	81 (62.8)
	Bursty	36 (27.9)
No	Regular	7 (5.9)
	Irregular	76 (63.9)
	Bursty	36 (30.3)

Percentage values are given in parentheses.

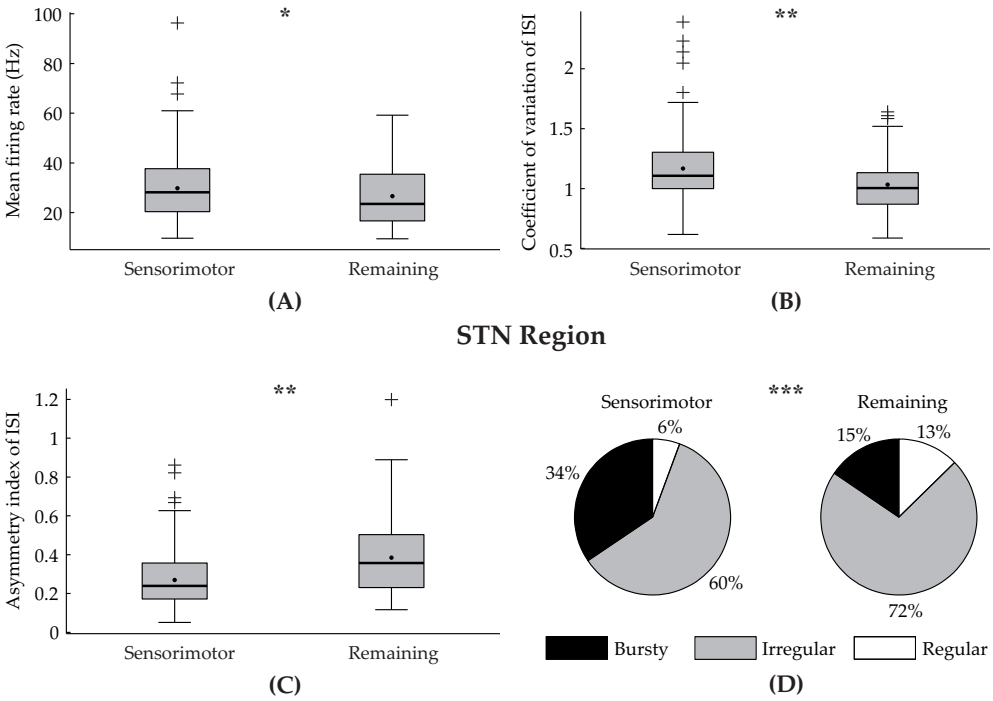

Figure 4.8 Statistical comparison of the firing rate (**A**), the ISI-distribution parameters CV (**B**) and AI (**C**) and distribution of the types of firing patterns (**D**) between the neurons in the sensorimotor and remaining part of the STN. The lower line of each box in A, B and C indicates the 25th percentile (Q_1), the upper line indicates the 75th percentile (Q_3), and the horizontal lines above and below the boxes (whiskers) represent the data range. The data range is defined as $1.5 * (Q_3 - Q_1)$ above Q_3 and below Q_1. Data values outside this range are plotted as $+$ markers. The bold line inside each box indicates the median, while the dot indicates the mean. Asterisks denote comparisons where statistical significance is reached (Mann–Whitney U-test; $^{*}P < 0.05$ and $^{**}P < 0.001$; χ^2-test; $^{***}P < 0.005$).

4.3.4 Coherence analysis

The synchronization within pairs of simultaneously recorded neurons was quantified with the coherence. Simultaneous recordings were obtained from 171 pairs of neurons, from which 129 were assigned to the sensorimotor STN and 42 to the remaining STN. When all frequencies bands were considered, 77 of 129 (59.7%) of these pairs in the sensorimotor STN and 22 of 42 (52.4%) in the remaining STN exhibited a significant coherence in at least one frequency band. The significant coherence in the two parts was not significantly different (Fisher exact test, $P = 0.47$). Figure 4.9 shows the proportion of neuron pairs having significant coherence across the five frequency bands. In both STN regions, neighboring STN neurons showed synchronized activity in all frequency bands. In the theta, alpha, beta and low gamma band,

on average significant coherence between neuron pairs was more often observed in the sensorimotor STN than in the remaining STN, while the opposite was seen for the high gamma band. Except for the beta band (Fisher exact test, $P = 0.015$) this difference between the two STN areas did not reach statistically significance.

Of 171 coherences, 122 were calculated between neurons recorded from one micro-electrode (local coherence) and 49 were calculated between neurons recorded from two separate micro-electrodes 2–4 mm apart (global coherence). When all frequencies bands were considered, the percentage of significant local coherence was not significantly different than the percentage of global coherence (Fisher exact test, $P = 0.30$; 60.7% and 51.0%, respectively). Moreover, the proportions of significant coherence for each frequency band did not significantly differ across the type of coherence, see Table 4.4.

We extracted 81 pairs of neurons from 17 STN where in the contralateral hemibody of the PD patient tremor was present. There was no difference between these 'tremor' pairs and the remaining pairs ($n = 90$) with respect to the distribution of significant coherence across frequency bands, see Table 4.4.

Table 4.4 Distribution of significant coherence between simultaneously recorded neuron pairs across frequency band as function of type of coherence and as function of tremor.

Frequency band	Type of coherence			Tremor		
	Local ($n = 122$)	Global ($n = 49$)	P-value	Yes ($n = 81$)	No ($n = 90$)	P-value
Theta	7 (5.7)	5 (10.2)	0.33	6 (7.4)	6 (6.7)	1.00
Alpha	9 (7.4)	1 (2.0)	0.29	5 (6.2)	5 (5.6)	1.00
Beta	34 (27.9)	12 (24.5)	0.71	25 (30.9)	21 (23.3)	0.30
Gamma low	23 (18.9)	11 (22.4)	0.67	18 (22.2)	16 (17.8)	0.57
Gamma high	28 (23.0)	11 (22.4)	1.00	21 (25.9)	18 (20.0)	0.37

Percentage values are given in parentheses. P-values are based on Fisher exact test.

4.4 Discussion

The current study shows that single neurons in the sensorimotor part of the STN of PD patients have significantly higher mean firing rate and exhibit significantly more burst-like activity in comparison to neurons in the remaining part of the STN. Furthermore, coherence analysis of spike patterns between neuron pairs in the Parkinsonian STN has demonstrated that significant coherent beta band activity is present

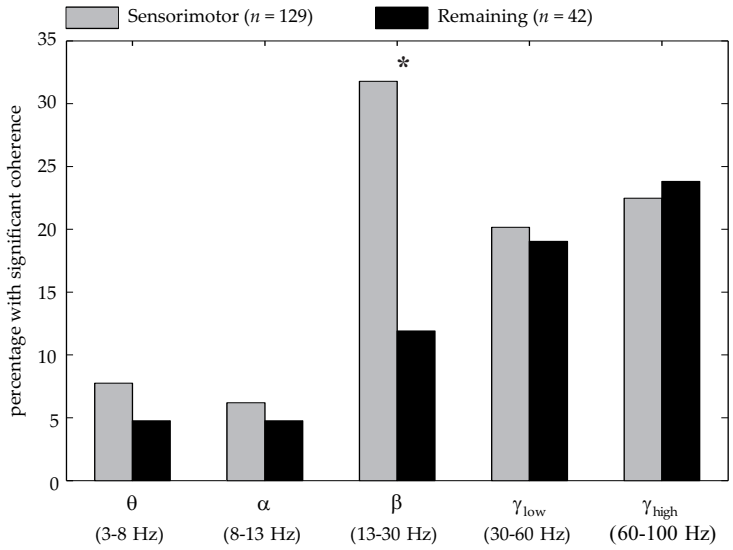

Figure 4.9 Distribution of significant coherence between simultaneously recorded neuron pairs across frequency band in the sensorimotor ($n = 129$) and remaining ($n = 42$) part of the STN. Neighboring STN neurons in both STN region show synchronized activity in all frequency bands. Proportion of significant coherence in the beta frequencies (13–30 Hz) in the sensorimotor STN is significantly higher than that in the remaining STN (Fisher exact test; $^*P = 0.015$).

more often in the sensorimotor part of the STN than elsewhere in the STN. In other frequency bands this difference in coherence cannot be demonstrated.

4.4.1 Dorsal–ventral versus sensorimotor part of the STN

Earlier studies, that have investigated differences in neural activity within the STN, have subdivided the STN in successive adjacent layers going from the dorsal to the ventral border but then along the stereotactic z-axis or the electrode trajectory [6, 44, 178, 188, 212, 223, 230]. In contrast to these studies, we have divided a generic atlas representation of the STN into two regions based on the functional territories of the STN, which are based on earlier studies in animal and human with the sensorimotor circuit more predominantly located in the dorsolateral STN [150, 162, 178]. Therefore, we have mapped for each patient its classified multichannel MERs to what we call the 'atlas STN'. This provides a more precise functional assignment of position to the observed activities (MER). Of 29 STNs analyzed in this study, 28 received a permanent DBS electrode from which 24, 1 year after surgery, appeared to have their clinically most effective contact in our defined sensorimotor 'atlas STN' or slightly above it and only four in the limbic associative 'atlas STN'. This data con-

firms that the sensorimotor part of the STN is the preferential location for DBS. The reason why some final contact points are located more ventrally from the sensorimotor part of the STN is partly due to unacceptable side effects at other locations as well as an inherent inaccuracy of about 1 mm in the location of the final contact point used for stimulation. Therefore, it must be concluded that in the sensorimotor part of the STN, where DBS appears most effective, also the spike characteristics of single neurons are different including higher mean firing rate, more burst-like activity and more often interneuronal coherence in the beta band.

The literature is not unambiguous as to how the STN should be subdivided into functionally different territories [107]. Prior to spike train analysis we subdivided the 'atlas STN' into two parts such that our defined sensorimotor 'atlas STN' corresponded closely to the sensorimotor part defined in the work of Benarroch [17], Hamani et al. [75], Parent and Hazrati [162]. Another unresolved question is whether the border between the different functional territories of the STN is sharp, as it is in our case, or a gradient.

4.4.2 Multi-unit versus single unit analysis

Instead of following the approach of extracting the envelope of the total MER signal by high-pass filtering and full-wave rectification [143, 144, 148], we concentrated our analysis specifically on spike trains from single units extracted from the MER signal, which in fact consists of a superposition of multiple units. In this way, we are able to distinguish between various firing patterns of STN neurons. In addition, information on functional connectivity between neighboring neurons and neurons that are several millimeters apart can be obtained via local and global coherence analysis.

To have full control over how spikes from the MERs are extracted and to assign each spike to putative neurons, instead of using existing spike sorting software, in the current study a new spike sorting algorithm has been developed. Except that the current spike sorting algorithm makes use of existing methods for each step (spike detection, feature extraction and clustering), it is optimized for our data by combining suitable methods. In most studies that make use of spike sorting [6, 188, 197, 223], declarations of the spike trains quality, including whether they are well-isolated, are made without tests and/or are only based on visual inspection. In contrast, we have used existing tests [54, 84, 101] to address the quality of the spike trains in an objective and standardized manner.

4.4.3 Percentage of coherent neuron pairs in beta band

This study confirms the observation of other studies [6, 120, 197, 223] that within the STN, pairs of neurons can be found that fire synchronously in the beta band. We found that 26.9% of the pairs recorded from the same or two separated micro-electrodes were significantly coherent within the beta band. This is comparable to the 25.4% in Weinberger et al. [223] and 30% in Levy et al. [120], where coherence was calculated between two single/multi-unit spike trains recorded from two separate micro-electrodes.

Interneuronal coherence in the beta band was observed in a lower proportion of 17.9% in a study of Amtage et al. [6]. One of their explanation for the relatively low beta synchronization was that only patients with strong rest tremor were selected, suggesting that beta synchronization was more a feature of the other PD symptoms. In contrast, Levy et al. [120] did not find beta band synchronous pairs in patients without tremor. This led them to conclude that beta oscillatory activity was present primarily in patients with tremor. In our group of patients we did not find a relation between tremor and interneuronal coherence in any of the five frequency bands. This is in agreement with two other studies [197, 223], where also interneuronal coherence in the beta band is found in PD patients without tremor.

In the current study beta coherence was present in 30.4% (14 of the 46) of the cases where beta peaks were detected in the spike pattern of at least one of the two single neurons. This finding is not in agreement with Weinberger et al. [223], who found a percentage of 88.2% (15 out of 17). Moreover, only 43 of the 248 (17.3%) single units in our study displayed a significant peak in the beta band, whereas in the study of Weinberger et al. [223] this was the case in 58 of the 200 (28%) single/multi-units.

4.4.4 Coherence in other frequency bands

The percentage of neuron pairs with significant coherence (60.7%) recorded from one micro-electrode (local) and the percentage of neuron pairs with significant coherence (51.0%) recorded from two separate micro-electrodes (global) is comparable. This indicates that the functional connectivity within the STN may spread out over distances of several millimeters. This is consistent with the results of Amtage et al. [6] who have also demonstrated significant interneuronal tremor coherence across such distances. Amtage et al. [6] have observed also a high amount of partial coherence and conclude that the STN tremor network is widely extended and strongly coupled. We could not perform a partial coherence analysis, as a consequence of our strict selection criteria for spike trains. Therefore, we had only a few recordings

that consisted of three simultaneously recorded neurons, which was not enough to come to any statistical significant conclusion. A high level of partial coherence may exclude a sparsely connected network, however, it does not differentiate between a network that is densely connected or has a small world architecture [37, 222]. In a small world network, in contrast to a densely connected network, the number of neurons with widespread connections and/or large number of connections is small. 'Long range' neurons in a small world network serve as common input to many neurons. Finally, the amount of coherence and partial coherence cannot rule out that the significant coherence between two STN neurons is the result of a common input from another brain region much further away located, for example, via the hyperdirect pathway from the cortex to the STN.

4.4.5 *Firing behavior*

Based on the discharge density histogram, the most frequently observed firing pattern within the whole STN was irregular (63%), followed by bursty (29%) and the regular (8%) discharge. This is in good agreement with a recent study by Seifried et al. [188]. Whereas in our study only with respect to the burst-like activity a statistically significant difference was found between sensorimotor part and elsewhere, for Seifried et al. [188] this was the case for regular and irregular activity. On the other hand, they did not find a significant difference in the firing rate, AI and CV of the ISI-distribution between the three STN subdivisions, whereas we did for our two STN subdivisions. This may be caused by the different approach in firing pattern classification, however, a more likely possibility for the difference is that we subdivide the STN in two regions based on the functional territories of the STN, while Seifried et al. [188] subdivide the STN in three regions along the stereotactic z-axis. A lower firing rate in the ventral STN was described in another report Rodriguez-Oroz et al. [178]. Our values for the firing rates and CV of the ISI-distributions are comparable to their values.

4.4.6 *The mechanisms underlying the pathological activity within the STN*

Experimental work using tissue slice preparations, animal models and in humans with PD has demonstrated that neurons in the basal ganglia (BG) tend to discharge in bursts, have altered firing rates and exhibit abnormally synchronized oscillatory

activity at multiple levels of the BG-cortical loop, see reviews by Hammond et al. [80] and Galvan and Wichmann [61]. However, the mechanisms underlying the pathological activity in PD are still debated. Using organotypic culture preparation with globus pallidus pars externa (GPe) and STN with frontomedial cortex and dorsolateral striatum, Plenz and Kital [170] conclude that the observed correlated activity in both STN and GPe is caused by the interaction between the STN and GPe rather than being driven by an external source. It is hypothesized that autonomous pacemaking in GPe neurons counterbalances the natural tendency of the reciprocally connected, STN–GPe network to switch into a pathological synchronous, rhythmic bursting seen in PD. Computational models show that increasing the inhibitory input to the GPe, due to dopamine depletion in the striatum, leads to a suppression of the autonomous GPe activity and therefore creates PD activity [114, 211]. In contrast, in vivo experiments give evidence that synchronized beta oscillations associated with the parkinsonian state are driven from motor areas of the cortex via the hyperdirect cortico-subthalamic pathway [128, 131, 189]. Recently, Ammari et al. [5] have shown in dopamine-depleted BG slices of mice that STN neurons, without synaptic inhibition from GPe, generate bursts of excitatory postsynaptic currents (EPSCs) in response to a single electrical stimulus. Such a burst of EPSCs leads to bursts of spikes in the STN. They hypothesize that the glutamatergic network within the STN, that is under negative control of dopamine, amplifies the STN responses to incoming excitation in the dopamine-depleted BG by generating bursts of spikes that will in turn generate bursts of spikes in GPe neurons.

Our results are largely confirmatory of those in other studies in that STN neurons of PD patients show coherent beta activity and burst-like activity. In addition, we demonstrated that this pathological activity was more a feature of the neurons in the sensorimotor STN than of the neurons in the remaining STN. However, with our available data and analysis we could not discover the source of the synchronized activity within the STN and resolve the mechanism behind the bursts in the STN.

4.4.7 Effect of false spike detection and clustering

As a consequence of the large number of false-negative errors, the true firing rate of neurons, which are classified as environmental with more than 10% of their spikes subthreshold, is underestimated and therefore the firing pattern may be classified incorrectly. The number of these neurons was equally distributed among the sensorimotor and remaining part of the STN (41% and 48%, respectively). Thus, the influence on the firing rate and firing pattern is comparable for both STN regions. When we leave out the environmental neurons we also obtain a significantly higher

firing rate and CV, a significantly lower AI and significantly more bursty neurons for the sensorimotor part (data not shown).

False negative and false positive errors in spike sorting may considerably influence the spike train measures related to synchrony, auto- and cross-correlation [10, 65, 165]. When spike sorting errors occur independently for two neurons under considerations, Pazienti and Grün [165] found that both types of error always reduce the significance of correlating firing. If two neurons are sorted from two different electrodes their spike sorting errors are independent, whereas their errors may also correlate when sorted from the same electrode. Correlated errors are created by ignoring overlapping spikes or by assigning spikes unjustly to another neuron (cluster overlap in the feature space). Removal of the overlapping spikes will remove information about functional connectivity between neurons. Moreover, inappropriate sorting of overlapping spikes may produce artefacts in the cross-correlograms and thereby introduce artificial correlations between pairs of neurons recorded from the same electrode [10]. Artificial correlations caused by removal of the overlapping spikes are diminished by assessing the statistical significance of the coherence with surrogate data that mimic the removal of the overlapping spikes. Pazienti and Grün [165] investigated the effect of incorrectly assigning spikes from one neuron to the other and found that this type of error may lead to false positive correlation between the two neurons involved. Therefore, we have excluded neurons from the analysis with a low quality of cluster separation and a large fraction of ISI violations.

4.5 Conclusions

Based on firing rate, discharge pattern of individual cells and the interneuronal coherence the sensorimotor part of the STN can be distinguished from the remaining part of the STN. The algorithm used to calculate the mentioned parameters are fast enough that they can be performed perioperatively during the evaluation phase of the MER. Ultimately, the firing behavior analysis of the recorded spike trains in the STN can be of extra help to the neurologist and neurosurgeon to determine particularly the sensorimotor part of the STN for the placement of the DBS electrode.

CHAPTER 5

A multi-site electrode system to measure local field potentials in a rat model of Parkinson's disease

5.1 Introduction

To obtain insight in differences in the dynamical behavior within nuclei of the basal ganglia under normal and Parkinsonian conditions, we studied a rat model of Parkinson's disease (PD). There are several animal models of PD, see Betarbet et al. [25], Bové et al. [30] for reviews. Since the loss of dopaminergic neurons within the substantia nigra pars compacta (SN_c) is a pathological hallmarks of PD and underlies the pathological dynamics of the basal ganglia [80], most animal models of PD using specific dopaminergic neurotoxins. At present, application of 1-methyl-4-phenyl-1,2,3,6-tetrahydropyridine (MPTP) neurotoxicity is the best available toxin-induced animal model of PD [186]. However, this model is not available for rat. We therefore used the 6-hydroxydopamine (6-OHDA) model. This neurotoxin disrupts the nigrostratial dopaminergic pathway when administered to the median forebrain bundle [25, 30, 49, 94, 100, 186] and thereby mimics the striatal dopamine deficiency observed in PD patients.

A multi-site electrode system was used that allowed us to record simultaneously local field potentials (LFP) in different nuclei of the basal ganglia, notably the caudate putamen, the globus pallidus pars externa (GPe), the globus pallidus pars interna (GPi), the subthalamic nucleus (STN), the SN_c and three other brain parts: the ventrolateral thalamic nucleus (VL), the primary motor cortex (M1) and the pedunculopontine nucleus (PPN).

The STN–GPe network acts as the pacemaker of the basal ganglia. Its pathological behavior in PD has been studied in computational models [181, 211]. The PPN modulates the STN and also connects to the brainstem. It is used as a target for electrical stimulation [97, 169], and its role in a network simulation model has been investigated [124]. The fundamental problem with computational studies is the lack of knowledge about the many physiological parameters involved. Having available

information on the network behavior may help to tune network models [136]. Especially important is to know how electrical activity in the different part of the basal ganglia is altered from a normal state to a PD state.

The electrode system was physically implemented in the form of a prefabricated teflon block. Isolated electrode wires were inserted through thin holes, that were based on the desired positions in the brains on the teflon block, glued and cut at the appropriate length. A canula was placed in a hole to administer the toxin. In this way we were able to record in up to 8 different brain locations of freely moving rats both in a normal and a PD state.

5.2 Methods

5.2.1 Subject

We used 12 male rats (Wistar Unilever, Harlan, The Netherlands), which were 3 months old and weighted 400–450 g at the time of surgery. Prior to surgery the rats were housed in pairs (High Makrolon® cages with Enviro Dry® bedding material and cage enrichment) with free access to food and water and were kept at a reversed 12–12 h light-dark cycle (light off at 8:30 AM). After surgery the rats were housed individually in order to prevent the rats from chewing on each other measurement system. All experimental protocols were authorized by the Ethical Committee on Animal Experimentation of the Radboud University Nijmegen (RU-DEC). Efforts were done to keep the discomfort of the animals as minimal as possible.

5.2.2 Construction of an electrode system suited for multi-site LFP recordings

A self-constructed electrode system was manufactured for multi-site local field potential recordings at specified brain locations [126, 217]. It consisted of a 8.5 mm $\times$ 4 mm, 3 mm thick Teflon block, which contained small holes located at the relative anterior/posterior (A/P) and medial/lateral (M/L) coordinates of the electrode target structures as determined by the rat-brain atlas of Paxinos and Watson [164]. In addition, it contained a bigger hole located at the relative A/P and M/L coordinates of the medial forebrain bundle for a stainless-steel guide cannula (diameter: 222 µm), used to inject 6-hydroxydopamine (6-OHDA). This block was fixed in a micro manipulator, which allowed us to insert electrode wires (stainless steel electrodes

insulated with polyamide, diameter: 127 µm, only the cutting edge of the electrode was not isolated) and the cannula through the holes and set them to their accurate depth coordinates. Wires and cannula were fixed to the Teflon-block by glue. The electrodes were fixed at the top-site to a connector pin which was entered into an electrode pedestal suitable for the connection to a multi-lead electrode cable. See Figure 5.1 for an overview of the construction of the multi-site recording system.

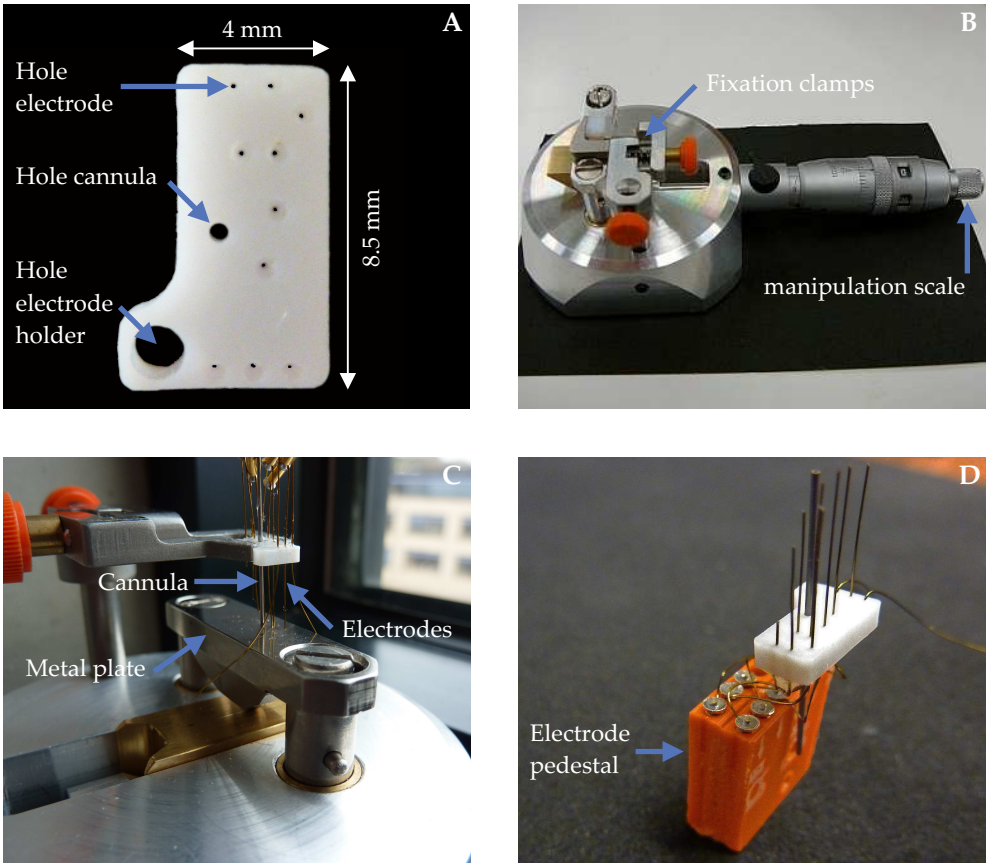

Figure 5.1 Parts and equipment used to manufacture the multi-site electrode system with cannula. It consists of a custom made Teflon block (**A**) with holes at the appropriate locations for the electrodes and the cannula. In the bottom left corner the block also has a bigger hole for the insertion of an electrode holder. This is needed during the implantation procedure for thorough placement of the system on the skull. The block is fixed with clamps in a micro manipulator (**B**,**C**) to assist in the insertion of the electrodes and the cannula through the holes. By turning on the manipulation scale, the distance between the Teflon block and a stable metal plate can be adjusted to set each electrode and the cannula to its desired length. Finally, electrodes are entered into an electrode pedestal (**D**) suitable for the connection to a multi-lead electrode cable.

5.2.3 Surgery

The multi-site electrode system with guide cannula was implanted stereotactically under isoflurane anesthesia. The head of the rat was fixed in the stereotactic instrument in such a way that we obtained a flat skull position between lambda and bregma. At the start of surgery, rats received a subcutaneous injection of the analgesic Rimadyl® mix (1:5 Rimadyl:NaCl, 0.4 ml/kg) and an intramuscular injection of atropine (0.1 ml) to prevent excessive salivary production. Body temperature was controlled and conserved via a heating pad. The local anesthetic Lidocaine was used on the incision points. Holes were drilled into the skull on top of the right hemisphere for the insertion of electrode wires and cannula, see Table 5.1 for the positions. In addition, two holes were drilled behind lambda for the insertion of ground and reference electrode. Four holes were drilled for the placement of screws (undetermined coordinates), that served as anchors for the cement in the fixation step. Electrode wires and cannula, fixed in the Teflon block at the appropriate position and length, were simultaneously entered into the brain. Ground and reference electrodes were placed on top of the cerebellum. The system was fixed to the skull via dental acrylic cement (Dental Union, Groningen, The Netherlands), that adheres to the screws and system. A dummy electrode was inserted in the cannula to prevent clogging (Figure 5.2). Postoperative analgesic Rimadyl® (24 and 48 h after surgery) was administered and rats were allowed to recover for 2 weeks.

Table 5.1 Stereotactic coordinates in mm of the electrode target structures and the end point of the cannula. All coordinates were determined relative to Bregma according to the rat-brain atlas of Paxinos and Watson [164].

	A/P	M/L	Depth
Primary motor cortex	−0.5	−1.5	1.5
Caudate putamen	−0.5	−3.0	6
Globus pallidus pars externa	−1.2	−3.3	7.8
Globus pallidus pars interna	−2.1	−2.6	8.7
Ventrolateral thalamic nucleus	−2.1	−1.7	7.1
Subthalamic nucleus	−3.6	−2.6	8.9
Substantia nigra pars compacta	−4.8	−2.3	8.7
Pedunculopontine nucleus	−7.2	−2.0	8.1
Cannula	−4.0	−1.5	8.5

Abbreviations: A/L, anterior/posterior; M/L, medial/lateral

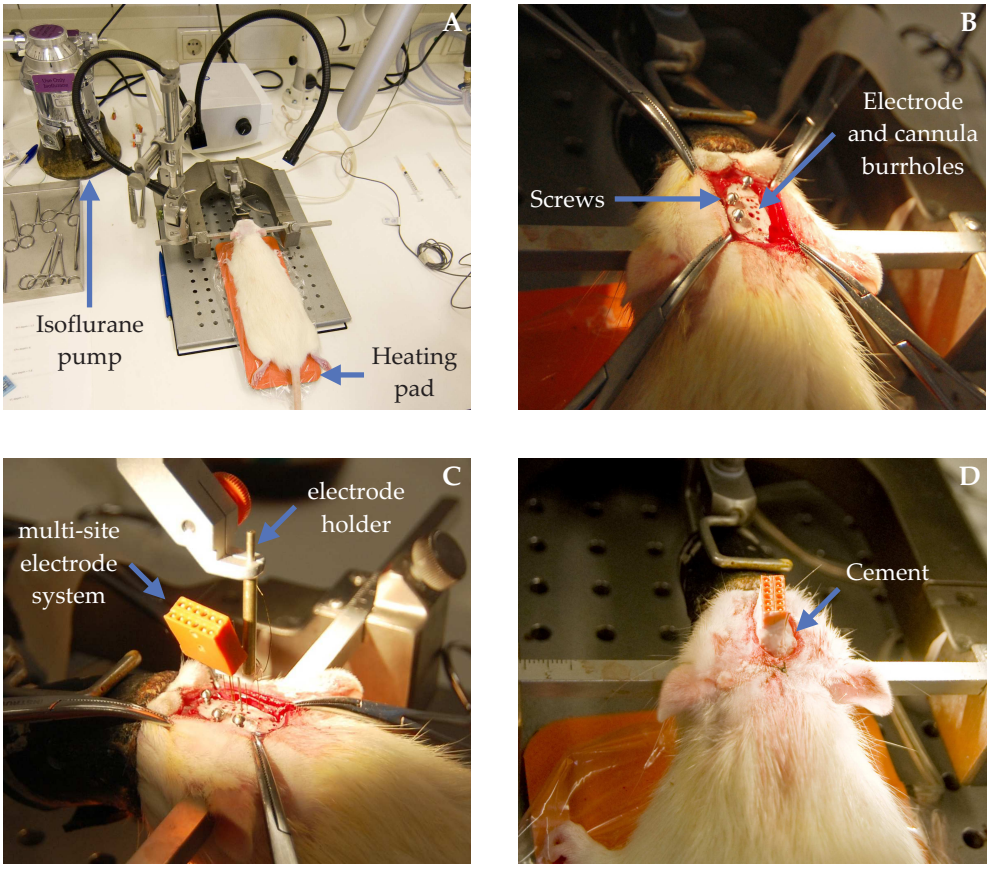

Figure 5.2 The rat is fixed in a stereotactic frame (**A**) and receives isoflurane anesthesia via a mask. The rat is placed on a heating pad to control and conserve the body temperature. Small burrholes are made in the skull above the intended recording sites and a bigger one above the medial forebrain bundle (**B**). In addition, screws are placed, which later help to fixate the whole system to the scull. The multi-site electrode system is connected to the stereotactic arm with an electrode holder (**C**) to assist in lowering it into the brain. Dental cement is used to fixate the whole sysem to the rats head (**D**).

5.2.4 Unilateral lesion of the nigrostriatal pathway

Three weeks after surgery the rats were given a unilateral injection of 6-OHDA to destroy the dopaminergic nigrostriatal pathway. The neurotoxin 6-OHDA (6-hydroxydopamine hydrobromide with 0.01% ascorbic acid; Sigma, Zwijndrecht, The Netherlands) is highly light-sensitive, and therefore was dissolved immediately before use in Ringer to a final concentration of 3 µg/µl and covered with aluminium foil. Then, 4 µl of 6-OHDA solution was infused at a rate of 1 µl/min through the implanted guide cannula using an injection needle connected by a flexible plastic

tube to a Hamilton syringe and inserted 0.5 mm beyond the tip of the cannula to target the medial forebrain bundle. The infusion rate was controlled manually by fixing the syringe into a mechanic holder and setting its piston into motion by turning the holder-screw. The tube was filled with distilled water and afterwards the 6-OHDA solution was inflated into the tip of the needle. The needle remained at the target site for 10 min after the infusion was completed to ensure diffusion of the 6-OHDA into medial forebrain bundle. The rats received an intraperitoneal injection of 25 mg/kg desipramine (Sigma, Zwijndrecht, The Netherlands), 30 minutes prior to the 6-OHDA infusion to protect noradrenergic neurons.

5.2.5 Recording of local field potentials

Two weeks after surgery (pre-lesion) and four weeks after 6-OHDA lesion LFPs were derived from the rats under two conditions: freely moving and on a moving belt. For the free moving condition the rats were placed individually in a transparent Plexiglas recording cage ($l \times w \times h = 25 \times 20 \times 35$ cm), filled with some bedding material and placed in a Faraday cage. The rats were connected to recording leads for multichannel LFP recordings attached to a swivel-contact, which allowed the registration of LFPs in freely moving animals. The LFP signals were amplified with a physiological amplifier (TD 90087, Radboud University Nijmegen, Electronic Research Group), filtered with an analog band pass filter of 1 to 100 Hz, and digitalized with a constant sample rate of 2048 Hz using the WINDAQ acquisition system (DATAQ Instruments Inc., Akron, OH, USA). In addition to the LFP signals the movements of the rat were registered by means of a Passive Infrared Registration (PIR) system (RK2000DPC LuNAR PR, Rokonet RISCO Group), that was attached to the ceiling of the recording cage. The rats were placed in the registration box and connected to the swivel-contact, 1 hour prior to the actual recordings in order to habituate to the recording conditions. Each rat was recorded for a period of 2 hours during the dark phase. The rest state of the rat was assessed with the following inequality:

$$|x(t)_{\mathrm{PIR}} - E\{x(t)_{\mathrm{PIR}}\}| \leq \sigma\{x(t)_{\mathrm{PIR}}\}; \tag{5.1}$$

were $x(t)_{\mathrm{PIR}}$ is the PIR signal. $E\{\}$ and $\sigma\{\}$ denote the expected value operator and the standard deviation operator, respectively. We considered the rat at rest if the inequality holds for $x(t)_{\mathrm{PIR}}$ on a continuous time interval longer than 3 minutes.

For the moving belt condition we used a special Plexiglas recording cage ($l \times w \times h = 26 \times 10 \times 35$ cm) whose floor was a rubber belt driven by two electrical power drives that were fed by an external feeding [187]. The rats were placed individually

in this recording cage on the rubber belt, which was also placed in the Faraday cage. The LFP leads were reconnected to a swivel-contact to guarantee free movements. The LFP data were obtained in the same way as under the free moving condition, except that we used a 50 Hz Notch filter to reduce the noise produced by the power drives of the moving belt. In addition to the LFP recordings, the rats were videotaped from a lateral view while they walked on the moving belt. All rats were trained until they were able to run steadily on the moving belt prior to the actual recordings. To minimize the discomfort of the animals, the moving belt recordings were performed directly after the freely moving recordings so that the animal could remain connected to the LFP leads. First, a rat had 3 min to adapt to the recording condition (speed zero). Next, the belt was turned on and set to a low running but challenging speed for 3 min, followed by a higher running speed for 3 min. The two moving belt speeds were separated by a 1 min rest period (speed zero). To enable later synchronization of the video and LFP recordings, a time marker equipment was used, including a digital stopwatch, which was placed directly in the picture frame of the camera, and a standard button box, whose square-wave signal was recorded in an extra channel of the WINDAQ system. During the experiment, square-wave markers were set at the beginning and the ending of each moving belt speed. Only LFP recording segments where the animal walked smoothly, continuously, and regularly were used.

5.2.6 Behavioral tests

Behavioral test were used to relate the extent of the unilaterally 6-OHDA lesion to the PD-like symptoms. The behavioral were performed two weeks after surgery (prelesion) and four weeks after 6-OHDA administration in the following sequence: 1) adjusting steps test; 2) rotarod test; 3) open field test; 4) apomorphine induced locomotion. For half of the rats, the LFP recordings and moving belt were performed prior the behavioral test and for the other half between the open field test and the apomorphine induced locomotion.

Adjusting steps test

To assess rigidity we performed the adjusting steps test as described by Lindner et al. [123]. In short, the rat was gently pushed laterally (left and right) over a distance of 100 cm at approximately 20 cm/s on a smooth stainless-steel table by placing one hand next to the left or right side of the rat. The number of forelimb adjustment steps

with the forelimb on the side to which the rat was being moved was counted for both directions. The test was video-taped such that the forelimb was clearly visible so that counting afterwards could be done. The score for each direction was calculated as the mean of 2 trials.

Rotarod test

The rotarod test was used to assess the animals' motor performance and coordination [78, 180]. The rotarod consists of a motorized rotating rod, whose speed and acceleration can be controlled. Each rat was placed individually on the rod, perpendicular to the axis of rotation and with its head facing the direction of the rotation. Tests were done at 8, 12 and 16 rpm. Each rotation speed started at 8 rpm and was accelerated with 0.4 rpm/s to its final speed. Pre-surgery the animals were trained to walk on the rod at each speed. The length of time that each animal was able to stay on the rod at each rotation speed was measured and was limited to a maximum of 120 seconds (including acceleration time). Each rat was tested in three consecutive trials, with the best time for each speed taken for data analysis. Test was performed in a room with dimmed light.

Open field test

The open field test was used to examine the locomotion activity and exploratory behavior in a novel and unfamiliar environment [45, 218, 221]. The open field consisted of an open square box (100 $\times$ 100 cm; 40 cm height) with black walls and floor and was illuminated at 110–130 lx light intensity. Immediately after an animal was placed individually in the center of the open field, its behavior was recorded for one hour using a installed camera above the center of the field and the Ethovision tracking software (Ethovision, Noldus Information Technology, Wageningen, The Netherlands). The following behavioral parameters were registered: total traveling distance in the first 10 min as a measure for locomotion and the time spent in the 36 $\times$ 36 cm imaginary center square of the field as a measure of fear. After testing each animal, the floor of the open field was thoroughly cleaned with an ethanol solution and water.

Apomorphine induced locomotion

The number of rotations in the direction of the lesion in response to apomorphine reflects the severity of unilaterally dopamine depletion caused by 6-OHDA and

subsequent development of dopamine receptor super-sensitivity Ungerstedt and Arbuthnott [214]. Apomorphine-induced rotation was measured after subcutaneous injection of 0.5 mg/kg apomorphine ((R)-(-)-apomorphine hydrochloride; Tocris) on two sites on the neck. Ten minutes after injection, the animal was placed individually in a round black bucket (diameter $\approx$ 30 cm), and its rotation behavior was recorded for 40 minutes using an installed camera above the center of the bucket. Afterwards, full 360°contralateral turns (away from the side of the lesion (cl)) and ipsilateral turns (toward the side of the lesion (il)) from an arbitrary chosen landmark were counted. According to van Oosten and Cools [218], the turning drive, $R_{\text{drive}} = \text{cl} + \text{il}$, and the turning direction preference, $R_{\text{pref}} = 100(\text{cl} - \text{il})/R_{\text{drive}}$, were computed.

5.2.7 *Post-mortem verification of electrode site*

After the experiment was completed, brains were removed for histological verification of the electrode locations. Rats were deeply anesthetized by intraperitoneal injection of a high dose of sodium pentobarbital (Nembutal). Subsequently, small electrolytic lesions were made at the tip of the recording electrode by passing an anodal direct current of 25 µA through the electrode for several seconds (10–20 s). Once lesion are set, the animals were perfused intracardially with physiological saline followed by a solution of 2% potassium ferrocyanide dissolved in 4% paraformaldehyde phosphate-buffer. The iron deposits left at the electrode tip after the electrolytic lesioning reacts with the potassium ferrocyanide to form a blue dot, clearly marking the electrode tip. Next, the brains were removed and stored in 4% paraformaldehyde phosphate-buffer for 24 hours and transferred into 30% buffered sucrose where they remained until they had sunk to the bottom. Brains were cut in 40 µm coronal slices with a microtome and slices containing the blue dots of the electrode tips are stained with Cresyl Violet.

5.3 Results

5.3.1 *Drop-out rates*

At different stages of the experiment rats were dropped out from the study. Firstly, three rats died due to surgery. Although, implanting the multi-site electrode system into the brain could lead to death due to brain injury (hemorrhage), the three rats died before insertion of the system. Secondly, two animals probably died due to the

6-OHDA injection. Bilateral infusion of 6-OHDA in the MFB is commonly associated with severe impairments in drinking and feeding, resulting in a high mortality rate of animals. However, all animals showed decrease in body weight after the unilateral 6-OHDA injection. Finally, two rats lost their electrode system. Therefore 7 out of 12 rats were dropped out, leaving a total number of 5 rats.

5.3.2 *Electrode Positioning*

The brains of the five rats that fulfilled the experiment were subjected to histology. Although one animal lost its electrode system during the last experimental day, verification of the electrode locations was possible as the electrode shaft and tip were visible on the brain slices. The histological outcome for each rat is shown in Table 5.2. In total we placed 40 electrodes in the five animals from which 14 (35%) were successfully placed in the planned target structure and 3 (7.5%) at the boundary. Especially, electrodes for the small structures were misplaced. For our purpose to investigate the functional connectivity between the different nuclei the number of correctly placed electrodes per rat should be at least two. In one case we did not fulfill this requirement.

Table 5.2 Histological verification of the electrode locations

Rat	M1	CPu	GPe	GPi	VL	STN	SN_c	PPN
1	−	+	−	−	−	−	+	⋆
3	−	+	−	−	−	−	−	−
4[1]	+	+	+	−	+	−	+	−
7	+	⋆	+	−	−	−	−	−
9	+	+	⋆	+	−	⋆	−	−

The +, − and ⋆ marker indicates if the electrode tip was inside, outside or at the border of the target structure,respectively. *Abbreviations*: M1, primary motor cortex; CPu, caudate putamen; GPe, globus pallidus pars externa; GPi, globus pallidus pars interna; VL, Ventrolateral thalamic nucleus; STN, Subthalamic nucleus; SN_c, Substantia nigra pars compacta; PPN, Pedunculopontine nucleus.
[1] Verifications are performed without electrolytic lesions at the electrode tips.

5.3.3 *Behavioral test*

The high preference percentage to rotate to the contralateral direction and the high turning drive in rats 4, 7 and 9 post-injection of 6-OHDA indicated successful

dopamine depletion (Figure 5.1A). Rats 4, and 7 pre-lesion and rat 3 post-lesion had a preference to rotate to the contralateral, ipsilateral and contralateral direction, respectively, but their turning drive was low and therefore not suspicious. Only rats 4 and 7 showed a large reduction in locomotion after 6-OHDA injection, while all rats showed more fear to enter the center of the open field (Figure 5.1B). The time during which an animal could stay on the rotarod at 16 rpm was lower in all animals after 6-OHDA injection (Figure 5.1C). Except for rat 7, the number of adjustment steps after 6-OHDA injection were not significantly different between the contralateral and the ipsilateral forelimb , indicating that they did not suffer from rigidity.

5.3.4 Local field potentials

Figure 5.4 and 5.5 show the LFP recordings of a rat at rest and running on a moving belt, respectively. In both situation we were able to derive good signals from the implanted electrodes. The quality of the signals was comparable between pre-lesion and post-lesion. Thus, the signals did not deteriorate over time due to tissue formation around the electrode tips. Interestingly, the amplitude of the LFP signals decreases during moving belt as compared to rest situation.

5.4 Discussion

In this Chapter we described the development of a multi-site electrode system to simultaneously measure the local field potential in different brain structures relevant for Parkinson's disease in freely moving rats. We have shown that we can successfully record from the electrodes (good signal-to-noise ratio) when the rat is at rest or is running on a moving belt, even seven weeks after system implantation. Moreover, we were able to render the animals parkinsonian with unilateral medial forebrain bundle 6-OHDA infusions via the implanted cannula. This set-up allowed us to investigate the change in the functional connectivity between different nuclei from normal to PD state in the same animal at rest or during forced exercise.

The analysis of the interaction and the the cooperativity (functional connectivity) between the different nuclei in normal and PD state can be done by using measures of association such as correlations or coherences among recording sites. However, in our set-up the LFPs recorded at the different recording sites were all amplified with respect to the same common reference. This introduces a signal common to all channels and depending on its amplitude it can dominate the coherence estimate [55]. One way to overcome this problem is to use two electrodes in each structure

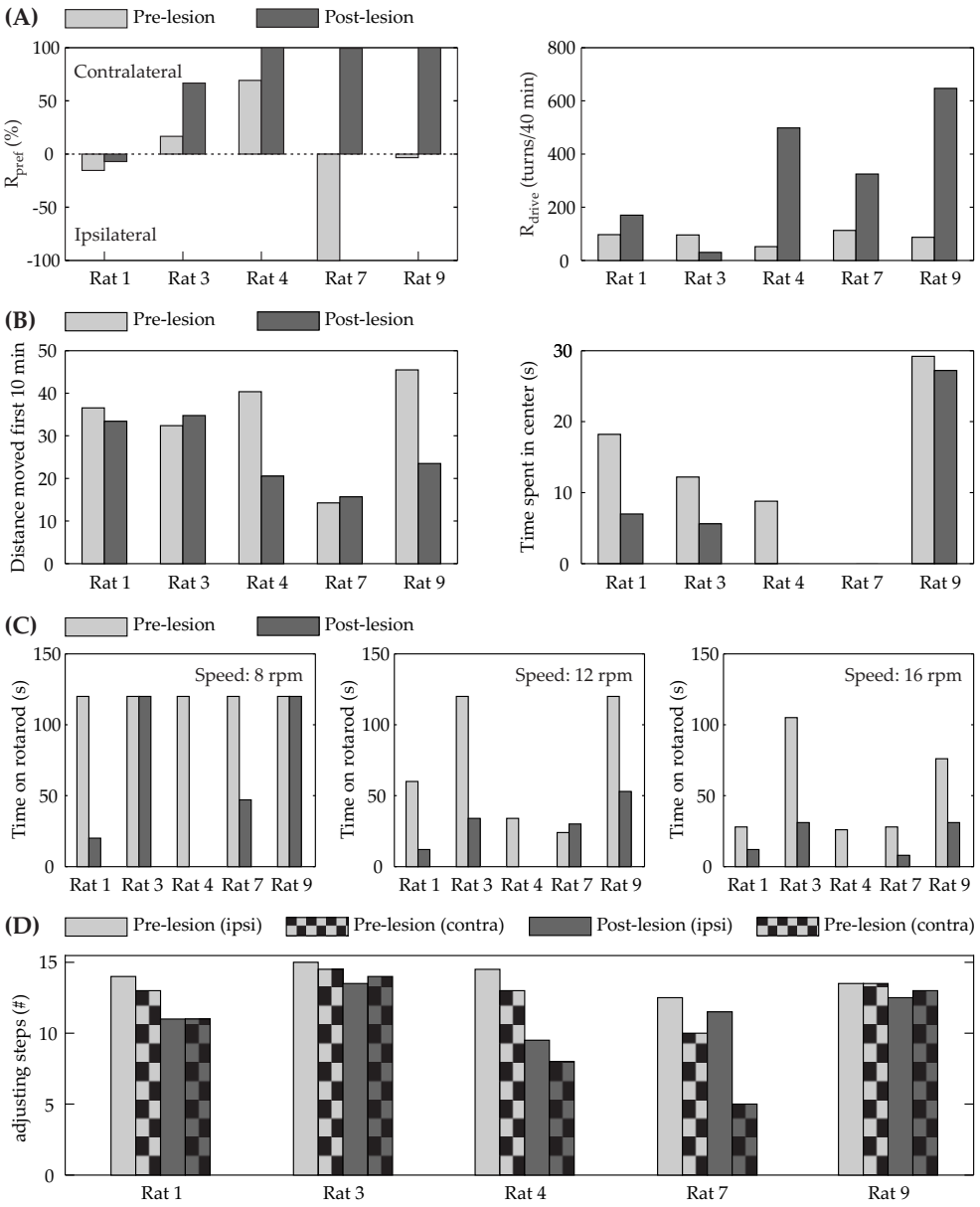

Figure 5.3 To examine the severity of unilaterally dopamine depletion the apomorphine induced locomotion test (**A**) is performed. To relate the extent of the 6-OHDA lesion to the PD-like symptoms the open field test (**B**), rotarod test (**C**) and adjusting steps test (**D**) are performed.

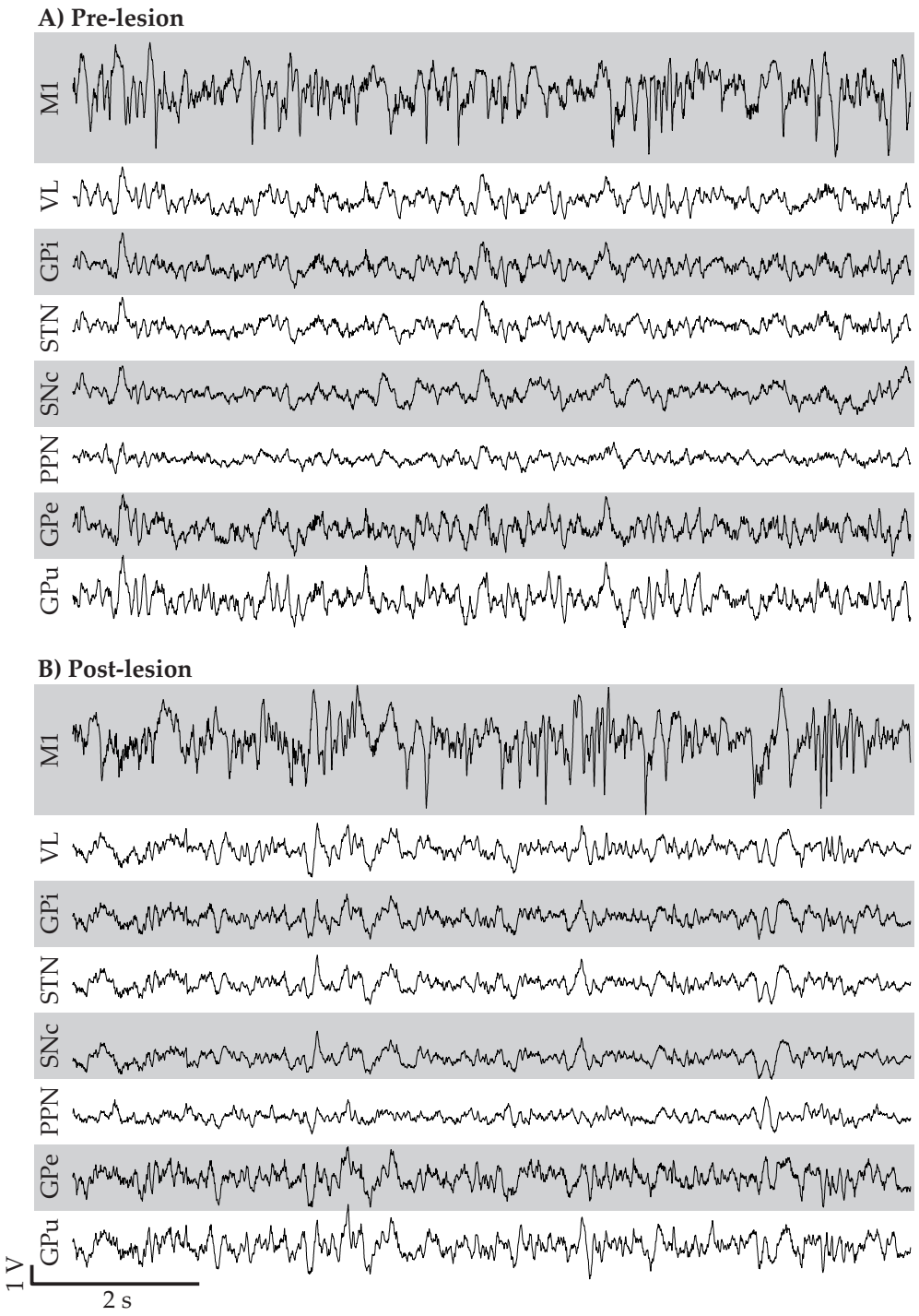

Figure 5.4 Example of 10-s long simultaneously recorded LFP set of rat 9 at rest, before (**A**) and after (**B**) the 6-OHDA lesion. The abbreviation of the nuclei names next to the LFPs are the intended nuclei, see Table 5.2 if they are placed correctly.

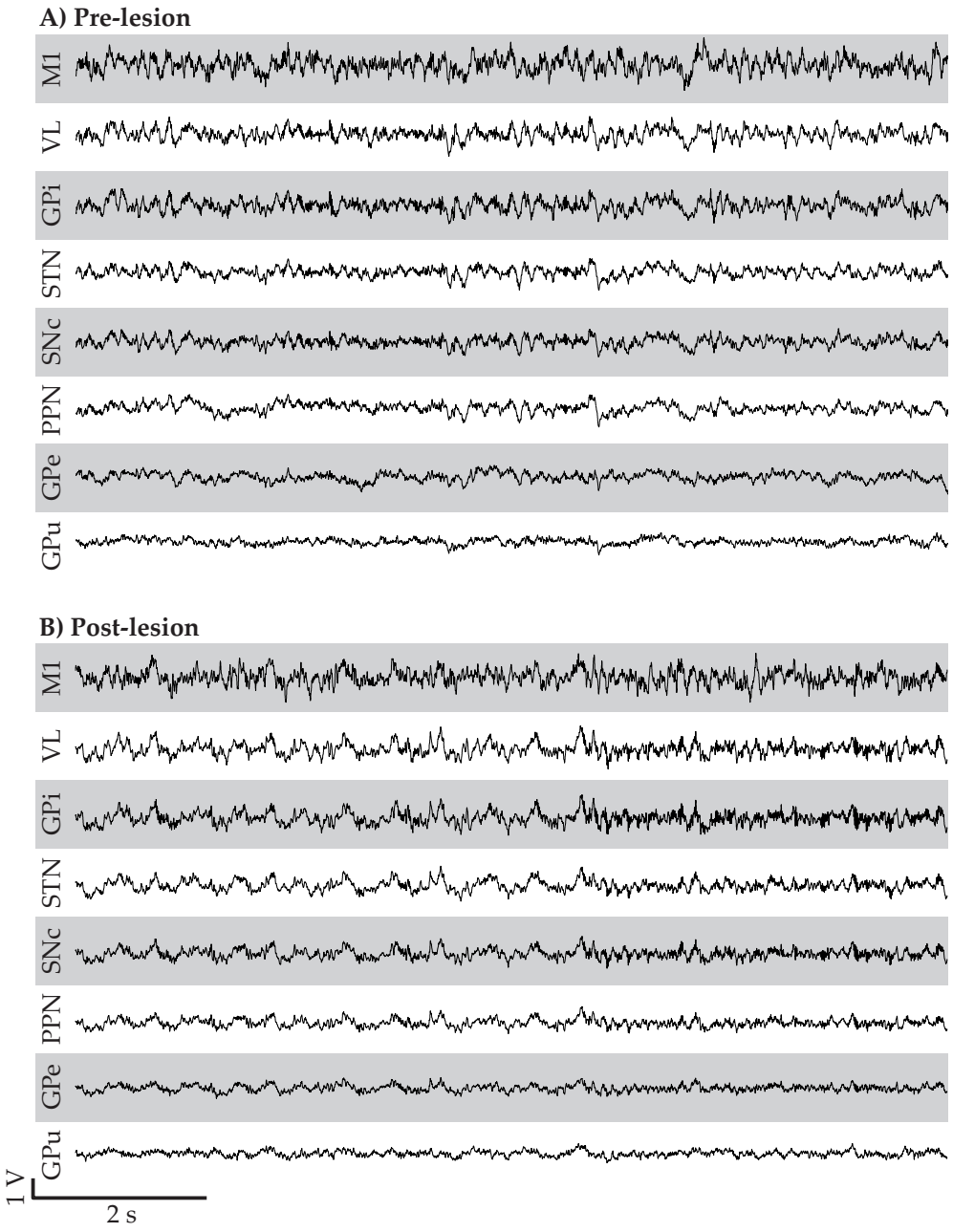

Figure 5.5 Example of 10-s long simultaneously recorded LFP set of rat 9 running on the moving belt at the highest speed, before (**A**) and after (**B**) the 6-OHDA lesion. The abbreviation of the nuclei names next to the LFPs are the intended nuclei, see Table 5.2 if they are placed correctly.

and off-line take the potential difference between the two electrodes (local bipolar derivation). This approach requires another larger electrode pedestal for the extra electrodes, which make the fixation to the skull difficult. In addition, all channels should be recorded with exactly the same amplification gain factor. However, due to tissue formations around the electrode its impedance is subjected to uncontrollable and continuous changes. Hence, the amplification gain is fluctuating and can differ across the channels. Another way is to use a connectivity measure that is less affected by a common signal originating from the same reference. Granger causality is a linear directional measure of connectivity and has been successfully applied to LFP data from animals [22, 184]. The Granger causality analysis is based on a multivariate autoregressive modelling of LFP time series [22]. In this approach the instantaneous component of the interactions, which is mainly affected by the common signal, can be discarded [22, 184].

Generally speaking, it is assumed that LFP reflects the incoming synaptic activity (excitatory and inhibitory postsynaptic potentials) [102, 141], while spikes reflect the output of the local network [59, 117]. However, other slow processes may contribute to the generation of LFPs, see Moran and Bar-Gad [143] and references therein. To use the observations of population level recordings (LFPs) to tune our spiking models we have to average spiking activity in one way or another.

Tan et al. [206] developed an electrode construction using clinical principles to perform DBS unilaterally or bilaterally in freely moving rats. They test their set-up in a rat model of PD (bilateral 6-OHDA infusion in the striatum) and a rat model of Huntington's disease (transgenic rats). The way they implanted and fixed the electrode system is quite similar to our multi-electrode system. It would be interesting to extend our system with their DBS-electrode, such that we could also measure the effect of DBS on network connectivity. Especially, for stimulation protocols where stimulation is not applied continuously, such as coordinated reset [208], it is worth seeing what happens with the network connectivity in the off-stimulation period. Tan et al. [206] achieved dopamine depletion (PD-model) by stereotactic injections of 6-OHDA into striatum. However, we have shown that dopamine depletion could also achieve by injection of 6-OHDA through the implanted guide cannula into the MFB. Thus, performing experiments with the same rat in different state (normal or PD) is possible.

A problem we encountered with our multi-site electrode is the high number of electrode misplacement. We could probably reduce this number by having multi-site electrode systems for different bregma-lambda distances at our disposal during surgery.

CHAPTER 6

Conclusions and Outlook

Deep brain stimulation (DBS), discovered by accident during thalamotomy to be effectively in reducing tremor, is now an established therapy of last resort for Parkinson's disease (PD). Currently, it is widely applied in the subthalamic nucleus (STN), the globus pallidus pars interna (GPi) and the ventral intermediate thalamic nucleus to alleviate PD symptoms. These targets were original selected for ablation. The selection was based on the classical model of the basal ganglia which explains the symptoms of PD in terms of changes in mean firing rate of the basal ganglia nuclei. Remarkably, DBS is continuously applied to these target nuclei and is only effective within very specific parameter ranges, most notably at high frequencies (>100 Hz). These parameter settings for DBS were empirically established.

Nowadays, we know that PD symptoms not only result from changes in firing rate of the basal ganglia nuclei, but also from abnormal synchronization of neuronal activity in basal ganglia networks. Moreover, not only the basal ganglia network is involved in PD and not all parts of a basal ganglia nucleus are affected. These new insights can be used to develop new and more effective stimulation protocols, and to select new nuclei or part of a nucleus to stimulate for the treatment of PD motor symptoms. For example, it turns out that STN–DBS is most effective if the active DBS electrode contact is located in the sensorimotor part. In Chapter 4, we make a valuable contribution to the growing evidence that synchronization between basal ganglia neurons in the beta frequency band (13–30 Hz) might serve to characterize the sensorimotor part of the STN.

To steer new stimulation therapies for PD, it is important to know in which circuitry and how the pathological activity is generated. However, the mechanisms underlying the pathological activity in PD are still debated and therefore the efforts in Parkinson's research are focused on investigating 'what goes wrong in the parkinsonian brain, and how can we reverse this pathological behavior'. Computational modeling is a valuable tool to shed light on the mechanisms underlying the pathological activity in PD and the working mechanism of DBS.

Modeling brain dynamics

The brain is too complicated to capture in a single model. Not only is the numbers of neurons too large, and do they make too many connections, in addition there are many timescales involved, which complicates even more. A model can only address a specific aspect of the dynamics of the brain. A good model is as simple as possible, relates to available data and allows to make statements about possible mechanisms. It is desirable that it makes predictions that can be verified experimentally.

Data driven modeling is nowadays the standard in neuroscience. There are many data available and this is helpful, as there are always so many parameters unknown. Yet, addressing specific questions requires specific data that very well may not be available. This has played a key role during my thesis work.

In this thesis, Parkinson's disease is the central theme. There are several issues that complicate the task for a mathematical modeler. There are many parts of the brain involved: not only the basal ganglia, but also the thalamus, the cortex and the brainstem. Despite much research done in the past, there are still many questions open about the anatomy of the basal ganglia. For instance, there is not very much knowledge about connectivity within the various nuclei. It is even unknown how neurons within the STN make connections. So the question arises:

Where do we start?

In 2002, Terman, Rubin, Yew and Wilson published a model for the subthalamopallidal network of the basal ganglia. It uses many physiological parameters, so indeed relates to available data, and based on this model hypotheses were made on the origin of synchronized bursting. This model, which they have extended in 2004 to a basal ganglia-thalamic network model [181], has been the starting point to investigate the effect of DBS in the pedunculopontine nucleus (PPN), chapter 3 of the thesis. It is proposed that low frequency stimulation of the PPN combined with standard DBS of the STN is clinically more effective for PD symptoms. We were able to model a single PPN Type I cell that reproduces firing pattern characteristics consistent with published experimental data. In our basal ganglia-PPN network model, combined stimulation of the PPN and STN is almost never better for the relay properties of the PPN cell than exclusive STN stimulation. However, with PPN stimulation alone it was possible to eliminate the clusters and thereby the low frequency (3 Hz, associated with tremor) oscillations from the entire network model. PPN–DBS is suggested for PD patients with severe gait and postural impairment. It is an open question how to relate these symptoms with network activity in computational models. It should be noted that the results of this study critically depend on the chosen topography

between the basal ganglia and the PPN and the strength of the connections. To continue in this direction requires more experimental findings about the input to this nucleus from the various nuclei in the basal ganglia.

This was exactly the reason why we have chosen to measure local field potentials (LFP) in a 6-hydroxydopamine rat model of PD. An account of this research is the fifth chapter of this thesis. It shows that it is possible to obtain clean LFP data. This study also showed that it is not easy to draw conclusions from the data that would improve the mathematical models. It would be better to work with neural mass models in combination with LFP data, than with the spiking neuron models like the ones used in chapter 3. In addition, the setup of the experiments should be slightly changed to make the outcome more suitable. For example, we should not use the same reference point for all electrodes, as this complicates the connectivity analysis. To reduce the number of electrode misplacements it would be wise to have multi-site electrode systems for different bregma-lambda distances.

LFP or single unit data?

In 2009, I have started to analyze unique human data, obtained in the Academic Medical Center, during DBS surgery in Parkinson patients. Chapter 4 of the thesis is devoted to the analysis of these data. Although there are many theoretical results in data analysis, in practice most of the assumptions underlying these, are not satisfied. We have combined many known strategies to arrive at conclusions that have practical value in the clinic. This in itself is satisfying. It was our initial goal to also use these data for the network models. Indeed these results are valuable. Based on spike data of single neurons it is possible to tune networks to represent certain aspects of the data, like the mean frequency, firing pattern and the coefficient of variation. We have also used data from GPi to test the standard DBS protocol. The results are in Meijer et al. [137] and are partially shown in the introduction of this thesis. The conclusion here is that single unit data are helpful when one works with network models. However, like always, it is *never enough*. Based on these data we cannot infer the network connectivity. There is always the problem that is it difficult, if not impossible, to distinguish between common input and causal connections. It may be clear that having both LFP and spike data at one's disposal is optimal. We foresee that in the future it will become fashionable to integrate spiking neuron models with neural mass models.

Making predictions

Since 2003, Peter Tass and his group advocate a new way of stimulation for PD. The so-called coordinated reset (CR) stimulation is supposed to be more effective than the standard continuous high frequency stimulation. Moreover, it saves battery consumption and it leads to fewer negative side effects of DBS, because most of the time the stimulation is turned off and stimulation intensity is low. In a model study we have investigated whether spike-timing-dependent plasticity (STDP) within the globus pallidus pars externa (GPe) might be an explanation for this claim. This is typically a situation where a computational model may be of help. We have determined a specific window for STDP for intra GPe connections, that does the job. The model predicts that with CR-stimulation it is possible to switch between different stable states of the system, one being pathological and the other resembling a more healthy state. What remains open is to confirm this window for STDP experimentally.

Where will it lead us from here?

Theory and experiment should go hand in hand. We have seen that experiments may rise questions that first can be examined in a theoretical computational study. From this computational study hypotheses should be put forward. This ideally will suggest experiments that either confirm or reject the hypotheses, likely raising more detailed questions that than will be subject for another computational study.

So far we discussed two type of models: spiking neuron models and neural mass models. There is evidence that we must also take into account the extracellular space and the astrocytes. In fact there are more astrocytes than neurons, and they play an important role in calcium signaling and the buffering of ions. But the principles for modeling and experiment as described above do not change.

APPENDIX A

STN and GPe cell model

In Chapter 2 we consider a GPe–STN network model in which each cell is represented as a single-compartment conductance-based model, based on voltage-clamp and current-clamp data of both populations [69, 181, 211]. Here we describe the equations and parameters of the membrane currents of equation 2.1 for both the STN and the GPe cell model. In both cell models, time is in ms, voltages are in mV, ion concentrations are in mM, currents are in μA cm^{-2}, conductances are in mS cm^{-2} and the membrane capacitance is in μF cm^{-2}. The membrane capacitance for each cell is assumed to be unity.

Membrane currents

In the STN and GPe cell model it is assumed that the instantaneous current-voltage relation for I_L, I_K, I_{Na}, I_T, I_{Ca} and I_{AHP} is linear. The leak current and the voltage-dependent currents (i.e. except I_{AHP}) are given by Hodgkin–Huxley formalism and are identical for both STN and GPe cells:

$$\begin{aligned} I_L(v) &= g_L(v - E_L) \\ I_{Na}(v) &= g_{Na} m_\infty^3(v) h (v - E_{Na}) \\ I_K(v) &= g_K n^4 (v - E_K) \\ I_{Ca}(v) &= g_{Ca} c_\infty^2(v)(v - E_{Ca}), \end{aligned}$$

except for I_T:

$$\begin{aligned} \text{STN} : I_T(v) &= g_T a_\infty^3(v) b_\infty^2(r)(v - E_{Ca}) \\ \text{GPe} : I_T(v) &= g_T a_\infty^3(v) r (v - E_{Ca}), \end{aligned}$$

where v is the membrane potential; m,h,n,a,b,r and c are (in)activation variables (gating variables); E_{L}, E_{Na}, E_{K} and E_{Ca} are the reversal potentials of the leak, sodium, potassium and calcium current, respectively; and g_{L}, g_{Na}, g_{K}, g_{T} and g_{Ca} are maximal conductance. The reversal potential is defined by the Nernst equation. We assume the ionic concentrations are constant during our simulations. The maximal conductances and reversal potentials for both population models are listed in Table A.1. The steady state of the gating variable (X_∞) depends on the voltages as follows

$$X_\infty(v) = \frac{1}{1+\exp(-(v-\theta_X)/q_X)} \qquad X \in \{m,h,n,r,a,c\}, \tag{A.1}$$

where θ_X and k_X are the half (in)activation voltage and slopes, respectively. For the T-current inactivation variable b, we used

$$b_\infty(r) = \frac{1}{1+\exp((r-\theta_b)/q_b)} - \frac{1}{1+\exp(-\theta_b/q_b)}. \tag{A.2}$$

Table A.1 Maximal conductances (g_x) and reversal potentials (E_x) of the membrane currents for STN and GPe models

	g_x [mS cm^{-2}]						E_x [mV]			
	L	K	Na	T	Ca	AHP	L	K	Na	Ca
STN	2.25	45	37.5	0.5	0.5	9	−60	−80	55	140
GPe	0.1	30	120	0.5	0.1	30	−55	−80	55	120

The gating variables h,n and r for both cell models are treated as slowly varying variables, whereas m,c,a and b for both cell models are treated as fast varying variables. For the slow variables we have first order kinetics of the form:

$$\frac{\mathrm{d}X}{\mathrm{d}t} = \phi_X(X_\infty(v) - X)/\tau_X(v) \qquad X \in \{h,n,r\}, \tag{A.3}$$

where ϕ_X is a time scaling constant of X. The voltage-dependent (in)activation time constant (τ_X) of X is given:

$$\tau_X = \tau_X^0 + \frac{\tau_X^1}{1+\exp(-(v-\theta_X^\tau)/q_X^\tau)} \qquad X \in \{h,n,r\}. \tag{A.4}$$

Time for (in)activation are then given by a sigmoidal function, with τ_X^0/ϕ_X as the minimum, $(\tau_X^0+\tau_X^1)/\phi_X$ as the maximum, θ_X^τ the voltage at which the time constant

is midway between the maximum and minimum values, and σ_X^τ is the slope factor which determines the level of voltage-dependence of the time constant. For the fast variables, activation are taken instantaneous and are determined by equation A.1 and in the case for b by equation A.2. The parameter values used for the gating kinetics of the ionic channels of the STN and GPe models are given in Tables A.2 and A.3.

Table A.2 STN kinetic parameters

	θ_X	q_X	τ_X^0	τ_X^1	θ_X^τ	q_X^τ	ϕ_X
m	−30	15					
h	−39	−3.1	1	500	−57	−3	0.75
n	−32	8	1	100	−80	−26	0.75
r	−67	−2	7.1	17.5	68	−2.2	0.5
a	−63	7.8					
b	0.25	−0.07					
c	−39	8					

Table A.3 GPe kinetic parameters

	θ_X	q_X	τ_X^0	τ_X^1	θ_X^τ	q_X^τ	ϕ_X
m	−37	10					
h	−58	−12	0.05	0.27	−40	−12	0.05
n	−50	14	0.05	0.27	−40	−12	0.1
r	−70	−2	30	0			1
a	−57	2					
c	−35	2					

The afterhyperpolarization potassium current (I_{AHP}) also depends on the calcium concentration instead of membrane potential and is given by:

$$I_{\text{AHP}} = g_{\text{AHP}}(v - E_{\text{K}})([Ca]/([Ca] + k_1)), \tag{A.5}$$

where g_{AHP} is the maximal conductance and is given in Table A.1. The constant k_1 is the dissociation constant of the calcium-dependent afterhyperpolarization potassium current and is given in Table A.4.

Calcium dynamics

The intracellular concentration of calcium ions (Ca^{2+}) available for the I_{AHP} depends on the calcium currents (I_T and I_{Ca}) and is governed by the first-order differential equation:

$$\frac{d[Ca]}{dt} = \epsilon_{Ca}(-I_{Ca} - I_T - k_{Ca}[Ca]), \tag{A.6}$$

where ϵ_{Ca} is a constant that accounts for the effects of cell volume, buffers, and molar charge of calcium. The constant k_{Ca} is the calcium pump rate. The constants for the calcium dynamics for the STN and GPe models are given in Table A.4. Note that the calcium reversal potential, that is used in the equations for I_T and I_{Ca}, is not affected by the calcium dynamics.

Table A.4 Calcium dynamic parameters

	ϵ_{Ca}	k_{Ca}	k_1
STN	5e−5	22.5	15
GPe	1e−4	15	30

APPENDIX B

The ionic current equations for the PPN model

We assume that the instantaneous current-voltage relation for $I_{\mathrm{Na,L}}$, $I_{\mathrm{K,L}}$, I_{Na}, I_{K}, I_{h} and $I_{\mathrm{Na,p}}$ is linear. These currents have the following general form:

$$I_{\mathrm{ion}} = g_{\max} m^a h^b (V_{\mathrm{m}} - E_{\mathrm{ion}}) \qquad a, b \in \mathbb{N}_0, \tag{B.1}$$

where $g_{\max}$ is the maximum ion channel conductance, m is the activation gating variable, h is the inactivation gating variable, V_{m} is the membrane potential and E_{ion} is the reversal potential. The reversal potential is defined by the Nernst equation. We assume the ionic concentrations are constant during our simulations. The current-voltage relation for I_{T} has a non-linear dependence upon ionic driving force that is described by the Goldman–Hodgkin–Katz current equation ($G(V_{\mathrm{m}}, [\mathrm{ion}]_i, [\mathrm{ion}]_o)$). Thus,

$$\begin{aligned} &I_{\mathrm{T}} = m^2 h G(V_{\mathrm{m}}, [\mathrm{Ca}]_i, [\mathrm{Ca}]_o) \\ &\text{with} \\ &G(V_{\mathrm{m}}, [\mathrm{Ca}]_i, [\mathrm{Ca}]_o) = p_{\mathrm{Ca}} \frac{z^2 F^2 V_{\mathrm{m}}}{RT} \frac{[\mathrm{Ca}]_i - [\mathrm{Ca}]_o \exp(-\frac{zFV_{\mathrm{m}}}{RT})}{1 - \exp(-\frac{zFV_{\mathrm{m}}}{RT})}, \end{aligned} \tag{B.2}$$

where $p_{\mathrm{Ca}} = 10^{-4}$ cm s^{-1} is the maximum T-type calcium channel permeability, $z = 2$ is the valence of calcium ion, F is the Faraday's constant in J V^{-1} mol^{-1}, R is the gas constant in J K^{-1} mol^{-1}, $T = 309.15$ K is the absolute temperature, $[\mathrm{Ca}]_o = 2$ mM is the extracellular Ca^{2+} concentration of the model cell. Intracellular Ca^{2+} concentration ($[\mathrm{Ca}]_i$) depends on T-type calcium current and is given by the following equation

$$\frac{\mathrm{d}[\mathrm{Ca}]_i}{\mathrm{d}t} = \frac{[\mathrm{Ca}]_{\mathrm{buff}} - [\mathrm{Ca}]_i}{\tau_{\mathrm{Ca}}} - k_{\mathrm{Ca}} I_{\mathrm{T}},$$

where $[\mathrm{Ca}]_{\mathrm{buff}} = 0.00024$ mM, $\tau_{\mathrm{Ca}} = 5$ ms, $k_{\mathrm{Ca}} = 5.1821\mathrm{e}{-5}$ is a unit conversion factor.

The (in)activation gating variables in equation B.1 and B.2 are described by differential equations of the form:

$$\frac{\mathrm{d}X}{\mathrm{d}t} = (X_\infty(V_\mathrm{m}) - X)/\tau_X(V_\mathrm{m}) \qquad X \in m,h,$$

where $X_\infty(V_\mathrm{m}) = \alpha_X(V_\mathrm{m})/(\alpha_X(V_\mathrm{m}) + \beta_X(V_\mathrm{m}))$ is the steady-state voltage-dependent (in)activation function of X and $\tau_X(V_\mathrm{m}) = 1/(\alpha_X(V_\mathrm{m}) + \beta_X(V_\mathrm{m}))$ is the voltage-dependent time constant. These functions are based on neurophysiological data of the thalamocortical relay neuron [48, 88, 135], except for the persistent sodium gating variables which are based neurophysiological data of the pre-Bötzinger neuron [182, 183].

Sodium and potassium leak currents

$$I_\mathrm{Na,L} = g_\mathrm{Na,L}(V_\mathrm{m} - E_\mathrm{Na})$$
$$I_\mathrm{K,L} = g_\mathrm{K,L}(V_\mathrm{m} - E_\mathrm{K})$$

Sodium current

$$I_\mathrm{Na} = g_\mathrm{Na} m^3 h (V_\mathrm{m} - E_\mathrm{Na})$$
$$\alpha_m = 0.32(V_\mathrm{m} + 55)/(1 - \exp(-(V_\mathrm{m} + 55)/4))$$
$$\beta_m = -0.28(V_\mathrm{m} + 28)/(1 - \exp((V + 28)/5))$$
$$\alpha_h = 0.12\exp(-(V_\mathrm{m} + 51)/18)$$
$$\beta_h = 4/(1 + \exp(-(V_\mathrm{m} + 28)/5))$$

Potassium current

$$I_\mathrm{K} = g_\mathrm{K} m^4 (V_\mathrm{m} - E_\mathrm{K})$$
$$\alpha_m = 0.032(V_\mathrm{m} + 63.8)/(1 - \exp(-(V_\mathrm{m} + 63.8)/5))$$
$$\beta_m = 0.5(\exp(-(V_\mathrm{m} + 68.8)/40))$$

Hyperpolarization-activated current

$$I_\mathrm{hyp} = g_\mathrm{hyp} m^3 (V_\mathrm{m} - E_\mathrm{hyp})$$
$$m_\infty = 1/(1 + \exp((V_\mathrm{m} + 85)/5.5))$$
$$\tau_m = 1/(\exp(-15.45 - 0.086 V_\mathrm{m}) + \exp(-1.17 + 0.0701 V_\mathrm{m}))$$

Persistent sodium current

$$
\begin{aligned}
I_{\mathrm{Na,p}} &= g_{\mathrm{Na,p}} mh(V_{\mathrm{m}} - E_{\mathrm{Na}}) \\
m_\infty &= 1/(1+\exp(-(V_{\mathrm{m}}+47.1)/3.1)) \\
\tau_m &= 0.9/\cosh((V_{\mathrm{m}}+47.1)/6.2) \\
h_\infty &= 1/(1+\exp((V_{\mathrm{m}}+57)/3)) \\
\tau_h &= 20000/\cosh((V_{\mathrm{m}}+57)/6)
\end{aligned}
$$

T-type calcium current

$$
\begin{aligned}
I_{\mathrm{T}} &= m^2 hG(V_{\mathrm{m}}, [\mathrm{Ca}]_i, [\mathrm{Ca}]_o) \\
m_\infty &= 1/(1+\exp(-(V_{\mathrm{m}}+60)/6.2)) \\
\tau_m &= 0.204 + 0.333/(\exp(-(V_{\mathrm{m}}+135)/16.7) + \exp((V_{\mathrm{m}}+19.8)/18.2)) \\
h_\infty &= 1/(1+\exp((V_{\mathrm{m}}+84)/4)) \\
\tau_h &= (9.33 + 0.333\exp(-(V_{\mathrm{m}}+25)/10.5))H_\infty(-10, V_{\mathrm{m}}) + \\
&\quad 0.333\exp((V_{\mathrm{m}}+470)/66.6)H_\infty(10, V_{\mathrm{m}}) \\
\text{where} \quad & H_\infty(x_1, x_2) = 1/(1+\exp(x_1(x_2+81)))
\end{aligned}
$$

In the model, time is in ms, voltages are in mV, ion concentrations are in mM, currents are in μA cm^{-2}, conductance are in mS cm^{-2} and the membrane capacitance is in μF cm^{-2}. The membrane capacitance is assumed to be unity and the reversal potentials are set to $E_{\mathrm{Na}} = 45$, $E_{\mathrm{K}} = -95$, $E_{\mathrm{hyp}} = -43$ mV, the conductances to $g_{\mathrm{Na,L}} = 0.0207$, $g_{\mathrm{K,L}} = 0.05$, $g_{\mathrm{Na}} = 30$, $g_{\mathrm{K}} = 3.2$, $g_{\mathrm{hyp}} = 0.4$, $g_{\mathrm{Na,p}} = 45$ mS cm^{-2}.

Appendix C

Spike sorting

Spike detection

Spikes were detected by amplitude thresholding the MER signal. In particular, local maxima of the MER signal that exceed a predefined threshold were flagged as a spike event. The predefined threshold was set as a multiple of the noise-level of the MER signal. The noise-level could not be directly measured and had to be estimated from the whole MER signal (noise, spikes and artefacts). For noise-level estimation we used the mode-based envelope method as proposed by Dolan et al. [51], under the assumption that the noise of the MER fragment was Gaussian distributed. This is a reasonable assumption, as the background noise signal is a superposition of distinct independent signals. This method uses the fact that the envelope, estimated using the Hilbert transformation, of a band-limited Gaussian noise signal, follows a Rayleigh distribution. The mode, i.e., the amplitude that occurs most frequently, of this Rayleigh distribution is exactly equal to the standard deviation of the underlying Gaussian distribution. This mode provides a reliable noise-level estimate, which is just very moderately influenced by spikes and high amplitude artefacts [51].

For all MER fragments we used a threshold that was 4.5 times the noise-level estimate. The number of detected spikes should increase upon lowering this threshold; however, in case of small amplitude spikes, differences in spike waveform between different neurons are indiscernible, because they are in the order of the noise level. To obtain the waveform of each detected spike we extracted a data window of 1.2 ms (25 samples) from the MER fragment, starting 0.4 ms (8 samples) prior to and ending 0.8 ms (16 samples) after the time of the spike event (peak). Subsequently, all spike waveforms were aligned to their peak at data point 9. Thus we obtained an initial spike matrix $S \epsilon \mathbb{R}^{25 \times n}$, with n the numbers of spikes. From this spike matrix a re-sampled spike matrix $S \epsilon \mathbb{R}^{32 \times n}$ was calculated in which the following issues were incorporated.

Overlapping spikes: different putative neurons may spike almost simultaneously and their waveforms will then overlap. Overlapping spikes were considered as outliers and were removed from the spike matrix. To remove overlapping spikes we ignored spike events that occurred within 1 ms from each other.

Artefacts: it could happen that artefacts exceeded the threshold and were flagged as spike event. Therefore, an event was only classified as spike if it satisfied the following constraints:

1. The time between the positive and negative peak of a spike waveform should not exceed 0.6 ms.
2. The (absolute) amplitude of the negative peak should be at least 0.3 times the amplitude of the positive peak.
3. Peak amplitude should not be higher than 10 times the threshold.

Misalignment: for the spike waveform analysis it is important that the spikes are correctly aligned with each other. The peak of the waveform is only reached for a very short time and therefore the exact moment at which a peak is reached will in general occur between two consecutive samples. Alignment of the waveforms to their peak can have a time shift that is a fraction of the sampling period. To avoid spike misalignments due to insufficient sampling, peaks were determined from a 4 times upsampled spike waveform, using cubic splines. After aligning, the interpolated waveforms were resampled to have 32 samples in a time window of 1.2 ms. In particular, we had 10 samples before and 21 samples after peak.

Feature extraction

Each column of S represents a time series of the spike waveform and is a point in a 32-dimensional space of raw sample values. The stored waveforms form a cloud of points in this high-dimensional space. In a high-dimensional space, standard clustering algorithm has the problem to end up in a local minimum. Therefore, to distinguish between different spike waveforms, the dimensionality of each spike waveform was reduced by extracting discriminative features from the spike waveform. We used a wavelet based dimension reduction method for spike feature extraction [89, 118, 174]. The discrete wavelet transform gives a time–frequency decomposition of the spike waveform with optimal resolution in both the time and the frequency domains [174]. Therefore, very localized waveform differences of the different neurons can be discerned with wavelets. Several studies [89, 118, 163, 174] have shown that a wavelet-based spike feature extraction method outperforms the commonly used principal component analysis based method. Especially, when the spike waveforms

demonstrate high frequency features (sharp edges) or the presence of high recording noise [163].

We used a fourth-level discrete Haar wavelet transform [129] to decompose each spike waveform with length 32 into 32 wavelet coefficients (30 detail and 2 approximation coefficients). Since the wavelet decomposition did not reduce the dimensionality of the spike waveform, the Kolmogorov–Smirnov test for normality [172] was utilized to extract six wavelet coefficients whose distribution over all spike waveforms differed most from the normal distribution. This strategy promotes extracting of wavelet coefficients with multi-modal distribution, thus enhancing the separation between different clusters (neurons).

Clustering

The 6 extracted wavelet coefficients were used as feature for the clustering step. For the clustering, a classification expectation maximization algorithm [42] was used, as implemented in KlustaKwik version 1.7 [81]. The default settings were used, except for the minimum number of clusters and the maximum number of iterations, which were set to 3 and 1000, respectively.

After clustering we obtained for each cluster the ordered times of occurrence of each spike (spike times) in terms of a multiple of the sampling interval ($\mathrm{d}t$). The sequence of ordered spike times can be considered as a realization of a stochastic orderly point process. For orderly point process the number of events (spikes) in an interval of duration $\mathrm{d}t$ will take on the value 0 or 1 depending on the occurrence of a spike [74]. So we could create a spike train, a sequence of zeros and ones with the same length as the recording, of the ordered spike times.

References

[1] O. Aizman, H. Brismar, P. Uhlén, E. Zettergren, A. I. Levey, H. Forssberg, P. Greengard, and A. Aperia. Anatomical and physiological evidence for d1 and d2 dopamine receptor colocalization in neostriatal neurons. *Nature Neuroscience*, 3(3):226–230, 2000.

[2] R. L. Albin, A. B. Young, and J. B. Penney. The functional anatomy of basal ganglia disorders. *Trends in Neurosciences*, 12(10):366–375, 1989.

[3] G. E. Alexander and M. D. Crutcher. Functional architecture of basal ganglia circuits: neural substrates of parallel processing. *Trends in Neurosciences*, 13(7):266–271, 1990.

[4] G. E. Alexander, M. R. DeLong, and P. L. Strick. Parallel organization of functionally segregated circuits linking basal ganglia and cortex. *Annual Review of Neuroscience*, 9(1):357–381, 1986.

[5] R. Ammari, B. Bioulac, L. Garcia, and C. Hammond. The subthalamic nucleus becomes a generator of bursts in the dopamine-depleted state. its high frequency stimulation dramatically weakens transmission to the globus pallidus. *Frontiers in Systems Neuroscience*, 5(43), June 2011.

[6] F. Amtage, K. Henschel, B. Schelter, J. Vesper, J. Timmer, C. H. Lücking, and B. Hellwig. High functional connectivity of tremor related subthalamic neurons in parkinson's disease. *Clinical Neurophysiology*, 120(9), September 2009.

[7] A. G. Androulidakis, S. Khan, V. Litvak, C. W. Pleydell-Pearce, P. Brown, and S. S. Gill. Local field potential recordings from the pedunculopontine nucleus in a parkinsonian patient. *Neuroreport*, 19(1):59–62, January 2008.

[8] A. G. Androulidakis, P. Mazzone, V. Litvak, W. Penny, M. Dileone, L. M. F. D. Gaynor, S. Tisch, V. D. Lazzaro, and P. Brown. Oscillatory activity in the pedunculopontine area of patients with parkinson's disease. *Experimental neurology*, 211(1):59–66, May 2008.

[9] B. Aouizerate, D. Guehl, E. Cuny, A. Rougier, B. Bioulac, J. Tignol, and P. Burbaud. Pathophysiology of obsessive-compulsive disorder: a necessary link between phenomenology, neuropsychology, imagery and physiology. *Progress in Neurobiology*, 72(3):195–221, 2004.

[10] I. Bar-Gad, Y. Ritov, E. Vaadia, and H. Bergman. Failure in identification of overlapping spikes from multiple neuron activity causes artificial correlations. *Journal of Neuroscience Methods*, 107(1-2), May 2001.

[11] I. Bar-Gad, G. Morris, and H. Bergman. Information processing, dimensionality reduction and reinforcement learning in the basal ganglia. *Progress in Neurobiology*, 71(6):439–473, 2003.

[12] A. L. Benabid. Deep brain stimulation for parkinson's disease. *Current Opinion in Neurobiology*, 13(6):696–706, 2003.

[13] A. L. Benabid, P. Pollak, A. Louveau, S. Henry, and J. de Rougemont. Combined (thalamotomy and stimulation) stereotactic surgery of the vim thalamic nucleus for bilateral parkinson disease. *Applied neurophysiology*, 50:344–346, 1987.

[14] A. L. Benabid, P. Pollak, D. Hoffmann, C. Gervason, M. Hommel, J. E. Perret, J. de Rougemont, and D. M. Gao. Long-term suppression of tremor by chronic stimulation of the ventral intermediate thalamic nucleus. *The Lancet*, 337(8738):403–406, 1991.

[15] A. L. Benabid, P. Pollak, C. Gross, D. Hoffmann, A. Benazzouz, D. M. Gao, A. Laurent, and M. G. J. Perret. Acute and long-term effects of subthalamic nucleus stimulation in parkinson's disease. *Stereotactic and Functional Neurosurgery*, 62:76–84, 1994.

[16] A. L. Benabid, S. Chabardes, J. Mitrofanis, and P. Pollak. Deep brain stimulation of the subthalamic nucleus for the treatment of parkinson's disease. *The Lancet Neurology*, 8(1):67–81, 2009.

[17] E. E. Benarroch. Subthalamic nucleus and its connections: Anatomic substrate for the network effects of deep brain stimulation. *Neurology*, 70(21), May 2008.

[18] A. Benazzouz, S. Breit, A. Koudsie, P. Pollak, P. Krack, and A. L. Benabid. Intraoperative microrecordings of the subthalamic nucleus in parkinson's disease. *Movement Disorders*, 17 (Suppl 3):S145–149, 2002.

[19] H. Bergman and G. Deuschl. Pathophysiology of parkinson's disease: from clinical neurology to basic neuroscience and back. *Movement Disorders*, 17(Suppl 3), May 2002.

[20] H. Bergman, T. Wichmann, B. Karmon, and M. R. DeLong. The primate subthalamic nucleus. ii. neuronal activity in the mptp model of parkinsonism. *Journal of Neurophysiology*, 72(2): 507–520, 1994.

[21] H. Bergman, A. Feingold, A. Nini, A. Raz, H. Slovin, M. Abeles, and E. Vaadia. Physiological aspects of information processing in the basal ganglia of normal and parkinsonian primates. *Trends in Neuroscience*, 21(1):32–38, 1998.

[22] C. Bernasconi and P. König. On the directionality of cortical interactions studied by structural analysis of electrophysiological recordings. *Biological Cybernetics*, 81(3):199–210, 1999.

[23] H. Bernheimer, W. Birkmayer, O. Hornykiewicz, K. Jellinger, and F. Seitelberger. Brain dopamine and the syndromes of parkinson and huntington clinical, morphological and neurochemical correlations. *Journal of the Neurological Sciences*, 20(4):415–455, 1973.

[24] J. Best, C. Park, D. Terman, and C. Wilson. Transitions between irregular and rhythmic firing patterns in excitatory-inhibitory neuronal networks. *Journal of Computational Neuroscience*, 23 (2):217–235, 2007.

[25] R. Betarbet, T. B. Sherer, and J. T. Greenamyre. Animal models of parkinson's disease. *Bioessays*, 24(4):308–318, April 2002.

[26] E. Bezard, C. E. Gross, and J. M. Brotchie. Presymptomatic compensation in parkinson's disease is not dopamine-mediated. *Trends in Neurosciences*, 26(4):215–221, 2003.

[27] G. Bi and M. Poo. Synaptic modifications in cultured hippocampal neurons: dependence on spike timing, synaptic strength, and postsynaptic cell type. *The Journal of Neuroscience*, 18(24): 10464–10472, 1998.

[28] T. Boraud, E. Bezard, B. Bioulac, and C. E. Gross. From single extracellular unit recording in experimental and human parkinsonism to the development of a functional concept of the role played by the basal ganglia in motor control. *Progress in Neurobiology*, 66(4):265–283, 2002.

[29] L. J. Bour, M. F. Contarino, E. M. Foncke, R. M. de Bie, P. van den Munckhof, J. D. Speelman, and P. R. Schuurman. Long-term experience with intraoperative microrecording during dbs neurosurgery in stn and gpi. *Acta Neurochirurgica (Wien)*, 152(12):2069–2077, 2010.

[30] J. Bové, D. Prou, C. Perier, and S. Przedborski. Toxin-induced models of parkinsons disease. *NeuroRx: The Journal of the American Society for Experimental NeuroTherapeutics*, 2(3), 2005.

[31] S. Breit, R. Bouali-Benazzouz, A. Benabid, and A. Benazzouz. Unilateral lesion of the nigrostriatal pathway induces an increase of neuronal activity of the pedunculopontine nucleus, which is reversed by the lesion of the subthalamic nucleus in the rat. *European journal of neuroscience*, 14:1833–1842, October 2001.

[32] P. Brown. Oscillatory nature of human basal ganglia activity: Relationship to the pathophysiology of parkinson's disease. *Movement Disorders*, 18(4):357–363, 2003.

[33] P. Brown. Abnormal oscillatory synchronisation in the motor system leads to impaired movement. *Current Opinion in Neurobiology*, 17(6):656–664, 2007.

[34] P. Brown, A. Oliviero, P. Mazzone, A. Insola, P. Tonali, and V. D. Lazzaro. Dopamine dependency of oscillations between subthalamic nucleus and pallidum in parkinson's disease. *The Journal of Neuroscience*, 21(3):1033–1038, 2001.

[35] C. R. Butson, S. E. Cooper, J. M. Henderson, and C. C. McIntyre. Patient-specific analysis of the volume of tissue activated during deep brain stimulation. *NeuroImage*, 34(2):661–670, 2007.

[36] G. Buzsáki. Large-scale recording of neuronal ensembles. *Nature Neuroscience*, 7(5):446–451, 2004.

[37] G. Buzsáki, C. Geisler, D. A. Henze, and X. Wang. Interneuron diversity series: Circuit complexity and axon wiring economy of cortical interneurons. *Trends in Neurosciences*, 27(4):186–193, 2004.

[38] H. Cagnan, H. G. E. Meijer, S. A. van Gils, M. Krupa, T. Heida, M. Rudolph, W. J. Wadman, and H. C. F. Martens. Frequency-selectivity of a thalamocortical relay neuron during parkinson's disease and deep brain stimulation: a computational study. *European Journal of Neuroscience*, 30(7):1306–1317, 2009.

[39] H. Cagnan, K. Dolan, X. He, M. F. Contarino, R. Schuurman, P. van den Munckhof, W. J. Wadman, L. Bour, and H. C. F. Martens. Automatic subthalamic nucleus detection from microelectrode recordings based on noise level and neuronal activity. *Journal of Neural Engineering*, 8(4):046006, 2011.

[40] N. Caporale and Y. Dan. Spike timing-dependent plasticity: a hebbian learning rule. *Annual Review of Neuroscience*, 31:25–46, 2008.

[41] A. Capozzo, T. Florio, G. Confalone, D. Minchella, P. Mazzone, and E. Scarnati. Low frequency stimulation of the pedunculopontine nucleus modulates electrical activity of subthalamic neurons in the rat. *Journal of neural transmission*, 116:51–56, 2009.

[42] G. Celeux and G. Govaert. A classification em algorithm for clustering and two stochastic versions. *Computational Statistics and Data Analysis*, 14(3):315–332, 1992.

[43] M. F. Contarino, L. J. Bour, M. Bot, P. van den Munckhof, J. D. Speelman, P. R. Schuurman, and R. M. A. de Bie. Pallidotomy suppresses beta power in the subthalamic nucleus of parkinson's disease patients. *European Journal of Neuroscience*, 33(7):1275–1280, 2011.

[44] M. F. Contarino, L. J. Bour, M. Bot, P. van den Munckhof, J. D. Speelman, P. R. Schuurman, and R. M. de Bie. Tremor-specific neuronal oscillation pattern in dorsal subthalamic nucleus of parkinsonian patients. *Brain Stimulation*, 5(3):305–314, 2012.

[45] A. Cools, R. Brachten, D. Heeren, A. Willemen, and B. Ellenbroek. Search after neurobiological profile of individual-specific features of wistar rats. *Brain Research Bulletin*, 24(1):49–69, 1990.

[46] V. Cutsuridis, T. Heida, W. Duch, and K. Doya. Neurocomputational models of brain disorders. *Neural Networks*, 24(6):513–514, 2011.

[47] M. R. DeLong. Primate models of movement disorders of basal ganglia origin. *Trends in Neurosciences*, 13(7):281–285, 1990.

[48] A. Destexhe, M. Neubig, D. Ulrich, and J. Huguenard. Dendritic low-threshold calcium currents in thalamic relay cells. *Journal of neuroscience*, 18(10):35743588, May 1998.

[49] R. Deumens, A. Blokland, and J. Prickaerts. Modeling parkinson's disease in rats: An evaluation of 6-ohda lesions of the nigrostriatal pathway. *Experimental Neurology*, 175(2):303–317, 2002.

[50] A. Dhooge, W. Govaerts, and Y. A. Kuznetsov. Matcont: A matlab package for numerical bifurcation analysis of odes. *ACM transactions on mathematical software*, 29(2):141–164, June 2003.

[51] K. Dolan, H. C. F. Martens, P. R. Schuurman, and L. J. Bour. Automatic noise-level detection for extra-cellular micro-electrode recordings. *Medical and Biological Engineering and Computing*, 47(7):791–800, 2009.

[52] E. R. Dorsey, R. Constantinescu, J. P. Thompson, K. M. Biglan, R. G. Holloway, K. Kieburtz, F. J. Marshall, B. M. Ravina, G. Schifitto, A. Siderowf, and C. M. Tanner. Projected number of people with parkinson disease in the most populous nations, 2005 through 2030. *Neurology*, 68(5):384–386, 2007.

[53] A. D. Dorval, A. M. Kuncel, M. J. Birdno, D. A. Turner, and W. M. Grill. Deep brain stimulation alleviates parkinsonian bradykinesia by regularizing pallidal activity. *Journal of Neurophysiology*, 104(2):911–921, 2010.

[54] M. S. Fee, P. P. Mitra, and D. Kleinfeld. Variability of extracellular spike waveforms of cortical neurons. *Journal of Neurophysiology*, 76(6):3823–3833, 1996.

[55] G. Fein, J. Raz, F. F. Brown, and E. L. Merrin. Common reference coherence data are confounded by power and phase effects. *Electroencephalography and Clinical Neurophysiology*, 69 (6):581–584, Februari 1988.

[56] D. E. Feldman. Timing-based ltp and ltd at vertical inputs to layer ii/iii pyramidal cells in rat barrel cortex. *Neuron*, 27(1):45–56, 2000.

[57] M. U. Ferraye, B. Debû, V. Fraix, L. Goetz, C. Ardouin, J. Yelnik, C. Henry-Lagrange, E. Seigneuret, B. Piallat, P. Krack, J.-F. L. Bas, A.-L. Benabid, S. Chabardès, and P. Pollak. Effects of pedunculopontine nucleus area stimulation on gait disorders in parkinson's disease. *Brain*, 133:205–214, 2010.

[58] T. Florio, E. Scarnati, G. Confalone, D. Minchella, S. Galati, P.Stanzione, A. Stefani, and P. Mazzone. High-frequency stimulation of the subthalamic nucleus modulates the activity of pedunculopontine neurons through direct activation of excitatory fibres as well as through indirect activation of inhibitory pallidal fibres in the rat. *European journal of neuroscience*, 25: 1174–1186, 2007.

[59] W. J. Freeman. *Mass action in the nervous system*. Academic Press, New York, 1975.

[60] S. Galati, E. Scarnati, P. Mazzone, P. Stanzione, and A. Stefani. Deep brain stimulation promotes excitation and inhibition in subthalamic nucleus in parkinson's disease. *Neuroreport*, 19(6):661–666, April 2008.

[61] A. Galvan and T. Wichmann. Pathophysiology of parkinsonism. *Clinical Neurophysiology*, 119 (7):1459–1474, 2008.

[62] P. Gatev, O. Darbin, and T. Wichmann. Oscillations in the basal ganglia under normal conditions and in movement disorders. *Movement Disorders*, 21(10):1566–1577, 2006.

[63] C. R. Gerfen. The neostriatal mosaic: multiple levels of compartmental organization. *Trends in Neurosciences*, 15(4):133–139, 1992.

[64] C. R. Gerfen and C. J. Wilson. Chapter ii the basal ganglia. In A. B. L.W. Swanson and T. Hökfelt, editors, *Integraded systems of the CNS, part III Cerebellum, basal ganglia, olfactory system*, volume 12 of *Handbook of Chemical Neuroanatomy*, pages 371–468. Elsevier, Amsterdam, 1996.

[65] G. L. Gerstein. Cross-correlation measures of unresolved multi-neuron recordings. *Journal of Neuroscience Methods*, 100(1-2), 2000.

[66] D. Golomb and J. Rinzel. Clustering in globally coupled inhibitory neurons. *Physica D: Nonlinear Phenomena*, 72(3):259–282, 1994.

[67] B. Gourévitch and J. J. Eggermont. A simple indicator of nonstationarity of firing rate in spike trains. *Journal of Neuroscience Methods*, 163(1):181–187, 2007.

[68] J. G. Greenfield and F. D. Bosanquet. The brain-stem lesions in parkinsonism. *Journal of Neurology, Neurosurgery, and Psychiatry*, 16:213–226, 1953.

[69] Y. Guo and J. E. Rubin. Multi-site stimulation of subthalamic nucleus diminishes thalamocortical relay errors in a biophysical network model. *Neural Networks*, 24(6):602–616, 2011.

[70] Y. Guo, J. E. Rubin, C. C. McIntyre, J. L. Vitek, and D. Terman. Thalamocortical relay fidelity varies across subthalamic nucleus deep brain stimulation protocols in a data-driven computational model. *Journal of Neurophysiology*, 99(3):1477–1492, 2008.

[71] J. S. Haas, T. Nowotny, and H. D. I. Abarbanel. Spike-timing-dependent plasticity of inhibitory synapses in the entorhinal cortex. *Journal of Neurophysiology*, 96(6):3305–3313, 2006.

[72] P. J. Hahn and C. C. McIntyre. Modeling shifts in the rate and pattern of subthalamopallidal network activity during deep brain stimulation. *Journal of Computational Neuroscience*, 28(3): 425–441, Juni 2010.

[73] P. J. Hahn, G. S. Russo, T. Hashimoto, S. Miocinovic, W. Xu, C. C. McIntyre, and J. L. Vitek. Pallidal burst activity during therapeutic deep brain stimulation. *Experimental Neurology*, 211 (1):243–251, 2008.

[74] D. M. Halliday, J. R. Rosenberg, A. M. Amjad, P. Breeze, B. A. Conway, and S. F. Farmer. A framework for the analysis of mixed time series/point process data - theory and application to the study of physiological tremor, single motor unit discharges and electromyograms. *Progress in Biophysics and Molecular Biology*, 64(2-3):237–278, 1995.

[75] C. Hamani, J. A. Saint-Cyr, J. Fraser, M. Kaplitt, and A. M. Lozano. The subthalamic nucleus in the context of movement disorders. *Brain*, 127(1):4–20, 2004.

[76] C. Hamani, J. Neimat, and A. M. Lozano. Deep brain stimulation for the treatment of parkinson's disease. In P. Riederer, H. Reichmann, M. B. H. Youdim, and M. Gerlach, editors, *Parkinson's Disease and Related Disorders*, volume 70 of *Journal of Neural Transmission. Supplementa*, pages 393–399. Springer Vienna, 2006.

[77] C. Hamani, S. Stone, A. Laxton, and A. M. Lozano. The pedunculopontine nucleus and movement disorders: Anatomy and the role for deep brain stimulation. *Parkinsonism and Related Disorders*, 13:s276–s280, 2007.

[78] R. J. Hamm, B. R. Pike, D. M. O'dell, B. G. Lyeth, and L. W. Jenkins. The rotarod test: An evaluation of its effectiveness in assessing motor deficits following traumatic brain injury. *Journal of Neurotrauma*, 11(2):187–196, 1994.

[79] C. Hammond and J. Yelnik. Intracellular labelling of rat subthalamic neurones with horseradish peroxidase: Computer analysis of dendrites and characterization of axon arborization. *Neuroscience*, 8(4):781–790, 1983.

[80] C. Hammond, H. Bergman, and P. Brown. Pathological synchronization in parkinson's disease: networks, models and treatments. *Trends in Neurosciences*, 30(7):357–364, 2007.

[81] K. D. Harris, D. A. Henze, J. Csicsvari, H. Hirase, and G. Buzsáki. Accuracy of tetrode spike separation as determined by simultaneous intracellular and extracellular measurements. *Journal of Neurophysiology*, 84(1):401–414, 2000.

[82] C. Hauptmann and P. A. Tass. Cumulative and after-effects of short and weak coordinated reset stimulation: a modeling study. *Journal of Neural Engineering*, 6(1):016004, 2009.

[83] T. Heida, E. Marani, and K. G. Usunoff. *The subthalamic nucleus, part II: modelling and simulation of activity*, volume 199 of *Advances in Anatomy, Embryology and Cell Biology*. Springer Verlag, London, 2008.

[84] D. N. Hill, S. B. Mehta, and D. Kleinfeld. Quality metrics to accompany spike sorting of extracellular signals. *The Journal of Neuroscience*, 31(24):8699–8705, June 2011.

[85] A. L. Hodgkin and A. F. Huxley. A quantitative description of membrane current and its application to conduction and excitation in nerve. *The Journal of Physiology*, 117(4):500–544, 1952.

[86] C. D. Holmgren and Y. Zilberter. Coincident spiking activity induces long-term changes in inhibition of neocortical pyramidal cells. *The Journal of Neuroscience*, 21(20):8270–8277, 2001.

[87] A. J. Hughes, S. E. Daniel, L. Kilford, and A. J. Lees. Accuracy of clinical diagnosis of idiopathic parkinson's disease: a clinico-pathological study of 100 cases. *Journal of Neurology, Neurosurgery, and Psychiatry*, 55(3):181–184, March 1992.

[88] J. R. Huguenard and D. A. McCormick. Simulation of the currents involved in rhythmic oscillations in thalamic relay neurons. *Journal of neurophysiology*, 68(4):1373–1383, October 1992.

[89] E. Hulata, R. Segev, and E. Ben-Jacob. A method for spike sorting and detection based on wavelet packets and shannon's mutual information. *Journal of Neuroscience Methods*, 117(1): 1–12, 2002.

[90] M. J. Hurley and P. Jenner. What has been learnt from study of dopamine receptors in parkinson's disease? *Pharmacology & Therapeutics*, 111(3):715–728, 2006.

[91] E. M. Izhikevich. *Dynamical systems in neuroscience: The geometry of excitability and bursting*. MIT press, Cambridge, MA, 2006.

[92] H. Jahnsen and R. Llinás. Electrophysiological properties of guinea-pig thalamic neurones: an in vitro study. *The Journal of Physiology*, 349(1):205–226, 1984.

[93] J. Jankovic. Parkinson's disease: clinical features and diagnosis. *Journal of neurology, neurosurgery, and psychiatry*, 79:368–376, 2008.

[94] F. Javoy, C. Sotelo, A. Herbet, and Y. Agid. Specificity of dopaminergic neuronal degeneration induced by intracerebral injection of 6-hydroxydopamine in the nigrostriatal dopamine system. *Brain Research*, 102(2):201–215, 1976.

[95] K. Jellinger. Quantitative changes in some subcortical nuclei in aging, alzheimer's disease and parkinson's disease. *Neurobiology of Aging*, 8(6):556–561, 1987.

[96] N. Jenkinson and P. Brown. New insights into the relationship between dopamine, beta oscillations and motor function. *Trends in Neurosciences*, 34(12):611–618, 2011.

[97] N. Jenkinson, D. Nandi, R. C. Miall, J. F. Stein, and T. Z. Aziz. Pedunculopontine nucleus stimulation improves akinesia in a parkinsonian monkey. *Neuroreport*, 15(17):2621–2624, 2004.

[98] N. Jenkinson, D. Nandi, K. Muthusamy, N. J. Ray, R. Gregory, J. F. Stein, and T. Z. Aziz. Anatomy, physiology, and pathophysiology of the pedunculopontine nucleus. *Movement Disorders*, 24(3):319–328, 2009.

[99] D. Joel and I. I. Weiner. The connections of the dopaminergic system with the striatum in rats and primates: an analysis with respect to the functional and compartmental organization of the striatum. *Neuroscience*, 96(3):451–474, 2000.

[100] G. Jonsson. Chemical neurotoxins as denervation tools in neurobiology. *Annual Review of Neuroscience*, 3(1):169–187, 1980.

[101] M. Joshua, S. Elias, O. Levine, and H. Bergman. Quantifying the isolation quality of extracellularly recorded action potentials. *Journal of Neuroscience Methods*, 163:267–282, 2007.

[102] E. Juergens, A. Guettler, and R. Eckhorn. Visual stimulation elicits locked and induced gamma oscillations in monkey intracortical- and eeg-potentials, but not in human eeg. *Experimental Brain Research*, 129(2):247–259, 1999.

[103] E. R. Kandel, J. H. Schwartz, and T. M. Jessel. *Principles of Neural Science*. McGraw-Hill, New York, fourth edition, 2000.

[104] Y. Kaneoke and J. L. Vitek. Burst and oscillation as disparate neuronal properties. *Journal of Neuroscience Method*, 68(2):211–223, 1996.

[105] Y. Kang and S. Kitai. Electrophysiological properties of pedunculopontine neurons and their postsynaptic responses following stimulation of substantia nigra reticulata. *Brain Research*, 535:79–95, 1990.

[106] A. Kepecs, M. C. W. van Rossum, S. Song, and J. Tegner. Spike-timing-dependent plasticity: common themes and divergent vistas. *Biological Cybernetics*, 87(5):446–458, 2002.

[107] M. C. Keuken, H. B. M. Uylings, S. Geyer, A. Schäfer, R. Turner, and B. U. Forstmann. Are there three subdivisions in the primate subthalamic nucleus? *Frontiers in Neuroanatomy*, 6: 00014, 2012.

[108] S. J. Kiebel, M. I. Garrido, R. J. Moran, and K. J. Friston. Dynamic causal modelling for eeg and meg. *Cognitive Neurodynamics*, 2(2):121–136, 2008.

[109] P. Krack, A. Batir, N. van Blercom, S. Chabardes, V. Fraix, C. Ardouin, A. Koudsie, P. D. Limousin, A. Benazzouz, J. F. LeBas, A. L. Benabid, and P. Pollak. Five-year follow-up of bilateral stimulation of the subthalamic nucleus in advanced parkinson's disease. *New England Journal of Medicine*, 349(20):1925–1934, 2003.

[110] A. A. Kühn, D. Williams, A. Kupsch, P. Limousin, M. Hariz, G. Schneider, K. Yarrow, and P. Brown. Event-related beta desynchronization in human subthalamic nucleus correlates with motor performance. *Brain*, 127(4):735–746, 2004.

[111] A. A. Kühn, A. Kupsch, G. Schneider, and P. Brown. Reduction in subthalamic 8-35 hz oscillatory activity correlates with clinical improvement in parkinson's disease. *European Journal of Neuroscience*, 23(7):1956–1960, 2006.

[112] A. A. Kühn, F. Kempf, C. Brücke, L. G. Doyle, I. Martinez-Torres, A. Pogosyan, T. Trottenberg, A. Kupsch, G. Schneider, M. I. Hariz, W. Vandenberghe, B. Nuttin, and P. Brown. High-frequency stimulation of the subthalamic nucleus suppresses oscillatory β activity in patients with parkinson's disease in parallel with improvement in motor performance. *The Journal of Neuroscience*, 28(24):6165–6173, 2008.

[113] A. A. Kühn, A. Tsui, T. Aziz, N. Ray, C. Brücke, A. Kupsch, G. Schneider, and P. Brown. Pathological synchronisation in the subthalamic nucleus of patients with parkinson's disease relates to both bradykinesia and rigidity. *Experimental Neurology*, 215(2):380–387, 2009.

[114] A. Kumar, S. Cardanobile, S. Rotter, and A. Aertsen. The role of inhibition in generating and controlling parkinson's disease oscillations in the basal ganglia. *Frontiers in Systems Neuroscience*, 5(86):1–14, 2011.

[115] Y. Kuramoto. *Chemical oscillations, waves, and turbulence*. Springer, New York, 1984.

[116] D. Labarre, W. Meissner, and T. Boraud. Measure of the regularity of events in stochastic point processes, application to neuron activity analysis. In *International Conference on Acoustics, Speech, and Signal Processing*, pages 489–492, April 2008.

[117] A. D. Legatt, J. Arezzo, and H. G. V. Jr. Averaged multiple unit activity as an estimate of phasic changes in local neuronal activity: effects of volume-conducted potentials. *Journal of Neuroscience Methods*, 2(2):203 – 217, 1980.

[118] J. C. Letelier and P. P. Weber. Spike sorting based on discrete wavelet transform coefficients. *Journal of Neuroscience Methods*, 101(2):93–106, 2000.

[119] M. Lévesque and A. Parent. The striatofugal fiber system in primates: a reevaluation of its organization based on single-axon tracing studies. *Proceedings of the National Academy of Sciences of the United States of America*, 102(33):11888–11893, 2005.

[120] R. Levy, W. D. Hutchison, A. M. Lozano, and J. O. Dostrovsky. High-frequency synchronization of neuronal activity in the subthalamic nucleus of parkinsonian patients with limb tremor. *The Journal of Neuroscience*, 20(20):7766–7775, 2000.

[121] R. Levy, P. Ashby, W. D. Hutchison, A. E. Lang, A. M. Lozano, and J. O. Dostrovsky. Dependence of subthalamic nucleus oscillations on movement and dopamine in parkinson's disease. *Brain*, 125(6):1196–1209, 2002.

[122] P. Limousin, P. Pollak, A. Benazzouz, D. Hoffmann, J. F. L. Bas, J. E. Perret, A. L. Benabid, and E. L. Broussolle. Effect on parkinsonian signs and symptoms of bilateral subthalamic nucleus stimulation. *The Lancet*, 345(8942):91–95, 1995.

[123] M. D. Lindner, C. K. Cain, M. A. Plone, B. R. Frydel, T. J. Blaney, D. F. Emerich, and M. R. Hoane. Incomplete nigrostriatal dopaminergic cell loss and partial reductions in striatal dopamine produce akinesia, rigidity, tremor and cognitive deficits in middle-aged rats. *Behavioural Brain Research*, 102(1-2):1–16, 1999.

[124] M. A. J. Lourens, H. G. E. Meijer, T. Heida, E. Marani, and S. A. van Gils. The pedunculopontine nucleus as an additional target for deep brain stimulation. *Neural Networks*, 24(6): 617–630, 2011.

[125] J. L. Luján, A. M. Noecker, C. R. Butson, S. E. Cooper, B. L. Walter, J. L. Vitek, and C. C. McIntyre. Automated 3-dimensional brain atlas fitting to microelectrode recordings from deep brain stimulation surgeries. *Stereotactic and Functional Neurosurgery*, 87(4):229–240, 2009.

[126] A. Lüttjohann and G. van Luijtelaar. The dynamics of cortico-thalamo-cortical interactions at the transition from pre-ictal to ictal lfps in absence epilepsy. *Neurobiology of Disease*, 47(1): 49–60, 2012.

[127] J. C. Magee and D. Johnston. A synaptically controlled, associative signal for hebbian plasticity in hippocampal neurons. *Science*, 275(5297):209–213, 1997.

[128] P. J. Magill, J. P. Bolam, and M. D. Bevan. Dopamine regulates the impact of the cerebral cortex on the subthalamic nucleus-globus pallidus network. *Neuroscience*, 106(2):313–330, 2001.

[129] S. G. Mallat. A theory for multiresolution signal decomposition: The wavelet representation. *IEEE Transactions on Pattern Analysis and Machine Intelligence*, 2(7):674–693, 1989.

[130] N. Mallet, A. Pogosyan, L. F. Mérton, J. P. Bolam, P. Brown, and P. J. Magill. Parkinsonian beta oscillations in the external globus pallidus and their relationship with subthalamic nucleus activity. *The Journal of Neuroscience*, 28(52):14245–14258, 2008.

[131] N. Mallet, A. Pogosyan, A. Sharott, J. Csicsvari, J. P. Bolam, P. Brown, and P. J. Magill. Disrupted dopamine transmission and the emergence of exaggerated beta oscillations in subthalamic nucleus and cerebral cortex. *The Journal of Neuroscience*, 28(18):4795–4806, 2008.

[132] H. Markram, J. Lübke, M. Frotscher, and B. Sakmann. Regulation of synaptic efficacy by coincidence of postsynaptic aps and epsps. *Science*, 275(5297):213–215, 1997.

[133] M. Matsumura, K. Watanabe, and C. Ohye. Single-unit activity in the primate nucleus tegmenti pedunculopontinus related to voluntary arm movement. *Neuroscience Research*, 28: 155–165, March 1997.

[134] P. Mazzone, A. Lozano, P. Stanzione, S. Galati, E. Scarnati, A. Peppe, and A. Stefani. Implantation of human pedunculopontine nucleus: A safe and clinically relevant target in parkinson's disease. *Neuroreport*, 16(17):1877–1881, November 2005.

[135] D. A. McCormick and J. R. Huguenard. A model of the electrophysiological properties of thalamocortical relay neurons. *Journal of Neurophysiology*, 68(4):1384–1400, October 1992.

[136] C. C. McIntyre and P. J. Hahn. Network perspectives on the mechanisms of deep brain stimulation. *Neurobiology of Disease*, 38(3):329–337, 2010.

[137] H. G. E. Meijer, M. Krupa, H. Cagnan, M. A. J. Lourens, T. Heida, H. C. F. Martens, L. J. Bour, and S. A. van Gils. From parkinsonian thalamic activity to restoring thalamic relay using deep brain stimulation: new insights from computational modeling. *Journal of Neural Engineering*, 8(6):066005, 2011.

[138] J. Mena-Segovia, J. P. Bolam, and P. J. Magill. Pedunculopontine nucleus and basal ganglia: Distant relatives or part of thr same family. *Trends in Neurosciences*, 27(10):585–588, October 2004.

[139] F. A. Middleton and P. L. Strick. Basal ganglia and cerebellar loops: motor and cognitive circuits. *Brain Research Reviews*, 31(2-3):236–250, 2000.

[140] S. Miocinovic, A. M. Noecker, C. B. Maks, C. R. Butson, and C. C. McIntyre. Cicerone: stereotactic neurophysiological recording and deep brain stimulation electrode placement software system. In D. E. Sakas and B. A. Simpson, editors, *Operative Neuromodulation*, volume 97 of *Acta Neurochirurgica Supplementum*, pages 561–567. Springer Vienna, 2007.

[141] U. Mitzdorf. Properties of the evoked potential generators: current source-density analysis of visually evoked potentials in the cat cortex. *The International Journal of Neuroscience*, 33(1-2): 33–59, 1987.

[142] M. A. Moffitt and C. C. McIntyre. Model-based analysis of cortical recording with silicon microelectrodes. *Clinical Neurophysiology*, 116(9):2240–2250, 2005.

[143] A. Moran and I. Bar-Gad. Revealing neuronal functional organization through the relation between multi-scale oscillatory extracellular signals. *Journal of Neuroscience Methods*, 186(1): 116–129, 2010.

[144] A. Moran, H. Bergman, Z. Israel, and I. Bar-Gad. Subthalamic nucleus functional organization revealed by parkinsonian neuronal oscillations and synchrony. *Brain*, 131(12):3395–3409, 2008.

[145] R. J. Moran, N. Mallet, V. Litvak, R. J. Dolan, P. J. Magill, K. J. Friston, and P. Brown. Alterations in brain connectivity underlying beta oscillations in parkinsonism. *PLoS Computational Biology*, 7(8):e1002124, 2011.

[146] E. Moro, R. J. A. Esselink, J. Xie, M. Hommel, A. L. Benabid, and P. Pollak. The impact on parkinson's disease of electrical parameter settings in stn stimulation. *Neurology*, 59(5):706–713, 2002.

[147] A. Morrison, M. Diesmann, and W. Gerstner. Phenomenological models of synaptic plasticity based on spike timing. *Biological Cybernetics*, 98(6):459–478, 2008.

[148] L. J. Myers, M. Lowery, M. O'Malley, C. L. Vaughan, C. Heneghan, A. S. C. Gibson, Y. X. R. Harley, and R. Sreenivasan. Rectification and non-linear pre-processing of emg signals for cortico-muscular analysis. *Journal of Neuroscience Methods*, 124(2):157–165, 2003.

[149] A. Nambu. A new approach to understand the pathophysiology of parkinson's disease. *Journal of Neurology*, 252(Suppl 4):iv1–iv4, 2005.

[150] A. Nambu, M. Takada, M. Inase, and H. Tokuno. Dual somatotopical representations in the primate subthalamic nucleus: evidence for ordered but reversed body-map transformations

from the primary motor cortex and the supplementary motor area. *The Journal of Neuroscience*, 16(8):2671–2683, 1996.

[151] A. Nambu, H. Tokuno, I. Hamada, H. Kita, M. Imanishi, T. Akazawa, Y. Ikeuchi, and N. Hasegawa. Excitatory cortical inputs to pallidal neurons via the subthalamic nucleus in the monkey. *Journal of Neurophysiology*, 84(1):289–300, 2000.

[152] A. Nambu, H. Tokuno, and M. Takada. Functional significance of the cortico-subthalamo-pallidal "hyperdirect" pathway. *Neuroscience Research*, 43(2):111–117, 2002.

[153] D. Nandi, T. Z. Aziz, N. Giladi, J. Winter, and J. F. Stein1. Reversal of akinesia in experimental parkinsonism by gaba antagonist microinjections in the pedunculopontine nucleus. *Brain*, 125:2418–2430, 2002.

[154] D. Nandi, T. Z. Aziz, X. Liu, and J. F. Stein. Brainstem motor loops in the control of movement. *Movement Disorders*, 17(3):s22–s27, 2002.

[155] A. Nini, A. Feingold, H. Slovin, and H. Bergman. Neurons in the globus pallidus do not show correlated activity in the normal monkey, but phase-locked oscillations appear in the mptp model of parkinsonism. *Journal of Neurophysiology*, 74(4):1800–1805, 1995.

[156] J. A. Obeso, C. W. Olanow, and J. G. Nutt. Levodopa motor complications in parkinson's disease. *Trends in Neurosciences*, 23(Suppl 1):S1–7, 2000.

[157] J. A. Obeso, M. C. Rodriguez-Oroz, M. Rodriguez, J. L. Lanciego, J. Artieda, N. Gonzalo, and C. W. Olanow. Pathophysiology of the basal ganglia in parkinson's disease. *Trends in Neurosciences*, 23(Suppl 1):S8–19, 2000.

[158] M. Ogura and H. Kita. Dynorphin exerts both postsynaptic and presynaptic effects in the globus pallidus of the rat. *Journal of neurophysiology*, 83:3366–3376, 2000.

[159] M. S. Okun. Deep-brain stimulation for parkinson's disease. *New England Journal of Medicine*, 367(16):1529–1538, 2012.

[160] J. Olszewski and J. Baxter. *Cytoarchitecture of the human brain stem*. Lippincott, Philadelphia, USA, 1 edition, 1954.

[161] P. A. Pahapill and A. M. Lozano. The pedunculopontine nucleus and parkinson's disease. *Brain*, 123:1767–1783, 2000.

[162] A. Parent and L. N. Hazrati. Functional anatomy of the basal ganglia. ii. the place of subthalamic nucleus and external pallidum in basal ganglia circuitry. *Brain Research Reviews*, 20(1): 128–154, 1995.

[163] A. Pavlov, V. A. Makarov, I. Makarova, and F. Panetsos. Sorting of neural spikes: When wavelet based methods outperform principal component analysis. *Natural Computing*, 6:269–281, 2007.

[164] G. Paxinos and C. Watson. *The rat brain in stereotaxic coordinates*. Academic Press, San Diego, fourth edition, 1998.

[165] A. Pazienti and S. Grün. Robustness of the significance of spike synchrony with respect to sorting errors. *Journal of Computational Neuroscience*, 21(3):329–342, 2006.

[166] M. Pierantozzi, M. G. Palmieri, S. Galati, P. Stanzione, A. Peppe, D. Tropepi, L. Brusa, A. Pisani, V. Moschella, M. G. Marciani, P. Mazzone, and A. Stefani. Pedunculopontine nucleus deep brain stimulation changes spinal cord excitability in parkinson's disease patients. *Journal of neural transmission*, 115(5):731–735, 2007.

[167] P. F. Pinsky and J. Rinzel. Synchrony measures for biological neural networks. *Biological Cybernetics*, 73(2):129–137, 1995.

[168] M. Pirini, L. Rocchi, M. Sensi, and L. Chiari. A computational modelling approach to investigate different targets in deep brain stimulation for parkinson's disease. *Journal of Computational Neuroscience*, 26(1):91–107, 2009.

[169] P. Plaha and S. S. Gill. Bilateral deep brain stimulation of the pedunculopontine nucleus for parkinson's disease. *Neuroreport*, 16(17):1883–1887, November 2005.

[170] D. Plenz and S. T. Kital. A basal ganglia pacemaker formed by the subthalamic nucleus and external globus pallidus. *Nature*, 400:677–682, June 1999.

[171] O. Popovych and P. A. Tass. Desynchronizing electrical and sensory coordinated reset neuromodulation. *Frontiers in Human Neuroscience*, 6, 2012.

[172] W. H. Press, S. A. Teukolsky, W. T. Vetterling, and B. P. Flannery. *Numerical recipes in C: the art of scientific computing*. Cambridge University Press, second edition, 1992.

[173] A. Priori, G. Foffani, A. Pesenti, F. Tamma, A. Bianchi, M. Pellegrini, M. Locatelli, K. Moxon, and R. Villani. Rhythm-specific pharmacological modulation of subthalamic activity in parkinson's disease. *Experimental Neurology*, 189(2):369–379, 2004.

[174] R. Q. Quiroga, Z. Nadasdy, and Y. Ben-Shaul. Unsupervised spike detection and sorting with wavelets and superparamagnetic clustering. *Neural Computation*, 16(8):1661–1687, 2004.

[175] N. J. Ray, N. Jenkinson, S. Wang, P. Holland, J. S. Brittain, C. Joint, J. F. Stein, and T. Aziz. Local field potential beta activity in the subthalamic nucleus of patients with parkinson's disease is associated with improvements in bradykinesia after dopamine and deep brain stimulation. *Experimental Neurology*, 213(1):108–113, 2008.

[176] A. Raz, E. Vaadia, and H. Bergman. Firing patterns and correlations of spontaneous discharge of pallidal neurons in the normal and the tremulous 1-methyl-4-phenyl-1,2,3,6-tetrahydropyridine vervet model of parkinsonism. *The Journal of Neuroscience*, 20(22):8559–8571, 2000.

[177] M. Rizzone, M. Lanotte, B. Bergamasco, A. Tavella, E. Torre, G. Faccani, A. Melcarne, and L. Lopiano. Deep brain stimulation of the subthalamic nucleus in parkinson's disease: effects of variation in stimulation parameters. *Journal of Neurology, Neurosurgery & Psychiatry*, 71(2): 215–219, 2001.

[178] M. C. Rodriguez-Oroz, M. Rodriguez, J. Guridi, K. Mewes, V. Chockkman, J. Vitek, M. R. DeLong, and J. A. Obeso. The subthalamic nucleus in parkinson's disease: somatotopic organization and physiological characteristics. *Brain*, 124(9):1777–1790, 2001.

[179] M. C. Rodriguez-Oroz, J. A. O. A. E. Lang, J. L. Houeto, P. Pollak, S. Rehncrona, J. Kulisevsky, A. Albanese, J. Volkmann, M. I. Hariz, N. P. Quinn, J. D. Speelman, J. Guridi, I. Zamarbide, A. Gironell, J. Molet, B. Pascual-Sedano, B. Pidoux, A. M. Bonnet, Y. Agid, J. Xie, A. L. Benabid, A. M. Lozano, J. Saint-Cyr, L. Romito, M. F. Contarino, M. Scerrati, V. Fraix, and N. van Blercom. Bilateral deep brain stimulation in parkinson's disease: a multicentre study with 4 years follow-up. *Brain*, 128(10):2240–2249, October 2005.

[180] G. Rozas, M. Guerra, and J. Labandeira-García. An automated rotarod method for quantitative drug-free evaluation of overall motor deficits in rat models of parkinsonism. *Brain Research Protocols*, 2(1):75–84, 1997.

[181] J. E. Rubin and D. Terman. High frequency stimulation of the subthalamic nucleus eliminates pathological thalamic rhythmicity in a computational model. *Journal of Computational Neuroscience*, 16(3):211–235, 2004.

[182] I. A. Rybak, K. Ptak, N. A. Shevtsova, and D. R. McCrimmon. Sodium currents in neurons from the rostroventrolateral medulla of the rat. *Journal of Neurophysiology*, 90(3):1635–1642, September 2003.

[183] I. A. Rybak, N. A. Shevtsova, W. M. St-John, J. F. R. Paton, and O. Pierrefiche. Endogenous rhythm generation in the pre-bötzinger complex and ionic currents: Modelling and in vitro studies. *European Journal of Neuroscience*, 18(2):239257, July 2003.

[184] R. F. Salazar, P. König, and C. Kayser. Directed interactions between visual areas and their role in processing image structure and expectancy. *European Journal of Neuroscience*, 20(5): 1391–1401, August 2004.

[185] E. Scarnati, A. Proia, S. D. Loreto, and C. Pacitti. The reciprocal electrophysiological influence between the nucleus tegmenti pedunculopontinus and the substantia nigra in normal and decorticated rats. *Brain research*, 423:116–124, March 1987.

[186] A. Schober. Classic toxin-induced animal models of parkinsons disease: 6-ohda and mptp. *Cell and Tissue Research*, 318:215–224, July 2004.

[187] U. Schridde and G. van Luijtelaar. The role of hippocampal theta activity in sensory gating in the rat. *Physiology and Behavior*, 74(3):257–266, 2001.

[188] C. Seifried, L. Weise, R. Hartmann, T. Gasser, S. Baudrexel, A. Szelényi, S. van de Loo, H. Steinmetz, V. Seifert, J. Roeper, and R. Hilker. Intraoperative microelectrode recording for the delineation of subthalamic nucleus topography in parkinson's disease. *Brain Stimulation*, 5(3):378–387, 2012.

[189] A. Sharott, P. J. Magill, D. Harnack, A. Kupsch, W. Meissner, and P. Brown. Dopamine depletion increases the power and coherence of β-oscillations in the cerebral cortex and subthalamic nucleus of the awake rat. *European Journal of Neuroscience*, 21(5):1413–1422, 2005.

[190] J. Siegfried and B. Lippitz. Bilateral chronic electrostimulation of ventroposterolateral pallidum: A new therapeutic approach for alleviating all parkinsonian symptoms. *Neurosurgery*, 35(6):1126–1130, 1994.

[191] C. Simon, N. Kezunovic, M. Ye, J. Hyde, A. Hayar, D. K. Williams, and E. Garcia-Rill1. Gamma band unit activity and population responses in the pedunculopontine nucleus. *Journal of Neurophysiology*, 104:463–474, May 2010.

[192] P. J. Sjöström, G. G. Turrigiano, and S. B. Nelson. Rate, timing, and cooperativity jointly determine cortical synaptic plasticity. *Neuron*, 32(6):1149–1164, 2001.

[193] Y. Smith and J. Z. Kieval. Anatomy of the dopamine system in the basal ganglia. *Trends in Neurosciences*, 23(Suppl 1):S28–S33, 2000.

[194] Y. Smith, M. D. Bevan, E. Shink, and J. P. Bolam. Microcircuitry of the direct and indirect pathways of the basal ganglia. *Neuroscience*, 86(2):353–387, 1998.

[195] I. M. Stanford and A. J. Cooper. Presynaptic μ and δ opioid receptor modulation of gaba_a ipscs in the rat globus pallidus in vitro. *The Journal of Neuroscience*, 19(12):4796–4803, June 1999.

[196] A. Stefani, A. M. Lozano, A. Peppe, P. Stanzione, S. Galati, D. Tropepi, M. Pierantozzi, L. Brusa, E. Scarnati, and P. Mazzone. Bilateral deep brain stimulation of the pedunculopontine and subthalamic nuclei in severe parkinson's disease. *Brain*, 130:1596–1607, January 2007.

[197] F. Steigerwald, M. Pötter, J. Herzog, M. Pinsker, F. Kopper, H. Mehdorn, G. Deuschl, and J. Volkmann. Neuronal activity of the human subthalamic nucleus in the parkinsonian and nonparkinsonian state. *Journal of Neurophysiology*, 100(5):2515–2524, 2008.

[198] K. E. Stephan, L. M. Harrison, S. J. Kiebel, O. David, W. D. Penny, and K. J. Friston. Dynamic causal models of neural system dynamics: current state and future extensions. *Journal of Biosciences*, 32(1):129–144, 2007.

[199] K. E. Stephan, W. D. Penny, R. J. Moran, H. E. M. D. Ouden, J. Daunizeau, and K. J. Friston. Ten simple rules for dynamic causal modeling. *Neuroimage*, 49(4):3099–3109, 2010.

[200] S. H. Strogatz and R. E. Mirollo. Stability of incoherence in a population of coupled oscillators. *Journal of Statistical Physics*, 63(3):613–635, 1991.

[201] D. J. Surmeier, W. J. Song, and Z. Yan. Coordinated expression of dopamine receptors in neostriatal medium spiny neurons. *The Journal of Neuroscience*, 16(20):6579–6591, 1996.

[202] K. Takakusaki and S. T. Kitai. Ionic mechanisms involved in the spontaneous firing of tegmental pedunculopontine nucleus neurons of the rat. *Neuroscience*, 78(3):771–794, 1997.

[203] K. Takakusaki, T. Shiroyama, T. Yamamoto, and S. T. Kitai. Cholinergic and noncholinergic tegmental pedunculopontine projection neurons in rats revealed by intracellular labeling. *The Journal of Comparative Neurology*, 371:345–361, 1996.

[204] K. Takakusaki, T. Shiroyama, and S. T. Kitai. Two types of cholinergic neurons in the rat tegmental pedunculopontine nucleus: Electrophysiological and morphological characterization. *Neuroscience*, 79(4):10891109, 1997.

[205] K. Takakusaki, K. Saitoh, H. Harada, and M. Kashiwayanagi. Role of basal ganglia-brainstem pathways in the control of motor behaviors. *Neuroscience Research*, 50:137–151, 2004.

[206] S. K. H. Tan, R. Vlamings, L. Lim, T. Sesia, M. L. Janssen, H. W. Steinbusch, V. Visser-Vandewalle, and Y. Temel. Experimental deep brain stimulation in animal models. *Neurosurgery*, 67(4):1073–1080, October 2010.

[207] P. Tass, D. Smirnov, A. Karavaev, U. Barnikol, T. Barnikol, I. Adamchic, C. Hauptmann, N. Pawelcyzk, M. Maarouf, V. Sturm, H. Freund, and B. Bezruchko. The causal relationship between subcortical local field potential oscillations and parkinsonian resting tremor. *Journal of Neural Engineering*, 7:16009, 2010.

[208] P. A. Tass. A model of desynchronizing deep brain stimulation with a demand-controlled coordinated reset of neural subpopulations. *Biological Cybernetics*, 89(2):81–88, 2003.

[209] P. A. Tass, A. N. Silchenko, C. Hauptmann, U. B. Barnikol, and E. J. Speckmann. Long-lasting desynchronization in rat hippocampal slice induced by coordinated reset stimulation. *Physical Review E*, 80(1):011902, 2009.

[210] P. Temperli, J. Ghika, J. G. Villemure, P. R. Burkhard, J. Bogousslavsky, and F. J. G. Vingerhoets. How do parkinsonian signs return after discontinuation of subthalamic dbs? *Neurology*, 60 (1):78–81, 2003.

[211] D. Terman, J. E. Rubin, A. C. Yew, and C. J. Wilson. Activity patterns in a model for the subthalamopallidal network of the basal ganglia. *The Journal of Neuroscience*, 22(7):2963–2976, April 2002.

[212] T. Trottenberg, A. Kupsch, G. Schneider, P. Brown, and A. A. Kühn. Frequency-dependent distribution of local field potential activity within the subthalamic nucleus in parkinson's disease. *Experimental Neurology*, 205(1):287–291, 2007.

[213] E. Tsang, C. Hamani, E. Moro, F. Mazzella, Y. Poon, A. Lozano, and R. Chen. Involvement of the human pedunculopontine nucleus region in voluntary movements. *Neurology*, 75(1-10), 2010.

[214] U. Ungerstedt and G. W. Arbuthnott. Quantitative recording of rotational behavior in rats after 6-hydroxy-dopamine lesions of the nigrostriatal dopamine system. *Brain Research*, 24(3): 485–493, 1970.

[215] K. Usunoff, D. Itzev, W. A. Ovtscharoff, and E. Marani. Neuromelanin in the human brain: a review and atlas of pigmented cells in the substantia nigra. *Archives of Physiology and Biochemistry*, 110(4):257–369, 2002.

[216] S. K. van den Eeden, C. M. Tanner, A. L. Bernstein, R. D. Fross, A. Leimpeter, D. A. Bloch, and L. M. Nelson. Incidence of parkinson's disease: Variation by age, gender, and race/ethnicity. *American Journal of Epidemiology*, 157(11), 2003.

[217] G. van Luijtelaar, E. Sitnikova, and A. Lüttjohann. On the origin and suddenness of absences in genetic absence models. *Clinical EEG and Neuroscience*, 42(2):83–97, 2011.

[218] R. van Oosten and A. Cools. Differential effects of a small, unilateral, 6-hydroxydopamine-induced nigral lesion on behavior in high and low responders to novelty. *Experimental Neurology*, 173(2):245–255, 2002.

[219] J. Volkmann, J. Herzog, F. Kopper, and G. Deuschl. Introduction to the programming of deep brain stimulators. *Movement Disorders*, 17(Suppl 3):S181–187, 2002.

[220] J. Volkmann, E. Moro, and R. Pahwa. Basic algorithms for the programming of deep brain stimulation in parkinson's disease. *Movement Disorders*, 21(Suppl 14):S284–289, 2006.

[221] R. N. Walsh and R. A. Cummins. The open-field test: A critical review. *Psychological Bulletin*, 83(3):482–504, May 1976.

[222] D. J. Watts and S. H. Strogatz. Collective dynamics of 'small-world' networks. *Nature*, 393: 440–442, 1998.

[223] M. Weinberger, N. Mahant, W. D. Hutchison, A. M. Lozano, E. Moro, M. Hodaie, A. E. Lang, and J. O. Dostrovsky. Beta oscillatory activity in the subthalamic nucleus and its relation to dopaminergic response in parkinson's disease. *Journal of Neurophysiology*, 96(6):3248–3256, 2006.

[224] M. Weinberger, C. Hamani, W. D. Hutchison, E. Moro, A. M. Lozano, and J. O. Dostrovsky. Pedunculopontine nucleus microelectrode recordings in movement disorder patients. *Experimental brain research*, 188(2):165–174, June 2008.

[225] M. M. Wickremaratchi, D. Perera, C. O'Loghlen, D. Sastry, E. Morgan, A. Jones, P. Edwards, N. P. Robertson, C. Butler, H. R. Morris, and Y. Ben-Shlomo. Prevalence and age of onset of parkinsons disease in cardiff: a community based cross sectional study and meta-analysis. *Journal of Neurology, Neurosurgery & Psychiatry*, 80(7), 2009.

[226] C. L. Wilson, M. Puntis, and M. G. Lacey. Overwhelmingly asynchronous firing of rat subthalamic nucleus neurones in brain slices provides little evidence for intrinsic interconnectivity. *Neuroscience*, 123(1):187–200, 2004.

[227] M. A. Woodin, K. Ganguly, and M. Poo. Coincident pre- and postsynaptic activity modifies gabaergic synapses by postsynaptic changes in cl^- transporter activity. *Neuron*, 39(5):807–820, 2003.

[228] N. Yamawaki, P. J. Magill, G. L. Woodhall, S. D. Hall, and I. M. Stanford. Frequency selectivity and dopamine-dependence of plasticity at glutamatergic synapses in the subthalamic nucleus. *Neuroscience*, 203:1–11, 2012.

[229] W. Yan, Q. J. Zhang, J. Liu, T. Wang, S. Wang, X. Liu, L. Chen, and Z. H. Gui. The neuronal activity of thalamic parafascicular nucleus is conversely regulated by nigrostriatal pathway and pedunculopontine nucleus in the rat. *Brain Research*, 1240:204–212, 2008.

[230] A. Zaidel, A. Spivak, B. Grieb, H. Bergman, and Z. Israel. Subthalamic span of β oscillations predicts deep brain stimulation efficacy for patients with parkinson's disease. *Brain*, 133(7): 2007–2012, 2010.

[231] L. I. Zhang, H. W. Tao, C. E. Holt, W. A. Harris, and M. Poo. A critical window for cooperation and competition among developing retinotectal synapses. *Nature*, 395(6697):37–44, 1998.

Summary

Parkinson's disease (PD) is characterized by the cell death of neuronal brain cells producing the signaling molecule dopamine. Due to resulting shortage of dopamine, the dynamics of neuronal cells changes, most notably abnormal synchronization of neuronal activity. Such changes complicate the information processing in the brain, resulting in symptoms such as tremor, rigidity and slowness of movement.

Deep brain stimulation (DBS) is a surgical treatment where an electrode is implanted to stimulate a specific brain region. DBS is a well-established treatment when medication is no longer effective for PD. DBS is meant to desynchronize pathological oscillations, as they are thought to be the main cause of the symptoms. Despite the high clinical success rate, the way how the pathological activity originates in the brain and how DBS can compensate it are still unresolved questions. Computational modeling is a valuable tool for finding answers to these questions.

In the first part of the thesis, computational models are employed in order to get insight in new proposed stimulation therapies for PD. It is demonstrated that stimulation of the pedunculopontine nucleus can eliminate the pathological activity from the entire network model. It is suggested that short-duration desynchronizing stimulation protocols may also disrupt pathological synchronous activity. The results of simulation show that plasticity within the globus pallidus pars externa might be an explanation for this claim.

The second half of this thesis focuses on the analysis of single-unit recordings of subthalamic nucleus (STN) cells obtained from PD patients and the acquisition of local field potentials (LFP) in parkinsonian rats. Although it was possible to record clean LFP data, using these data in combination with spiking neuron models is not straightforward. It has been shown that the firing behavior of single units is different in the sensorimotor part of the STN than in other parts of the STN. Postoperative evaluation of target stimulation areas in the investigated PD patients with DBS shows a significant preference for the sensorimotor part of the STN. Therefore, analysis of the firing behavior may help to discriminate the STN sensorimotor part for the optimal placement of the DBS electrode.

Samenvatting

De ziekte van Parkinson wordt gekenmerkt door het afsterven van neurale hersencellen die de stof dopamine produceren. Omdat deze stof wordt gebruikt voor de communicatie tussen hersencellen, zal een tekort aan dopamine de informatieverwerking in de hersenen verstoren. Wanneer een groot deel van deze hersencellen is afgestorven kan dit leiden tot een aantal symptomen, waaronder een tremor, stijfheid en traagheid in het bewegen. Op dit moment denkt men dat het dopamine tekort leidt tot synchrone activiteit van neurale hersencellen, wat zich vervolgens uit in de bovengenoemde symptomen.

Wanneer parkinsonpatiënten geen baat meer hebben bij medicatie, gaat men soms over tot operatief ingrijpen om de motorische symptomen te verminderen. Een voorbeeld hiervan is diepe hersenstimulatie (DHS). Bij deze behandeling wordt een stimulator ingebracht die elektrische pulsjes toedient aan specifieke gebieden in het brein. Op deze manier kan de pathologische activiteit in deze gebieden desynchroniseren. Ondanks de overtuigende klinische resultaten, blijven vragen over het ontstaan van pathologische, synchrone activiteit in het brein en de precieze werking van DHS nog onbeantwoord. Een wiskundig model is een uitermate geschikt middel om antwoord op deze elementaire vragen te krijgen.

In het eerste deel van dit proefschrift worden computermodellen gebruikt om inzicht te krijgen in recent voorgestelde DHS therapieën voor de ziekte van Parkinson. De hersengebieden waar DHS momenteel wordt toegepast hebben nauwelijks invloed op de balansproblemen die bepaalde patiënten in een latere stadium ondervinden. Met een relevant netwerk model van de delen in het brein wordt bestudeerd of het stimuleren van de Pedunculopontine nucleus (PPN) een positief effect kan hebben voor deze patiënten. Simulaties tonen aan dat het met stimulatie van de PPN mogelijk is om de pathologische synchrone activiteit teniet te doen. Daarnaast wordt gesuggereerd dat kortstondige desynchroniserende stimulatie in plaats van continue stimulatie van de hersengebieden de pathologische synchrone activiteit ook kan verstoren. De resultaten van simulaties laten zien dat plasticiteit binnen de Globus Pallidus *pars externa* een mogelijke verklaring is voor dit effect.

Het tweede deel van het proefschrift richt zich op het verkrijgen en analyseren van metingen om zo het voorgaande modeleerwerk te ondersteunen. In het bijzonder worden extracellulaire micro-elektrode metingen bestudeerd van individuele cellen in de Subthalamische nucleus (STN), welke zijn verkregen tijdens de DHS operatie bij parkinsonpatiënten. Tevens worden de mogelijkheden geïnventariseerd om lokale veld potentialen te meten in ratten met parkinsonisme. Het bleek inderdaad mogelijk om de lokale veld potentialen van meerdere hersenkernen simultaan te meten. Deze metingen waren echter ontoereikend om bepaalde analyses te doen. Daarentegen leverde de analyse van afzonderlijke cel metingen belangrijke en nieuwe inzichten. Ze tonen aan dat het vuurgedrag in het sensorimotorische deel van de STN anders is dan in de andere delen van de STN. Postoperatieve evaluatie naar het meest effectieve klinisch gebied voor stimulatie laat een significante voorkeur zien voor het sensorimotorische deel van de STN. Zodoende blijkt dat het analyseren van het vuurgedrag tijdens de operatie een belangrijke bijdrage kan leveren bij de identificatie van het sensorimotorische deel van de STN. Op deze manier kan de DHS elektrode optimaal geplaatst worden.

Dankwoord

De afgelopen 5 jaar heb ik gewerkt aan de totstandkoming van dit proefschrift in de Applied Analysis and Mathematical Physics groep aan de Universiteit Twente. Een deel van mijn onderzoek heb ik uit mogen voeren in het Academic Medisch Centrum (AMC) en het Donders Instituut aan de Radboud Universiteit Nijmegen. Door deze verschillende werkplekken heb ik met veel plezier mogen samenwerken met een gezellige en inspirerende groep mensen. Hierdoor heb ik ervaren dat je een promotieonderzoek niet in je eentje uitvoert, maar dat er vele helpende handen zijn. Daarom wil ik iedereen bedanken die heeft bijgedragen aan de totstandkoming van mijn proefschrift. Zonder anderen tekort te willen doen, wil ik een aantal mensen in het bijzonder noemen.

Als eerste wil ik mijn promotor en dagelijkse begeleider Stephan van Gils bedanken. Wat fijn Stephan dat je mij 5 jaar geleden de mogelijkheid hebt gegeven om aan dit promotieonderzoek te beginnen en bedankt voor jouw hulp om het te volbrengen. Jouw enthousiasme en positieve kijk op dit onderzoek gaven mij het vertrouwen om dit project goed af te ronden. Ook kon ik altijd binnen lopen voor vragen en mailtjes werden zelfs laat in de avond of in het weekend nog beantwoord (sorry Andrea). De espresso's en chocolade muffins waren natuurlijk ook een enorme motivatie voor mij.

Ik wil mijn assistent-promotor Lo Bour bedanken, omdat hij mij de mogelijkheid heeft gegeven om in het AMC data van patiënten te mogen analyseren. Door jouw positiviteit moest mijn kritische blik herhaaldelijk het onderspit delven, waardoor ik telkens weer een stapje verder kwam in mijn onderzoek. Jouw inzet heeft zeker bijgedragen aan de kwaliteit van dit proefschrift. Ook kijk ik uit naar onze samenwerking het komende halfjaar. Ik wil ook alle mensen op jouw afdeling bedanken voor hun hulp en in het bijzonder Fiorella, Pepijn en Rick.

I would like to express my acknowledgment to the rest of the graduation committee, C.F. Beckmann, H.C.F. Martens, C.C. McIntyre, M.J.A.M. van Putten, Y. Temel and P.H. Veltink for their valuable time in reading and evaluating this thesis.

Ik wil Gilles van Luijtelaar bedanken dat hij mij als wiskundige toeliet in zijn dierenlab op het Donders Instituut om ratten te opereren en gedragstesten af te nemen. Je had gelijk dat het allemaal te leren valt. Verder wil ik alle mensen bij het Donders Instituut bedanken die mij hebben geholpen bij het uitvoeren van de dierexperimenten. In het bijzonder wil ik Annika bedanken voor het leren opereren en alle praktische tips die je me gaf en Roeland voor het assisteren tijdens het hele experiment.

De collega's en vrienden van toegepaste wiskunde en BrainGain wil ik bedanken voor de samenwerking en gezelligheid van de afgelopen jaren. Hil bedankt voor je kritische blik. Ook zorgde jij er telkens weer voor dat ik mijn gedachtenspinsels op papier zette. Ciska en Enrico bedankt voor jullie nuttige discussies en commentaar op mijn manuscripts. Sid, Bettina en Julia bedankt voor de interessante discussies, maar vooral ook voor jullie gezelschap op de werkplek. Ook hebben jullie samen met Alef, Anastasia, Sander en Bob ervoor gezorgd dat ik niet de hele dag achter mijn beeldscherm gekluisterd zat, maar ook nog buiten kwam om een luchtje te scheppen. Sid zonder jouw hulp waren de figuren in mijn proefschrift niet van de kwaliteit geweest, zoals ze nu zijn. Ook jouw ratten fotoshoot heeft een plaatsje gekregen in mijn boekje, waar ik erg blij mee ben. Verder wil ik ook mijn andere kamergenoten Alyona, Domokos, Ivan, Lie, Tim en Vijaya bedanken voor de leuke tijd samen en natuurlijk ook de secretaresses, Marielle en Linda, voor hun hulp.

Ook wil ik al mijn andere vrienden bedanken voor de nodige afleiding en ontspanning tijdens mijn promotieonderzoek. Edwin wat fijn dat ik 's avonds laat na mijn werk in het AMC nog zo vaak bij je aan kon schuiven voor een hapje eten. Ook wil ik Toon en José, Bjorn en Annemiek en Lise bedanken voor hun interesse in mijn onderzoek, mijn ouders, Petra en Johan en mijn neefje en nichtjes bedanken voor hun steun.

En natuurlijk wil ik mijn lieve Kim bedanken voor al haar liefde en steun en, in de laatste maanden, voor al haar geduld. Ik beloof dat ik nu veel meer tijd voor jou zal vrijmaken.

Marcel, februari 2013

About the author

Marcel Lourens was born in Deventer, The Netherlands on November 30, 1980. In 1999, he obtained his VWO diploma at the Revius in Deventer. From September 2000 until August 2007 he studied Biomedical Engineering at the Eindhoven University of Technology. As part of this study, he did an internship at Radi Medical Systems AB in Uppsala, Sweden. He evaluated the possibility to use their PressureWire sensor as a flow sensor. The research for his master thesis "A mathematical model for platelet adhesion and activation: application to cerebral arteries" was performed at the Cardiovascular Biomechanics group under the supervision of dr.ir. P.H.M. Bovendeerd and prof.dr.ir. F.N. van de Vosse. During his study, he also followed a course on laboratory animal science and received the 'Article 9' certificate. In January 2008, he started his PhD research under supervision of prof.dr. S.A. van Gils in the group of Applied Analysis and Mathematical Physics at the University of Twente, The Netherlands. Part of this PhD research was performed at the Academic Medical Center (AMC) in Amsterdam and the Donders Institute for Brain, Cognition and Behaviour at the Radboud University Nijmegen. The result of his PhD research is contained in this thesis. Since March of this year, Marcel is working as a post-doctoral researcher at AMC and Sapiens Steering Brain Stimulation.

ISBN: 978-90-365-3507-6